Charged-particle multiplicities in *pp* interactions measured with the ATLAS detector at the LHC

The ATLAS Collaboration

Abstract. Measurements are presented from proton–proton collisions at centre-of-mass energies of $\sqrt{s} = 0.9$, 2.36 and 7 TeV recorded with the ATLAS detector at the LHC. Events were collected using a single-arm minimum-bias trigger. The charged-particle multiplicity, its dependence on transverse momentum and pseudorapidity and the relationship between the mean transverse momentum and charged-particle multiplicity are measured. Measurements in different regions of phase space are shown, providing diffraction-reduced measurements as well as more inclusive ones. The observed distributions are corrected to well-defined phase-space regions, using model-independent corrections. The results are compared to each other and to various Monte Carlo (MC) models, including a new AMBT1 PYTHIA6 tune. In all the kinematic regions considered, the particle multiplicities are higher than predicted by the MC models. The central charged-particle multiplicity per event and unit of pseudorapidity, for tracks with $p_T > 100$ MeV, is measured to be 3.483 ± 0.009 (stat) ± 0.106 (syst) at $\sqrt{s} = 0.9$ TeV and 5.630 ± 0.003 (stat) ± 0.169 (syst) at $\sqrt{s} = 7$ TeV.

IOP Institute of Physics ⏀ DEUTSCHE PHYSIKALISCHE GESELLSCHAFT

Contents

1. Introduction

Inclusive charged-particle distributions have been previously measured in pp and $p\bar{p}$ collisions in a range of different centre-of-mass energies [1–17]. These measurements provide insight into the strong interactions at low energy scales. Several quantum chromodynamics (QCD)-inspired models have been developed to interpret them. These models are frequently cast into Monte Carlo (MC) simulations with free parameters that can be constrained by measurements such as minimum bias distributions. These measurements contribute to the understanding of soft QCD; moreover, they are important in the determination of biases on high-p_T phenomena due to underlying events (UEs) and event pileup effects and are therefore of growing importance for future Large Hadron Collider (LHC) physics. The measurements presented in this paper implement a similar strategy to that in [1]. A single-arm trigger overlapping with the acceptance of the tracking volume is used. The results are presented as inclusive-inelastic distributions, with minimal model dependence; a minimum number of charged particles within well-defined p_T and η selection are required.

This paper reports on measurements of primary charged-particle multiplicity distributions using the first $\sim 190\,\mu b^{-1}$ of data recorded by the ATLAS experiment at 7 TeV and $\sim 7\,\mu b^{-1}$ at 0.9 TeV. At $\sqrt{s} = 0.9$ TeV the sample is similar to that used for the first ATLAS minimum-bias publication [1]. The results are also presented at $\sqrt{s} = 2.36$ TeV where the track reconstruction setup differs significantly from that at the other energies, due to the silicon tracker (SCT) not being at nominal voltage. The integrated luminosity at this energy is estimated to be $\sim 0.1\,\mu b^{-1}$.

The following distributions are measured in this paper:

$$\frac{1}{N_{ev}} \cdot \frac{dN_{ch}}{d\eta}, \quad \frac{1}{N_{ev}} \cdot \frac{1}{2\pi p_T} \cdot \frac{d^2 N_{ch}}{d\eta dp_T}, \quad \frac{1}{N_{ev}} \cdot \frac{dN_{ev}}{dn_{ch}} \quad \text{and} \quad \langle p_T \rangle \text{ versus } n_{ch},$$

where p_T is the charged-particle momentum component transverse to the beam direction[1], η is the pseudorapidity of the particle, n_{ch} is the number of charged particles in an event, N_{ev} is the number of events with a minimum number of charged particles within the selected kinematic range, N_{ch} is the total number of charged particles in the data sample and $\langle p_T \rangle$ is the average p_T for a given number of charged particles[2]. Primary charged particles are defined as charged particles with a mean lifetime $\tau > 0.3 \times 10^{-10}$ s either directly produced in pp interactions or from subsequent decays of particles with a shorter lifetime.

The charged-particle multiplicity results are compared to particle-level MC predictions. Three different phase-space regions are considered in this paper, with varying selection both on the p_T and the number of charged particles per event; all phase-space regions require tracks within $|\eta| < 2.5$. Diffractive physics is expected to contribute mostly at low numbers of charged particles and at low track momentum. Therefore, varying the selection on n_{ch} and p_T in effect varies the relative contribution from diffractive events. Appendix B shows the results

---

[1] The ATLAS reference system is a Cartesian right-handed co-ordinate system, with the nominal collision point at the origin. The anti-clockwise beam direction defines the positive z-axis, while the positive x-axis is defined as pointing from the collision point to the centre of the LHC ring and the positive y-axis points upwards. The azimuthal angle ϕ is measured around the beam axis and the polar angle θ is measured with respect to the z-axis. The pseudorapidity is defined as $\eta = -\ln \tan(\theta/2)$.
[2] The factor $2\pi p_T$ in the p_T spectrum comes from the Lorentz invariant definition of the cross section in terms of $d^3 p$. Our results could thus be interpreted as the massless approximation to $d^3 p$.

for two additional phase-space regions useful for MC tuning. This measurement, with refined corrections and systematic uncertainty determination, supersedes the results presented in [1].

2. The ATLAS detector

The ATLAS detector [18] at the LHC [19] covers almost the whole solid angle around the collision point with layers of tracking detectors, calorimeters and muon chambers. It has been designed to study a wide range of physics topics at LHC energies. For the measurements presented in this paper, the tracking devices and the trigger system are of particular importance.

The ATLAS Inner Detector (ID) has full coverage in ϕ and covers the pseudorapidity range $|\eta| < 2.5$. It consists of a silicon pixel detector (Pixel), a silicon microstrip detector (SCT) and a transition radiation tracker (TRT). These detectors cover a sensitive radial distance from the interaction point of 50.5–150, 299–560 and 563–1066 mm, respectively, and are immersed in a 2 T axial magnetic field. The ID barrel (end-cap) parts consist of three (2×3) Pixel layers, four (2×9) double layers of single-sided silicon microstrips with a 40 mrad stereo angle and 73 (2×160) layers of TRT straws. Typical position resolutions are 10, 17 and 130 μm for the R–ϕ co-ordinate and, in the case of the Pixel and SCT, 115 and 580 μm for the second measured co-ordinate. A track from a charged particle traversing the barrel detector would typically have 11 silicon hits[3] (three pixel clusters and eight strip clusters) and more than 30 straw hits.

For the runs at $\sqrt{s} = 2.36$ TeV, stable beams were not declared by the LHC; the high voltage on the SCT detector was thus not turned up to its nominal operating voltage but was left in standby mode. The Pixel detector was in nominal conditions for these runs. The hit efficiency in the SCT is thus significantly lower and special track reconstruction algorithms are needed; the single hit efficiency at nominal voltage in the SCT barrel is above 99.7% [20], while in standby it drops to ∼60% for tracks perpendicular to the silicon surface.

The ATLAS detector has a three-level trigger system: Level 1 (L1), Level 2 (L2) and Event Filter (EF). For this measurement, the trigger relies on the L1 signals from the Beam Pickup Timing Devices (BPTX) and the Minimum Bias Trigger Scintillators (MBTS). The BPTX stations are composed of electrostatic button pick-up detectors attached to the beam pipe at ±175 m from the centre of the ATLAS detector. The coincidence of the BPTX signal between the two sides of the detector is used to determine when bunches are colliding at the centre of the ATLAS detector. The MBTS are mounted at each end of the detector in front of the liquid-argon end-cap calorimeter cryostats at $z = \pm3.56$ m. They are segmented into eight sectors in azimuth and two rings in pseudorapidity ($2.09 < |\eta| < 2.82$ and $2.82 < |\eta| < 3.84$). The data were collected for this analysis using a trigger requiring a BPTX coincidence and MBTS trigger signals. The MBTS trigger used for this paper is configured to require one hit above threshold from either side of the detector, referred to as a single-arm trigger. The efficiency of this trigger is studied with a separate prescaled L1 BPTX trigger, filtered to obtain inelastic interactions by Inner Detector requirements at L2 and EF, the latter only for the 900 GeV data.

3. Monte Carlo (MC) simulation

Inclusive minimum bias data are modelled using three components in the PYTHIA6 [21] MC event generator: non-diffractive (ND), single- (SD) and double-diffractive (DD). ND processes

---

[3] A hit is a measurement point assigned to a track.

are modelled from two-to-two processes as described in this section. Diffractive process modelling is described in section 3.1.

Low-p_T scattering processes may be described by lowest-order perturbative QCD two-to-two parton scatters, where the divergence of the cross-section at $p_T = 0$ is regulated by phenomenological models. The PYTHIA6 MC event generator implements several of these models. The parameters of these models have been tuned to describe charged hadron production and the UE in pp and $p\bar{p}$ data at centre-of-mass energies between 200 GeV and 1.96 TeV.

Samples of MC events were produced for SD, DD and ND processes using the PYTHIA6 generator[4]. The ATLAS MC09 PYTHIA tune [22] uses a specific set of optimized parameters; it employs the MRST LO* parton density functions (PDFs) [23] and the p_T-ordered parton shower [24]. A tune is a particular configuration or set of values of the parameters of the particular MC model. These parameters were derived by tuning to the UE and minimum-bias data from the Tevatron at 630 GeV to 1.96 TeV. The MC samples generated with this tune are used to determine detector acceptances and efficiencies and to correct the data. MC samples were produced at all three centre-of-mass energies considered in this paper. The ND, SD and DD contributions in the generated samples are mixed according to the generator cross-sections.

All the events are processed through the ATLAS detector simulation program [25], which is based on GEANT4 [26]. They are then reconstructed and analysed by the same program chain used for the data. Particular attention was devoted to the description in the simulation of the size and position of the collision beam spot and of the detailed detector conditions during data taking. The MC09 PYTHIA6 samples are used to derive the detector corrections for these measurements. The MC samples at 2.36 TeV were generated assuming nominal detector conditions.

For the purpose of comparing the present measurements to different phenomenological models describing minimum-bias events, the following additional particle-level MC samples were generated:

- the new ATLAS Minimum Bias Tune 1 (AMBT1) PYTHIA6 tune described in section 3.2;
- the DW [27] PYTHIA6 tune, which uses virtuality-ordered showers and was derived to describe the CDF Run II UE and Drell–Yan data;
- the PYTHIA8 generator[5] [28], in which the diffraction model produces much harder p_T and n_{ch} spectra for the SD and DD contributions than PYTHIA6. The default parton shower model is similar to the one used in PYTHIA6 MC09;
- the PHOJET generator[6] [29], which is used as an alternative model to PYTHIA-based generators. PHOJET relies on PYTHIA6[7] for the fragmentation of partons.

3.1. Diffractive models

PYTHIA6, PYTHIA8 and PHOJET model the diffractive components very differently. Here we mostly describe the model implemented in PYTHIA6. The PYTHIA6 diffraction is based on a Regge-based pomeron model to generate the cross-section and generate the diffractive mass and momentum transfer [30, 31]. To allow the Regge model to cover the full phase space, empirical corrections are introduced [21]. These have the effect of enhancing the production of

---

[4] PYTHIA version 6.4.21.
[5] PYTHIA version 8.130.
[6] PHOJET version 1.12.1.35.
[7] PYTHIA version 6.1.15.

small masses and suppressing production near the kinematic limit. Particle production from low mass states ($M_X < 1\,\text{GeV}$) is treated as an isotropic two-body decay. Particle production from high mass states is based on the string model. Two string configurations are possible depending on whether the pomeron couples to a quark or gluon [21].

The PYTHIA8 model uses the same model as PYTHIA6 to generate the cross-section and generate the diffractive mass and momentum transfer. The particle production for low mass states uses the string model, but for higher masses ($M_X > 10\,\text{GeV}$) a perturbative element based on pomeron–proton scattering is introduced. The non-perturbative string model introduces a mass dependence on the relative probability of the pomeron scattering off a quark to scattering off a gluon, which enhances the gluon probability at high masses. The perturbative pomeron–proton scattering uses HERA diffractive PDFs [32] and the standard multiple interactions framework is used to generate the parton–parton scattering. The introduction of the perturbative pomeron–proton scattering results in a harder p_T and multiplicity spectrum for diffractive events generated with PYTHIA8 compared with those generated with PYTHIA6 [33]. However, it should be noted that relatively little tuning has been made of the diffractive processes in PYTHIA6 and PYTHIA8.

PHOJET is based on the dual parton model. It generates a harder p_T and multiplicity spectrum in diffractive events than PYTHIA6. The new diffraction model of PYTHIA8 generates distributions quite similar to those from PHOJET [33].

3.2. PYTHIA6 ATLAS Minimum Bias Tune 1

Before the start of the LHC, an ATLAS tune to PYTHIA6 with MRST LO* PDFs using Tevatron UE and minimum bias data was produced, the so-called MC09 tune [22]. The first ATLAS measurements of charged-particle production at the LHC [1] measured the charged-particle production at $\sqrt{s} = 0.9\,\text{TeV}$ in the central region to be 5–15% higher than the MC models predict. In addition, neither the high n_{ch} nor the high p_T distributions were well described by this tune and the $\langle p_T \rangle$ was overestimated in events with $n_{\text{ch}} > 20$. A new tune, AMBT1, was developed in order to adapt the free parameters of the ND models to the new experimental data at $\sqrt{s} = 0.9\,\text{TeV}$ and $\sqrt{s} = 7\,\text{TeV}$, using the same PDFs and PYTHIA6 model choices as MC09.

The AMBT1 tune is obtained by tuning to ATLAS minimum bias data at both $\sqrt{s} = 0.9\,\text{TeV}$ and $\sqrt{s} = 7\,\text{TeV}$ in a diffraction-reduced phase space that is presented in this paper: $n_{\text{ch}} \geqslant 6$, $p_T > 500\,\text{MeV}$, $|\eta| < 2.5$. The tune was derived using preliminary versions of these distributions [34]. The starting point for this tune is the ATLAS MC09c [22] PYTHIA6 tune. MC09c is an extension of the ATLAS MC09 tune where the strength of the colour reconnection (CR) was tuned to describe the $\langle p_T \rangle$ versus n_{ch} distributions measured by CDF in $p\bar{p}$ collisions at the Tevatron [7].

Charged-particle distributions are sensitive to multi-parton interactions (MPI) and CR of the hadronic final state [35]; the MPI are regulated by a low p_T cut-off and the matter overlap distribution of the two protons in which the additional partonic scattering takes place. These are the main parameters varied for this new tune. Parameters related to final state radiation, hadronization and fragmentation are not tuned, as these are constrained by many LEP results. No changes to the diffraction model are made. The model parameters are adapted in order to best describe these new distributions over the full range while maintaining consistency with the Tevatron results. For the data MC comparisons the RIVET[8] [36] package is used; the tuning is

---

[8] Version 1.2.2a0.

Table 1. Comparison of MC09c and AMBT1 parameters. The ranges of the parameter variations scanned are also given. The parameters declared as 'fixed' were fixed at the values obtained after an initial pass of the tuning.

Parameter	Related model	MC09c value	Scanning range	AMBT1 value
PARP(90)	MPI (energy extrapolation)	0.2487	0.18–0.28	0.250
PARP(82)	MPI (p_T^{min})	2.31	2.1–2.5	2.292
PARP(84)	MPI matter overlap (core size)	0.7	0.0–1.0	0.651
PARP(83)	MPI matter overlap (fraction in core)	0.8	Fixed	0.356
PARP(78)	CR strength	0.224	0.2–0.6	0.538
PARP(77)	CR suppression	0.0	0.25–1.15	1.016
PARP(93)	Primordial $k_\perp$	5.0	Fixed	10.0
PARP(62)	ISR cut-off	1.0	Fixed	1.025

done using the PROFESSOR package[9] [37, 38]. Table 1 summarizes the parameters varied in this tune; the meaning of the parameters is given below.

3.2.1. Multi-parton interactions (MPI) parameters. The size of the MPI component in the PYTHIA6 model is regulated by a simple cut-off parameter for the $\hat{p}_T$ of two-to-two scattering processes. This cut-off parameter is fixed at a reference energy, which is generally taken as 1.8 TeV. The cut-off at this reference scale is called PARP(82). It is then rescaled for other centre-of-mass energies using a parameter PARP(90). The rescaling is done according to the following formula:

$$p_T^{min} = \text{PARP(82)} \left(\frac{E}{1.8 \text{ TeV}} \right)^{\text{PARP(90)}}. \tag{1}$$

The amount of scattering is described by the matter overlap distribution between the two protons, which regulates how many central, hard scatterings and how many less central, softer scatterings occur. This distribution is modelled as a double Gaussian probability density function. The parameter PARP(83) describes the fraction of matter in the narrower of the two Gaussian functions. The size of this narrower Gaussian is given as a fraction PARP(84) of the wider, main radius. The optimal value for this parameter was found in a first tuning run. Further variations of the matter fraction in the narrower cone were found to not have a significant influence on the main distributions used for tuning.

3.2.2. Colour reconnection (CR) parameters. The CR scenario of PYTHIA used in MC09c minimizes the total string length between partons. The probability that a given string piece does not participate in the CR is given by $(1 - \text{PARP(78)})^{n_{MI}}$, where n_{MI} is the number of MPI [21]; the larger the parameter, the smaller the probability of the string piece not participating. In addition to this parameter, an additional parameter PARP(77) is present in PYTHIA; it is used to

[9] Version 1.0.0a0.

describe a suppression factor for the CR of fast moving string pieces. The suppression factor is given by $1/(1 + \text{PARP}(77)^2 \cdot p_{\text{avg}}^2)$, where p_{avg}^2 is a measure of the average squared momentum that hadrons produced by the string piece would have.

3.2.3. Additional parameters investigated.   In an initial study, the cut-off parameter for initial state radiation (PARP(62)) and the cut-off for momentum smearing in primordial $k_\perp$ (PARP(93)) were considered. The optimal values for these parameters were found in a first tuning run; further variation of those parameters was not found to have a significant influence on the main distributions used for tuning.

3.2.4. Distributions used.   The tune described in this paper focuses on the ATLAS minimum bias data. It primarily attempts to improve the description of the high p_T and high n_{ch} distributions observed. For the p_T spectrum, only particles above 5 GeV are considered. For the n_{ch} spectrum, only events with 20 or more tracks are used in the tune. For the $\langle p_T \rangle$ versus n_{ch} distribution, only events with ten or more tracks are considered. The full η distribution is used. For completeness, the preliminary UE results [39, 40] are included in the plateau region; however, due to the limited statistics, these data have only a very small impact on the tune.

Tevatron data in the energy range of 630 GeV to 1.96 TeV are included in the tune, but with a weight that is ten times lower than that of the ATLAS data. This weighting allows a check of the consistency of the resulting tune with the Tevatron data while forcing the ATLAS data to drive the tuning process. Similar datasets were used for the MC09c tune. The charged-particle multiplicity shown in [41] was not included in the tune as no variation of the tuning parameters considered was able to fit both the ATLAS and the CDF distributions simultaneously. Appendix A shows a full list of the distributions and the ranges considered by the tune.

3.2.5. Results.   The final parameter values resulting from the tune are shown in table 1.

4. Data selection

Events in which the ID was fully operational and the solenoid magnet was on are used for this analysis for both $\sqrt{s} = 0.9$ TeV and $\sqrt{s} = 7$ TeV. During this data-taking period, more than 97% of the Pixel detector, 99% of the SCT and 98% of the TRT were operational. At $\sqrt{s} = 2.36$ TeV the requirements are the same, except for the SCT being in standby.

Events were selected from colliding proton bunches in which the MBTS trigger recorded one or more counters above threshold on either side. The maximum instantaneous luminosity is approximately 1.9×10^{27} cm^{-2} s^{-1} at 7 TeV. The probability of additional interactions in the same bunch crossing is estimated to be of the order of 0.1%. In order to perform an inclusive-inelastic measurement, no further requirements beyond the MBTS trigger are applied.

In order to better understand the track reconstruction performance at $\sqrt{s} = 2.36$ TeV, during which time the SCT was in standby, additional data at $\sqrt{s} = 0.9$ TeV were taken with the SCT in standby for part of a run. This enables the derivation of data-driven corrections to the track reconstruction efficiency, as described in section 6.4.

Table 2. Fraction of simulated events originating from diffractive processes, as predicted by PYTHIA6, PYTHIA8 and PHOJET in the three phase-space regions measured in this paper at both $\sqrt{s} = 0.9$ TeV and $\sqrt{s} = 7$ TeV. All results are for $|\eta| < 2.5$.

Phase-space region		$\sqrt{s} = 0.9$ TeV			$\sqrt{s} = 7$ TeV		
min n_{ch}	min p_T (MeV)	PYTHIA6 (%)	PYTHIA8 (%)	PHOJET (%)	PYTHIA6 (%)	PYTHIA8 (%)	PHOJET
2	100	22	22	20	21	21	14%
1	500	16	21	19	17	21	14%
6	500	0.4	5	8	0.4	10	8%

4.1. Different phase-space regions considered

Three separate phase-space regions are considered in the main part of this paper with varying contributions from diffractive events:

- at least one charged particle in the kinematic range $|\eta| < 2.5$ and $p_T > 500$ MeV,
- at least two charged particles in the kinematic range $|\eta| < 2.5$ and $p_T > 100$ MeV,
- at least six charged particles in the kinematic range $|\eta| < 2.5$ and $p_T > 500$ MeV.

The first of these phase-space regions is studied at all three centre-of-mass energies. This is the region that allows us to best investigate the evolution of charged-multiplicity distributions as a function of centre-of-mass energy and thus constrain the MC parameters that dictate the energy extrapolation of the models. The second measures the most inclusive charged-particle spectra and is also used as the basis for the model-dependent extrapolation to $p_T = 0$; in this phase-space region results at $\sqrt{s} = 0.9$ and 7 TeV are shown. The third phase-space region considered is similar to the first but with a higher cut on the number of charged particles, thus reducing the expected contribution from diffractive events in the sample. These distributions are measured for both 0.9 and 7 TeV. This is the phase-space region that was used to produce the new AMBT1 tune. At 2.36 TeV only the first phase-space region is measured. Two additional phase-space regions are presented in appendix B.

The relative contribution from diffractive events varies widely between MC models and depends strongly on the phase-space region selection applied. The diffractive contribution is constrained very little by previous data. Table 2 shows the predicted fractions of simulated events originating from diffractive processes, as predicted by PYTHIA6, PYTHIA8 and PHOJET; the values for the different tunes of PYTHIA6 are found to be similar because the acceptances of the different ND models do not change significantly and the diffractive models are identical. The large difference in predictions between the models is one of the motivations for not making any model-dependent corrections to the experimental data, as such corrections would vary significantly depending on which MC model is used to derive them.

4.2. Event selection

To reduce the contribution from background events and non-primary tracks, as well as to minimize the systematic uncertainties, the events are required to satisfy the following criteria:

- to have triggered the single-arm, single-counter level 1 minimum bias trigger scintillators;
- the presence of a primary vertex [42] reconstructed using the beam spot information [43] and at least two tracks, each with
  - $p_T > 100$ MeV;
  - a transverse distance of the closest approach with respect to the beam-spot position $|d_0^{BS}| < 4$ mm;
- the rejection of events with a second vertex containing four or more tracks, to remove events with more than one interaction per bunch crossing;
- a minimum number of tracks, depending on the particular phase-space region, as described in section 4.3.

4.3. Track reconstruction algorithms

Tracks are reconstructed offline within the full acceptance range $|\eta| < 2.5$ of the ID [44, 45]. Track candidates are reconstructed by requiring a minimum number of silicon hits and then extrapolated to include measurements in the TRT. Due to the SCT being in standby mode at 2.36 TeV, different track reconstruction algorithms are needed; at 0.9 and 7 TeV, the reconstruction algorithms are collectively referred to as full tracks. The analysis at $\sqrt{s} = 2.36$ TeV has been performed using two complementary methods for reconstructing tracks. The first reconstructs tracks using pixel detector information only, denoted by Pixel tracks. The second uses tracks reconstructed from the full ID information, denoted by ID tracks[10].

4.3.1. Algorithms for 0.9 and 7 TeV. For the measurements at 0.9 and 7 TeV, two different track reconstruction algorithms are used. The algorithm used for the previous minimum-bias publication [1] is used with a lower-p_T threshold cut at 100 MeV. An additional algorithm configuration is run using only the hits that have not been used by the first algorithm. This additional algorithm uses wider initial roads and has a looser requirement on the number of silicon hits. This second algorithm contributes around 60% of the tracks from 100 to 150 MeV, mostly due to the tracks having too low a momentum to go far enough in the SCT detector to satisfy the silicon hit requirement of the original algorithm; this fraction decreases rapidly, reaching less than 2% at 200 MeV.

Tracks are required to pass the selection criteria shown in table 3; the column labelled Full Tracks refers to the algorithms used at 0.9 and 7 TeV. The transverse, d_0, and longitudinal, z_0, impact parameters are calculated with respect to the event primary vertex. The layer-0 selection requires a hit in the innermost layer of the Pixel detector if a hit is expected[11]. The track-fit χ^2 probability[12] cut is applied to remove tracks with mismeasured p_T due to misalignment or nuclear interactions.

---

[10] In the context of the other analyses, ID tracks are referred to as track for brevity.

[11] A hit is expected if the extrapolated track crosses an active region of a Pixel module that has not been disabled.

[12] This probability function is computed as $1 - P(n_{dof}/2, \chi^2/2)$, where $P(n_{dof}/2, \chi^2/2)$ is the incomplete gamma function and n_{dof} is the number of degrees of freedom of the fit. It represents the probability that an observed χ^2 exceeds the observed value for a correct model.

Table 3. Selection criteria applied to tracks for the full reconstruction, ID tracks and pixel tracks. The transverse momentum cut applied depends on the phase-space region in question. (*) For the Pixel track method, the layer-0 is required even if not expected. (**) The SCT hit selection are for $p_T < 200$, $200 < p_T < 300$ or $p_T > 300$ MeV, respectively. (***) For the Pixel track method, the d_0 and z_0 selection are after, the track refitting is performed (see section 4.3.2).

Criteria	$\sqrt{s} = 0.9$ and 7 TeV	$\sqrt{s} = 2.36$ TeV	
	Full tracks	ID tracks	Pixel tracks
$p_T > 100$ or 500 MeV	Yes	Yes	Yes
$|\eta| < 2.5$	Yes	Yes	Yes
Layer-0 hit if expected	Yes	Yes	Yes (*)
>1 Pixel hit	Yes	Yes	Yes
>2, 4 or 6 SCT hits for tracks (**)	Yes	No	No
$|d_0| < 1.5$ mm and $|z_0| \cdot \sin\theta < 1.5$ mm	Yes	Yes	Yes (***)
χ^2 probability > 0.01 for $p_T > 10$ GeV	Yes	N/A	N/A

Table 4. The number of events and tracks in the three phase-space regions at each centre-of-mass energy considered in this paper.

Phase-space region		$\sqrt{s} = 0.9$ TeV		$\sqrt{s} = 7$ TeV		$\sqrt{s} = 2.36$ TeV	
n_{ch}	min p_T	Full tracks		Full tracks		ID tracks (pixel tracks)	
	(MeV)	Events	Tracks	Events	Tracks	Events	Tracks
2	100	357 523	4 532 663	10 066 072	209 809 430	–	–
1	500	334 411	1 854 930	9 619 049	97 224 268	5929 (5983)	38 983 (44 788)
6	500	124 782	1 287 898	5 395 381	85 587 104	–	–

These tracks are used to produce the corrected distributions and will be referred to as selected tracks. The multiplicity of selected tracks within an event is denoted by n_{sel}. The tracks used by the vertex reconstruction algorithm are very similar to those used for the analysis; the p_T threshold is also 100 MeV. Due to the requirement that the vertex be made from a minimum of two such tracks and the fact that we do not wish to correct our measurement outside of the observed phase-space region, the minimum number of particles per event for the phase-space region with $p_T > 100$ MeV also needs to be set at two. Table 4 shows the total number of selected events and tracks for all phase-space regions considered.

Trigger and vertex reconstruction efficiencies are parameterized as a function of n_{sel}^{BS}. Note that n_{sel}^{BS} is defined as the number of tracks passing all of the track selection requirements except for the constraints with respect to the primary vertex; instead, the unsigned transverse impact parameter with respect to the beam spot, $|d_0^{BS}|$, is required to be less than 1.8 mm.

4.3.2. Track reconstruction algorithms at 2.36 TeV. Operation of the SCT at standby voltage during 2.36 TeV data taking led to reduced SCT hit efficiency. Consequently, ID tracks are reconstructed at this centre-of-mass energy using looser requirements on the numbers of hits

and holes[13] [44, 45]. There are no simulation samples that fully describe the SCT operating at reduced voltage. A technique to emulate the impact of operating the SCT in standby was developed in simulation; this corrects the MC without re-simulation by modifying the silicon clusterization algorithm used to study the tracking performance. However, the final ID track efficiency at $\sqrt{s} = 2.36$ TeV was determined using a correction to the track reconstruction efficiency derived from data at $\sqrt{s} = 0.9$ TeV.

Pixel tracks were reconstructed using the standard track reconstruction algorithms limited to Pixel hits and with different track requirements. There is little redundant information, because at least three measurement points are needed to obtain a momentum measurement and the average number of Pixel hits per track is three in the barrel. Therefore, the Pixel track reconstruction efficiency is very sensitive to the location of inactive Pixel modules. The total distance between the first and the last measurement point in the pixel detector, as well as the limited number of measurement points per track, limit the momentum resolution of the tracks; therefore the Pixel tracks were refitted using the reconstructed primary vertex as an additional measurement point. The refitting improves the momentum resolution by almost a factor of two. However, the Pixel track momentum resolution remains a factor of three worse than the resolution of ID tracks.

The selection criteria used to define good Pixel and ID tracks are shown in table 3. The total numbers of accepted events and tracks at this energy are shown in table 4. These two track reconstruction methods have different limitations; the method with the best possible measurement for a given variable is chosen when producing the final plots. The Pixel track method is used for the n_{ch} and η distributions, while the ID track method is used for the p_T spectrum measurement; the $\langle p_T \rangle$ distribution is not produced for this energy as neither method is able to describe both the number of particles and their p_T accurately.

5. Background contribution

5.1. Event backgrounds

There are three possible sources of background events that can contaminate the selected sample: cosmic rays, beam-induced background and the presence of another collision inside the same bunch crossing. The fraction of cosmic ray background events was estimated in [1], where it was found to be smaller than 10^{-6}. Beam-induced backgrounds are estimated from non-colliding empty bunches using the same method as described in [1]; after final event selection, fewer than 0.1% of events are predicted to originate from beam-induced backgrounds. The reconstructed primary vertex requirement is particularly useful in suppressing the beam-induced background. The instantaneous luminosity at $\sqrt{s} = 7$ TeV is high enough that the effect of multiple collisions inside the same bunch crossing cannot be ignored. Events are rejected if they have a second vertex with four or more tracks[14]. After this cut, the fraction of events with more than one interaction in the same bunch crossing is measured to be about 0.1%; the residual effect is thus neglected. At the lower centre-of-mass energies, the rate of multiple interactions is lower and thus also neglected.

---

[13] A hole is defined as an absence of a hit when it is expected given the track trajectory.
[14] Events with two vertices with fewer than four tracks are dominated by events where a secondary interaction is reconstructed as another primary vertex and are thus not removed from our data samples.
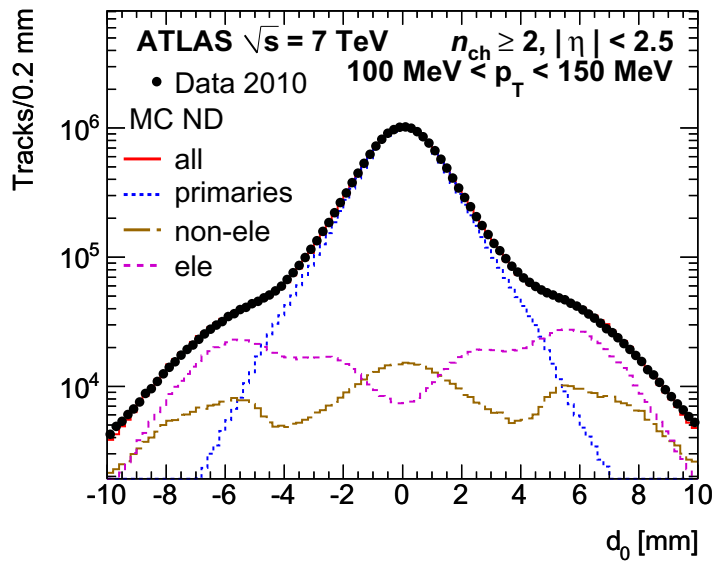
Figure 1. Transverse impact parameter, d_0, distribution at $\sqrt{s} = 7\,\mathrm{TeV}$ for primary (blue short-dashed) and non-primary particles after scaling them to the best fit value for $100 < p_\mathrm{T} < 150\,\mathrm{MeV}$. The non-primary particles are split into electrons (pink long-dashed) and non-electrons (green dot-dashed). The full red curve shows the ND MC prediction for the sum over the three components, which agrees well with the data (black points).

5.2. Backgrounds to primary tracks

Primary charged-particle multiplicities are measured from selected-track distributions after correcting for the fraction of non-primary particles in the sample. Non-primary tracks are mostly due to hadronic interactions, photon conversions and decays of long-lived particles, as well as a small fraction of fake tracks. Their contribution is estimated using MC predictions for the shape of the d_0 distribution for primaries, non-primaries from electrons and other non-primaries. The separation between non-primaries from electrons and non-electrons is needed as the electrons are mostly from conversions in the detector material and would thus be sensitive to a mismodelling of the detector material, whereas the non-electron non-primary tracks are mostly from long-lived particles and this fraction is thus also sensitive to the underlying physics. The Gaussian peak of the d_0 distribution, shown in figure 1 for $100 < p_\mathrm{T} < 150\,\mathrm{GeV}$, is dominated by the primary tracks and their resolution. The non-primary tracks populate the tails. The dominant contribution to non-primary tracks inside the acceptance cut on $|d_0|$ comes from non-electrons.

The primary, electron non-primary and non-electron non-primary d_0 distributions are obtained from MC and used as templates to extract the relative fractions in data. A fit is performed in the side-bands of the distribution, i.e. outside the range in d_0 used for selecting tracks. The fractions of primary, electron non-primary and non-electron non-primary tracks are all allowed to float with the total number of events constrained to that of the data. The contribution of non-primaries from electrons within the analysis acceptance of 1.5 mm is small, while it dominates at high values of $|d_0|$. The requirement on having a hit on layer-0 suppresses this contribution enough to allow the fit to be performed down to the lowest p_T region. The fit is performed in bins of 50 MeV in p_T from 100 to 500 MeV. A single fit is used for all tracks

IOP Institute of Physics ⬧ DEUTSCHE PHYSIKALISCHE GESELLSCHAFT

with $p_T > 500$ MeV; in this bin the distinction is not made between the two sources of non-primary tracks. The fraction of non-primary tracks varies from 3.4% for $100 < p_T < 150$ MeV to 1.6% above 500 MeV at $\sqrt{s} = 7$ TeV. Figure 1 shows the observed d_0 distribution for the bin $100 < p_T < 150$ MeV compared to the MC predictions after the fit.

5.2.1. Systematic uncertainties. The full difference between the non-primary fraction in MC and that in data obtained using the fit is taken as a systematic uncertainty. The largest difference is found to be an increase of non-primaries in data by 25% relative to the MC for $p_T > 500$ MeV. This conservative estimate is taken to be constant as a function of p_T and results in only a small effect, up to 0.9%, on the final corrected distributions. In order to estimate the effect of the choice of the variable used to obtain the fit, the fraction of primary and non-primary track contributions are obtained by fitting the z_0 distributions. The difference is measured to be 12% in the first bin, 8% in the last bin and less than 4% in all other bins; this difference is taken as a source of systematic uncertainty. The estimated number of non-primary tracks in $|d_0| < 1.5$ mm is found to be stable with respect to a change in the fit range of 1 mm in all p_T bins except the first one ($100 < p_T < 150$ MeV), where a 10% difference is observed; this difference is taken as a systematic uncertainty. The fraction of non-primary tracks is found to be independent of n_{sel}, but shows a small dependence on η, taken as a small systematic uncertainty of 0.1%.

The total uncertainty on the fraction of non-primary tracks is taken as the sum in quadrature of all these effects. The total relative uncertainty on the measured distributions at $\sqrt{s} = 0.9$ TeV and $\sqrt{s} = 7$ TeV is 1.0% for the first p_T bin, decreasing to 0.5% above 500 MeV. At $\sqrt{s} = 2.36$ TeV this uncertainty for the Pixel track method is 0.6%.

6. Selection efficiency

The data are corrected to obtain inclusive spectra for charged primary particles satisfying the different phase-space region requirements. These corrections include inefficiencies due to trigger selection, vertex and track reconstruction. They also account for effects due to the momentum scale and resolution and for the residual background from non-primary tracks.

In the following sections the methods used to obtain these efficiencies, as well as the systematic uncertainties associated with them, are described. Plots are shown for the phase-space region $n_{ch} \geqslant 2$, $p_T > 100$ MeV, $|\eta| < 2.5$ at $\sqrt{s} = 7$ TeV, but similar conclusions can be drawn at the other energies and phase-space regions.

6.1. Trigger efficiency

The trigger efficiency, ε_{trig}, is measured from a data sample selected using a control trigger. The control trigger used for this analysis selects events from random filled bunch crossings, which are then filtered at L2. At $\sqrt{s} = 0.9$ TeV the L2 filter requires a minimum of seven pixel clusters and seven SCT hits and the EF requires at least one track with $p_T > 200$ MeV. At $\sqrt{s} = 7$ TeV the L2 requirement is loosened to four pixel clusters and four SCT hits. No EF requirements are made at this energy. The vertex requirement for selected tracks is removed for these trigger studies, to account for correlations between the trigger and vertex reconstruction efficiencies. The trigger efficiency is determined by taking the ratio of events from the control trigger in which the L1 MBTS also accepted the event, over the total number of events in the control sample. For $\sqrt{s} = 2.36$ TeV there is not sufficient data to measure the trigger efficiency and thus the $\sqrt{s} = 0.9$ TeV parameterization is used to correct the 2.36 TeV data.
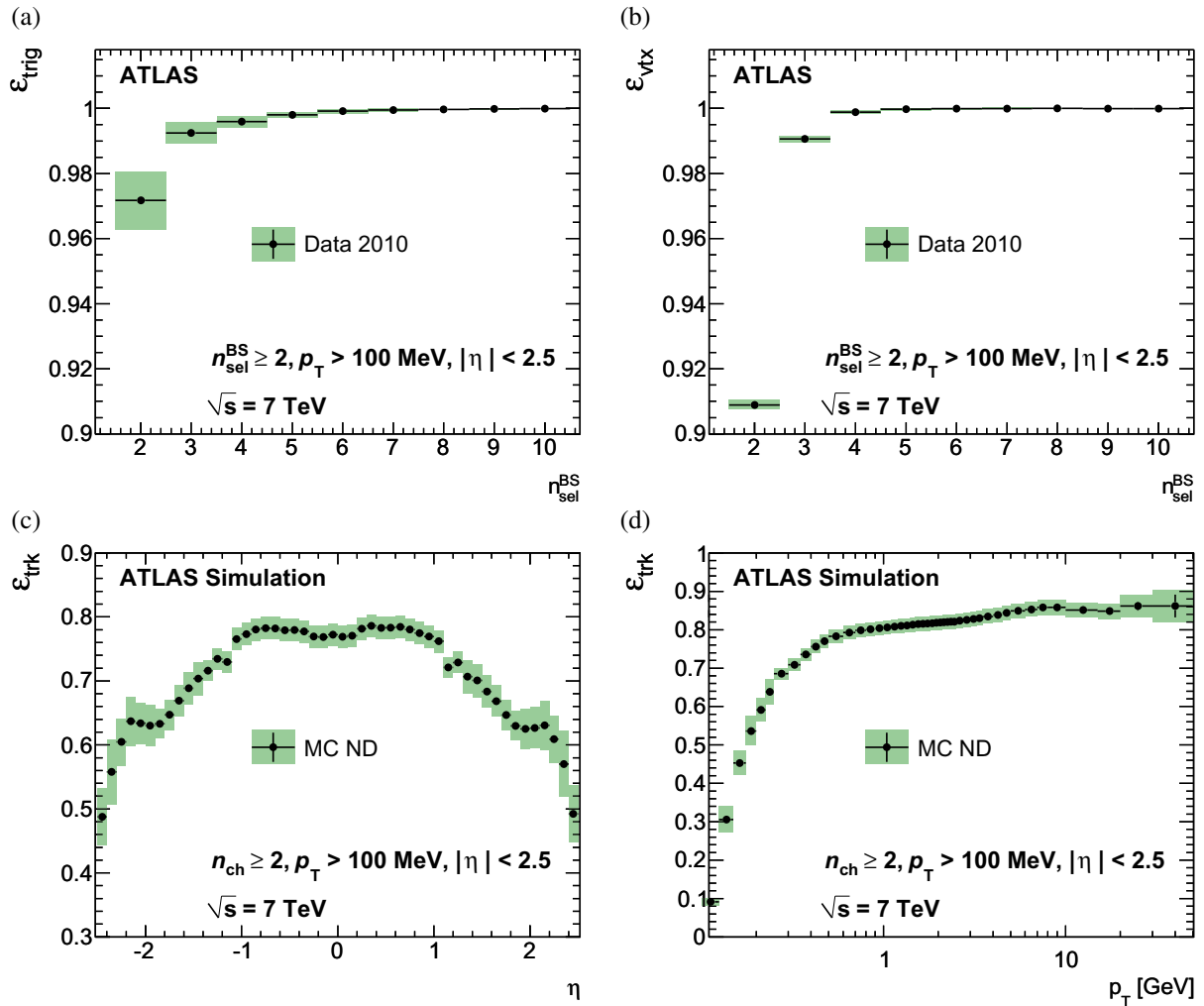
Figure 2. Trigger efficiency (a) and vertex reconstruction efficiency (b) with respect to the event selection, as a function of the number of reconstructed tracks before the vertex requirement (n_{sel}^{BS}). The track reconstruction efficiency as a function of η (c) and p_T (d) is derived from ND MC. The statistical errors are shown as black lines, the total errors as green shaded areas. All distributions are shown at $\sqrt{s} = 7$ TeV for $n_{ch} \geqslant 2$, $p_T > 100$ MeV, $|\eta| < 2.5$. For the vertex and trigger efficiencies, the selection requires $n_{sel}^{BS} \geqslant 2$.

The trigger efficiency is parameterized as a function of n_{sel}^{BS}; it is 97% (99%) in the first n_{sel}^{BS} bin and rapidly increases to nearly 100% for $n_{sel}^{BS} \geqslant 2$, $p_T > 100$ MeV ($n_{sel}^{BS} \geqslant 1$, $p_T > 500$ MeV). The trigger requirement is found to introduce no observable bias in the p_T and η distributions of selected tracks within the statistical uncertainties of the the data recorded with the control trigger. The resulting trigger efficiency is shown in figure 2(a) for the phase-space region with $n_{sel}^{BS} \geqslant 2$, $p_T > 100$ MeV at $\sqrt{s} = 7$ TeV.

Systematic uncertainties. Since there is no vertex requirement in the data sample used to measure the trigger efficiency, it is not possible to make the same impact-parameter selection as is made on the final selected tracks. In order to study potential effects due to this, the

trigger efficiency is measured after applying the impact-parameter constraints with respect to the primary vertex if available or with respect to the beam spot if not. The difference in the efficiency obtained this way and in the nominal way is considered as a systematic uncertainty. This variation provides a conservative estimate of the effect of beam-induced background and non-primary tracks on the trigger efficiency at low values of $n_{\rm sel}^{\rm BS}$. The systematic uncertainty arising from possible correlation of the MBTS trigger with the control trigger is studied using simulation, and the effect of correlations on the trigger efficiency is found to be less than 0.1%. The total systematic uncertainty on the trigger efficiency determination, which also includes the statistical uncertainty on the control sample, is of the order of 1% in the first $n_{\rm sel}^{\rm BS}$ bin, decreasing rapidly as $n_{\rm sel}^{\rm BS}$ increases.

6.2. Vertex reconstruction efficiency

The vertex reconstruction efficiency, $\varepsilon_{\rm vtx}$, is determined from data by taking the ratio of triggered events with a reconstructed vertex to the total number of triggered events, after removing the expected contribution from beam background events. The efficiency is measured to be 90–92% in the first $n_{\rm sel}^{\rm BS}$ bin for the different energies and phase-space regions; it rapidly rises to 100% at higher track multiplicities. The vertex reconstruction efficiency at $\sqrt{s} = 7\,{\rm TeV}$ for $n_{\rm sel}^{\rm BS} \geqslant 2$, $p_{\rm T} > 100\,{\rm MeV}$ is shown in figure 2(b) as a function of $n_{\rm sel}^{\rm BS}$.

The dependence of the vertex reconstruction efficiency on the η and $p_{\rm T}$ of the selected tracks is studied as well as the dependence on the projection along the beam-axis of the separation between the perigees[15] of the tracks (Δz), for events with more than one track. For all phase-space regions, only the dominant effect is corrected for as the other effect is always found to be significantly smaller and would thus not affect the final result.

For the lower $p_{\rm T}$ threshold selection, a strong dependence is observed as a function of Δz for events with two tracks; this bias is corrected for in the analysis using two different parameterizations depending on the $p_{\rm T}$ of the lowest $p_{\rm T}$ track: one for tracks below 200 MeV and one for those above that threshold. The dependence on the vertex reconstruction efficiency due to the η of the tracks is found to be smaller than the Δz correction and is neglected for this phase-space region. For the 500 MeV $p_{\rm T}$ threshold selection, the η dependence is corrected for events with $n_{\rm sel}^{\rm BS} = 1$. For events with higher multiplicities the Δz dependence is found to be very small and is neglected.

Systematic uncertainties. The difference between the vertex reconstruction efficiency measured with beam background removal and the vertex reconstruction efficiency measured without beam background removal is assigned as the systematic uncertainty on the vertex reconstruction efficiency. For the determination of this difference, the contribution of beam-related backgrounds is estimated using non-colliding bunches, as in [1]. The highest rate of beam-related background is found in the phase-space region with $p_{\rm T} > 100\,{\rm MeV}$ at 900 GeV, where it is 0.8% without vertex selection and 0.2% with vertex selection, although it is found to decrease rapidly at higher multiplicities. (This beam-related background contribution is larger than that given in section 5 where a reconstructed primary vertex was required.) The total uncertainty due to the vertex reconstruction efficiency is significantly below 1% for all phase-space regions at all energies. Figure 2(b) shows the total error for the phase-space region with $p_{\rm T} > 100\,{\rm MeV}$ at $\sqrt{s} = 7\,{\rm TeV}$.

---

[15] The perigee of a track is here the point of closest approach of the track and the coordinate origin (0,0,0).
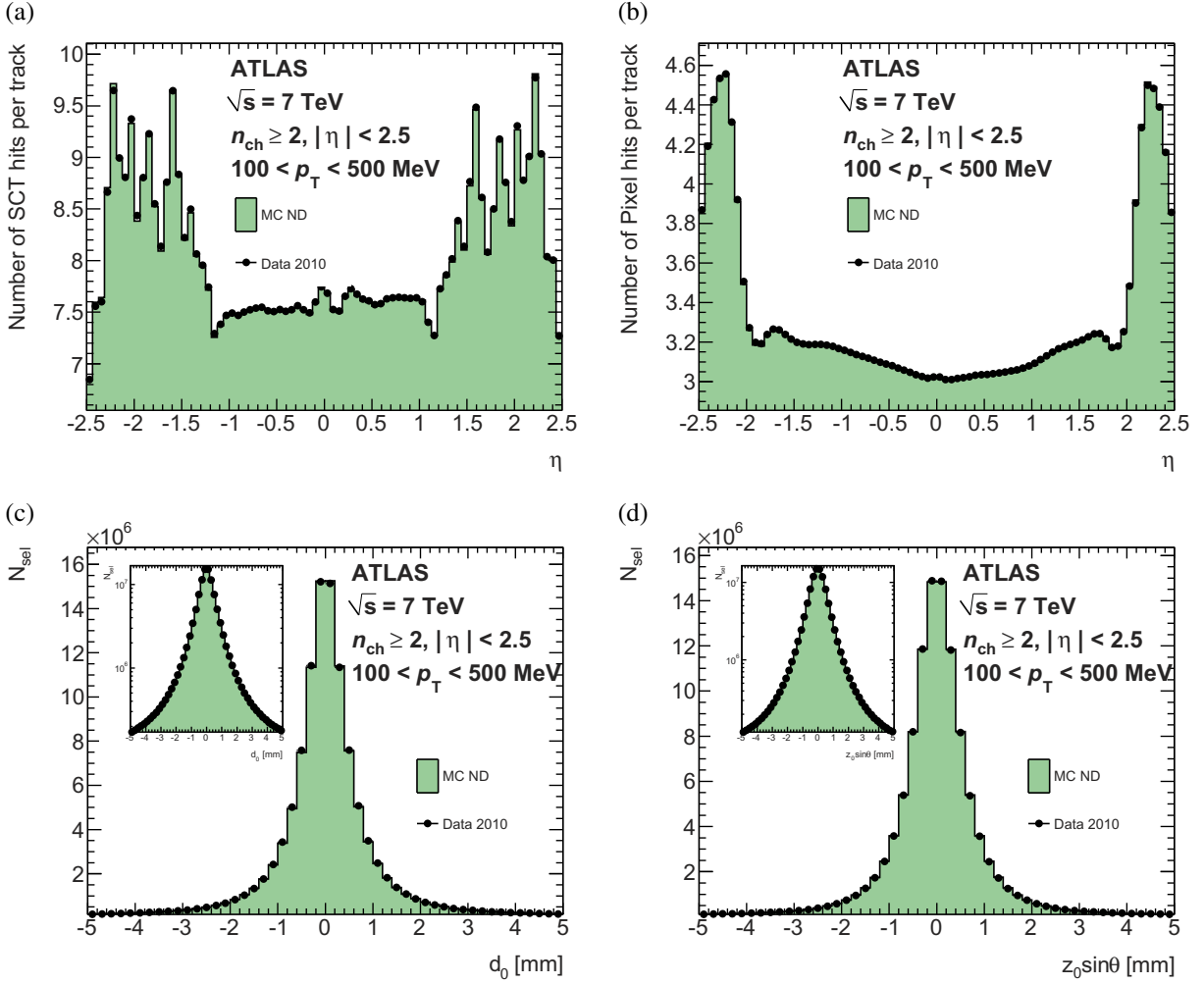
(a)

(b)

(c)

(d)

Figure 3. Comparison between data and simulation at $\sqrt{s} = 7\,\text{TeV}$ for tracks with transverse momentum between 100 and 500 MeV: the average number of silicon hits on reconstructed track as a function of η in the SCT (a) and Pixel (b) detectors, the transverse impact parameter (c) and the longitudinal impact parameter multiplied by $\sin\theta$ (d). The insets for the impact parameter plots show the log-scale plots. The p_T distribution of the tracks in ND MC is re-weighted to match the data and the number of events is scaled to the data.

6.3. Track-reconstruction efficiency for the 0.9 and 7 TeV data samples

The track reconstruction efficiency, ε_{trk}, determined from MC, is parameterized in bins of p_T and η. The excellent agreement between data and MC of basic track quantities for tracks above 500 MeV demonstrated previously [1]. Figure 3 highlights the agreement for tracks in the additional range covered in this paper, $100 < p_T < 500\,\text{MeV}$.

The track reconstruction efficiency is defined as

$$\varepsilon_{\text{trk}}(p_T, \eta) = \frac{N_{\text{rec}}^{\text{matched}}(p_T, \eta)}{N_{\text{gen}}(p_T, \eta)},$$

where p_T and η are generated particle properties, $N_{rec}^{matched}(p_T, \eta)$ is the number of reconstructed tracks matched to a generated charged particle and $N_{gen}(p_T, \eta)$ is the number of generated charged particles in that bin. The matching between a generated particle and a reconstructed track uses a cone-matching algorithm in the η–ϕ plane, associating the particle with the track with the smallest $\Delta R = \sqrt{(\Delta\phi)^2 + (\Delta\eta)^2}$ within a cone of radius 0.15. In addition, the particle trajectory must be compatible with the position of one of the pixel hits of the track. A larger cone size than in [1] is needed to account for the degraded resolution at lower track p_T.

The resulting reconstruction efficiency as a function of η integrated over p_T is shown in figure 2(c) at $\sqrt{s} = 7$ TeV for the phase-space region with the lowest p_T threshold. The track reconstruction efficiency is lower in the region $|\eta| > 1$ due to particles passing through more material in that region. Figure 2(d) shows the efficiency as a function of p_T integrated over η. The initial rise with p_T is due to the requirement on the minimum number of silicon hits required in the analysis, which indirectly constrains the tracks to pass through a minimum number of detector layers and thus have a minimum p_T.

Systematic uncertainties. As the track reconstruction efficiency is determined from MC, the main systematic uncertainties result from the level of agreement between data and MC. The overwhelming majority of particles in the selected events are hadrons. These are known to suffer from hadronic interactions with the material in the detector. Thus a good description of the material in the detector is needed to get a good description of the track reconstruction efficiency. To quantify the influence of an imperfect description of the detector description, in particular the material in the simulation, two different data-driven methods are used. The first reconstructs the invariant mass of K_s^0 mesons decaying to two charged pions; the second compares the track lengths in data and simulation. The K_s^0 mass method studies the mass as a function of the decay radius of the meson; it has greatest sensitivity to small radii, while the track length study probes the material description in the simulation in terms of nuclear interaction length (λ) in the SCT detector. The combination of both methods provides good sensitivity throughout the silicon detectors. They allow us to constrain the material to better than 10% in the central barrel region and better than 30% at the highest $|\eta|$ measured. The material uncertainty is the largest uncertainty in almost all regions of all distributions plotted in this paper. In the barrel region, the total uncertainty due to the material is 8% at low p_T, going down to 2% above 500 MeV. The uncertainty increases with increasing $|\eta|$; the largest uncertainties are in the region $2.3 < |\eta| < 2.5$: 15% in the first p_T bin decreasing to 7% above 500 MeV.

The track-fit χ^2 probability cut has been found to offer powerful discrimination against tracks with mismeasured momenta. These are mostly very low momentum particles that are reconstructed with much higher momentum due to misalignment or nuclear interactions[16]. Mismeasured tracks are seen predominantly at the edges of the η acceptance where the distance between consecutive measurement points of the outer layer of the Pixel and the first layer of the SCT can reach up to ~ 1 m. The fraction of mismeasured tracks is observed to be significantly more in data than in MC even after this cut is applied. Two different methods are used to estimate the fraction of mismeasured tracks in data. The first compares the momentum obtained from the tracks reconstructed using only the SCT hit information to that obtained for fully reconstructed tracks. After normalizing the number of well-measured tracks in MC to data, the scaling of the MC high-p_T tails needed to model the data is obtained. The second method uses

---

[16] Note that the momentum spectrum falls by many orders of magnitude in the measured range.

the difference between data and MC seen in the tails of the d_0 distributions at high p_T because mismeasured tracks tend to have poorly reconstructed d_0. Again a scaling factor is obtained to scale the MC tails in order to describe the data. These two methods give very similar results. Both methods are used to obtain the systematic uncertainty for all but the outermost regions in η where the effect is the most significant. In this region an additional method is used that compares the η distributions, normalized in the central region, in bins of p_T. The variation with p_T of the η distribution due to physics is small compared to the differences observed due to mismeasured tracks. The additional tracks at high $|\eta|$, high p_T are considered to be due to mismeasured tracks and the fraction of mismeasured tracks in data is obtained. This third method gives the systematic uncertainty for the outermost η bins. Averaged over the whole η region, the fraction of mismeasured tracks in data is found to be negligible for $p_T < 10\,\text{GeV}$, 3% for $10 < p_T < 15\,\text{GeV}$ and increases to 30% for $30 < p_T < 50\,\text{GeV}$. An additional systematic on the track reconstruction efficiency of 10% is taken for all tracks with $p_T > 10\,\text{GeV}$ due to different efficiencies of the χ^2 probability cut in data and MC. All systematic uncertainties on the mismeasured high-p_T tracks are taken as single-sided errors.

Studies using $Z \to \mu\mu$ events show that the resolution in data is about 10% worse than the nominal MC resolution above $10\,\text{GeV}$. The impact of a 10% Gaussian smearing of the reconstructed track p_T in MC is performed and found to have a 7% effect for the binning used in this paper. This effect is taken as a systematic uncertainty on tracks above $10\,\text{GeV}$. This systematic uncertainty is single-sided and added linearly with the systematic uncertainty due to the mismeasured high-p_T tracks. The effect on tracks below $10\,\text{GeV}$ is found to be negligible.

The p_T cut applied at various stages of the pattern recognition inside the track reconstruction algorithm introduces an inefficiency due to the momentum resolution. A different momentum resolution or a bias in the momentum estimation in data compared to MC can result in a change in the migration out of the first bin in p_T ($100 < p_T < 150\,\text{MeV}$) and thus a gain or loss of observed tracks. The default migration correction is derived using the resolution in MC. The track p_T resolution at the seed finding stage in MC is increased by a very conservative $10\,\text{MeV}$, making the p_T resolution effectively $15\,\text{MeV}$ instead of $10\,\text{MeV}$. The effect of this shift on the track reconstruction efficiency in the first p_T bin is found to be about 5%; this difference is assigned as a systematic uncertainty.

A detailed comparison of track properties in data and simulation is performed by varying the track selection criteria. The largest deviations between data and MC are observed at high η and are found to be $\sim 1\%$. For simplicity, a constant 1% uncertainty is assigned over the whole range.

A summary of the track reconstruction systematic uncertainties is shown in table 5. The total uncertainty due to the track reconstruction efficiency determination is obtained by adding all effects in quadrature except for tracks above $10\,\text{GeV}$ where the resolution and mismeasured track effects are added linearly; asymmetric errors are considered for these effects.

6.4. Track-reconstruction efficiency for the 2.36 TeV data sample

Both the Pixel track and the ID track methods apply a data-driven correction to the primary track reconstruction efficiency, ε_{MC}:

$$\varepsilon(x) = \varepsilon_{\text{MC}}(x) \cdot \varepsilon_{\text{corr}}(\eta), \tag{2}$$

Table 5. The systematic uncertainties on the track reconstruction efficiency for $\sqrt{s} = 0.9\,\mathrm{TeV}$, $\sqrt{s} = 7\,\mathrm{TeV}$ and $\sqrt{s} = 2.36\,\mathrm{TeV}$ Pixel track and ID track methods. Unless otherwise stated, the systematic is similar for all energies and phase-space regions. All uncertainties are quoted relative to the track reconstruction efficiency.

Systematic uncertainty	Size	Region
Material	± 2 to 15%	Decreases with p_T, increases with $|\eta|$
χ^2 prob. cut	$\pm 10\%$	Flat, only for $p_T > 10\,\mathrm{GeV}$
	$\pm 5\%$	$100 < p_T < 150\,\mathrm{MeV}$
Resolution	Negligible	$0.15 < p_T < 10\,\mathrm{GeV}$
	-7%	$p_T > 10\,\mathrm{GeV}$
Track selection	$\pm 1\%$	Flat in p_T and η
Truth matching	± 1	Only for $\sqrt{s} = 2.36\,\mathrm{TeV}$ Pixel tracks
Efficiency correction factor	± 4	Only for $\sqrt{s} = 2.36\,\mathrm{TeV}$ ID track
		Only for $p_T > 10\,\mathrm{GeV}$
Alignment and other high p_T	-3 to -30	Averaged over η, increases with increasing p_T

where $\varepsilon_{\mathrm{MC}}$ is derived from nominal simulation at $\sqrt{s} = 2.36\,\mathrm{TeV}$. Here x is either both p_T and η for the ID track or only η for the Pixel track method, as those are the parameters that the correction factors were found to depend on.

The correction, $\varepsilon_{\mathrm{corr}}$, is derived from the reference dataset taken at $\sqrt{s} = 0.9\,\mathrm{TeV}$ where the high voltage on the SCT was lowered for part of the run.

For the Pixel track method, $\varepsilon_{\mathrm{corr}}$ is the ratio of the relative Pixel track reconstruction efficiency, $\varepsilon_{\mathrm{rel}}$, in data to simulation. The relative Pixel track efficiency is the efficiency of reconstructing a Pixel track if a track has been reconstructed using hits in the SCT and TRT detectors only.

$$\varepsilon_{\mathrm{corr}}(\eta) = \frac{\varepsilon_{\mathrm{rel}}^{\mathrm{Data}}(\eta)}{\varepsilon_{\mathrm{rel}}^{\mathrm{MC}}(\eta)}. \tag{3}$$

Figure 4(a) shows the relative Pixel track efficiency in data and simulation. The ratio of the two distributions, shown in the inset, is used to correct the track reconstruction efficiency for the Pixel track method at $\sqrt{s} = 2.36\,\mathrm{TeV}$.

For the ID track method the efficiency derived from simulation with nominal conditions is corrected by $\varepsilon_{\mathrm{corr}}$ to account for the lower SCT efficiency in standby mode. Figure 4(b) shows the distribution of the number of reconstructed tracks in data in both SCT configurations at $\sqrt{s} = 0.9\,\mathrm{TeV}$ normalized to the same number of events satisfying the trigger requirement. The ratio of the number of reconstructed tracks with the SCT in standby, $N_{\mathrm{tr}}^{\mathrm{sb}}$, to the number of reconstructed tracks with the SCT at nominal, $N_{\mathrm{tr}}^{\mathrm{nom}}$, shown in the inset, is used to correct the track reconstruction efficiency for the ID track method at $\sqrt{s} = 2.36\,\mathrm{TeV}$:

$$\varepsilon_{\mathrm{corr}}(\eta) = \frac{N_{\mathrm{tr}}^{\mathrm{sb}}(\eta)}{N_{\mathrm{tr}}^{\mathrm{nom}}(\eta)}. \tag{4}$$

Systematic uncertainties. Most systematic uncertainties on the ID track reconstruction efficiency are similar to the full tracking at other energies. The major additional systematic uncertainty is
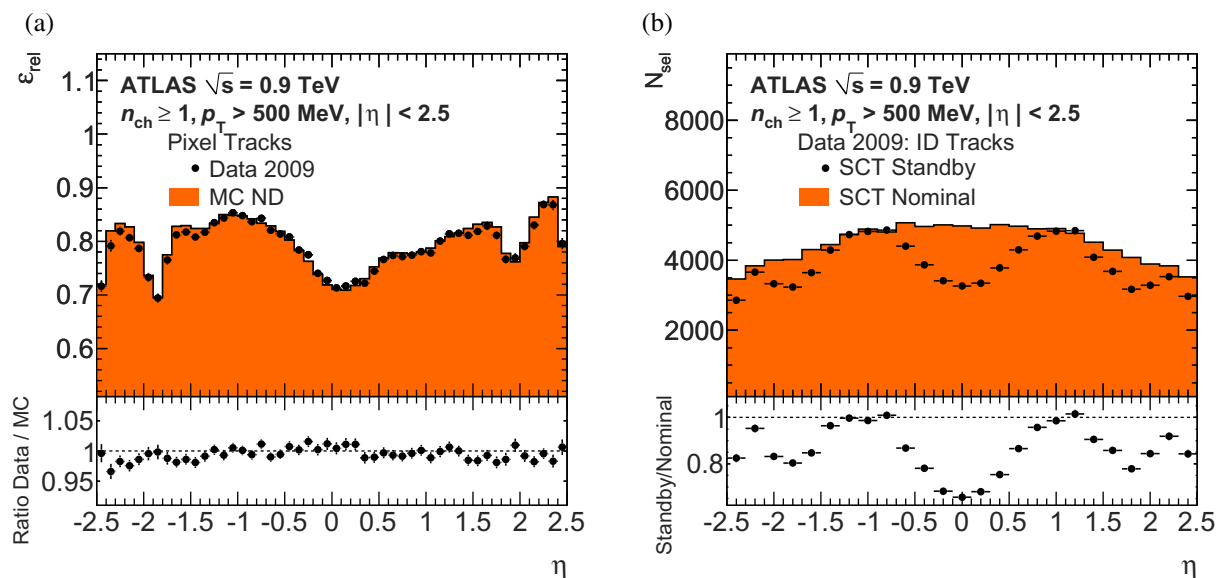
Figure 4. Relative efficiency of Pixel tracks in data and ND MC simulation at $\sqrt{s} = 0.9$ TeV (a). Both Pixel track distributions are re-weighted to have the same beam spot distribution as the $\sqrt{s} = 2.36$ TeV data. The number of reconstructed ID tracks in data at $\sqrt{s} = 0.9$ TeV as a function of η with the SCT in nominal and standby (b). The ID track distributions are normalized to the number of events passing the trigger requirement.

due to the efficiency correction factor for the SCT configuration. The uncertainty due to the statistical limitations of the reference dataset is 2%. An additional 3% uncertainty accounts for the extrapolation from $\sqrt{s} = 0.9$ TeV to $\sqrt{s} = 2.36$ TeV, which was estimated by comparing the distributions of the number of ID tracks between $\sqrt{s} = 0.9$ TeV and $\sqrt{s} = 2.36$ TeV. The total uncertainty on the efficiency correction factor adds those two effects in quadrature to obtain a total uncertainty of 4%.

The material uncertainty is estimated using a similar method as for the other energies; the absolute uncertainty is found to be 2% (3%) for the Pixel (ID) track reconstruction efficiency. The uncertainty is larger for ID tracks, because such tracks are sensitive to the material throughout the whole silicon detector. The uncertainty due to the momentum resolution is negligible because the phase-space cuts are sufficiently far from the track algorithm cuts.

There is an additional 1% uncertainty on the Pixel track method due to the matching procedure. The relative Pixel track reconstruction efficiency differs from the primary efficiency due to material effects and contributions from non-primary tracks. There is an additional discrepancy of 4% for $2.4 < |\eta| < 2.5$ that is assigned as a systematic uncertainty for those bins. At central η the total uncertainty on the Pixel (ID) track reconstruction efficiency is estimated to be 3.4% (6%). Table 5 shows the track reconstruction systematics at $\sqrt{s} = 2.36$ TeV, and the differences with respect to the uncertainties at other centre-of-mass energies are indicated.

7. Correction procedure

The effect of events lost due to the trigger and vertex requirements is corrected using an event-by-event weight:

$$w_{\text{ev}}(n_{\text{sel}}^{\text{BS}}) = \frac{1}{\varepsilon_{\text{trig}}(n_{\text{sel}}^{\text{BS}})} \cdot \frac{1}{\varepsilon_{\text{vtx}}(n_{\text{sel}}^{\text{BS}}, x)},$$

where x is either the Δz between tracks or the η of the tracks, as described in section 6.2.

The p_{T} and η distributions of selected tracks are corrected for using a track-by-track weight:

$$w_{\text{trk}}(p_{\text{T}}, \eta) = \frac{1}{\varepsilon_{\text{trk}}(p_{\text{T}}, \eta)} \cdot (1 - f_{\text{nonp}}(p_{\text{T}})) \cdot (1 - f_{\text{okr}}(p_{\text{T}}, \eta)),$$

where f_{nonp} is the fraction of non-primary tracks determined as described in section 5.

The fraction of selected tracks passing the kinematic selection for which the corresponding primary particle is outside the kinematic range, $f_{\text{okr}}(p_{\text{T}}, \eta)$, originates from resolution effects and has been estimated from MC. The uncertainty on f_{okr} is mostly due to the resolution difference between data and MC. This uncertainty is negligible for all cases except at $\sqrt{s} = 2.36 \, \text{TeV}$ for the Pixel track method where the uncertainty is estimated to be 1%, due to the poor momentum resolution of the Pixel tracks. No additional corrections are needed for the η distribution; the additional corrections needed for the other distributions are described in the following sections.

For all distributions in all phase-space regions considered, closure tests are carried out. These are tests carried out on MC where the reconstructed samples are corrected according to the same procedure as used on the data; the resulting difference between the corrected distribution and the known particle-level distribution is defined as the amount of non-closure; if the correction procedure were perfect, the non-closure would be zero. For this analysis, closure tests are carried out on all distributions in all phases-space regions and unless explicitly mentioned in the text the level of non-closure is less than 1%.

7.1. Correction to $\frac{\text{d}N_{\text{ev}}}{\text{d}n_{\text{ch}}}$

First, the observed n_{sel} distribution is corrected for the trigger and vertex reconstruction efficiencies. Then, an event-level correction is applied using Bayesian unfolding [46] to correct the observed track multiplicity to the distribution of the number of primary charged particles, as follows. An unfolding matrix, $M_{\text{ch,sel}}$, is defined that expresses the probability that a given selected track multiplicity, after all other event-level corrections are applied, n_{sel}, is due to n_{ch} primary particles. This matrix is normalized such that the number of events does not change except for the rare cases where $n_{\text{sel}} > n_{\text{ch}}$ and n_{ch} is below our acceptance selection. This matrix is populated from MC09 MC and applied to data in order to obtain the observed n_{ch} distribution. The resulting distribution is then used to re-populate the matrix and the correction is re-applied. This procedure is repeated without a regularization term and converges after four iterations in data; convergence is defined as the first iteration in which the χ^2 difference between the result of the unfolding and the input distribution for that iteration is less than the number of bins used in the unfolding.

After the n_{sel} distribution has been unfolded, the resulting charged-particle multiplicity distribution is corrected for events migrating out of the selected kinematic range ($n_{\text{ch}} \geqslant X$),

which the matrix does not account for. This is achieved by adding an additional term to the correction. The correction terms for the phase-space regions with $n_{\mathrm{ch}} \geqslant 2$ are

$$1/(1 - (1 - \varepsilon_{\mathrm{trk}})^{n_{\mathrm{ch}}} - n_{\mathrm{ch}} \cdot \varepsilon_{\mathrm{trk}} \cdot (1 - \varepsilon_{\mathrm{trk}})^{(n_{\mathrm{ch}}-1)}), \qquad (5)$$

where $\varepsilon_{\mathrm{trk}}$ is the mean effective track reconstruction efficiency for a given n_{ch} bin. Corresponding terms are used for the other phase-space regions. This track reconstruction efficiency can, in principle, be different for each n_{ch} bin, but the difference is found to be small and thus the mean effective track reconstruction efficiency for the lowest n_{ch} bin is used.

Systematic uncertainties. The systematic uncertainties on the unfolding procedure are obtained by modifying the input distributions as described below, applying the unfolding procedure and comparing the output to that obtained when using the nominal input; the matrix and the correction factors are not modified.

There are two sources of systematic uncertainties considered. One of them is due to the track reconstruction efficiency uncertainties, while the second one accounts for the different p_{T} spectra reconstructed in data and MC. The first source of uncertainty is estimated by starting from the observed n_{sel} spectrum in data; tracks are randomly removed from the distribution according to the mean p_{T} and η of the tracks for each value of n_{sel} and the uncertainty on the track reconstruction efficiency for those p_{T} and η values. A new input distribution is obtained and put through the unfolding procedure and the difference with respect to the nominal n_{ch} distribution is taken as a systematic uncertainty. The uncertainty is then symmetrized. The uncertainty on n_{ch} due to the uncertainty on the track reconstruction efficiency is found to be $\sim$ 3% to $\sim$25% at $\sqrt{s} = 7\,\mathrm{TeV}$ in the most inclusive phase-space region, $n_{\mathrm{ch}} \geqslant 2$, $p_{\mathrm{T}} > 100\,\mathrm{MeV}$, $|\eta| < 2.5$.

The other source of uncertainty originates from the unfolding method that is carried out in a single dimension at a time, in this case n_{ch}. There is some dependence on the p_{T} spectrum of the MC sample used to populate the matrix, due to the strong dependence of the track reconstruction efficiency on p_{T}. To investigate this effect, the average track reconstruction efficiency derived using the p_{T} spectrum in data and that obtained from MC are compared. The difference of these two mean efficiencies is then treated in the same way as the uncertainty on track reconstruction efficiency, described in the previous paragraph. This uncertainty is taken to be asymmetric; only the contribution from a shift of the spectrum in the direction of the data is taken. The mean value is kept as that given by the nominal p_{T} spectrum in MC. The uncertainty varies with increasing n_{ch} from -2% to $+40\%$ at $\sqrt{s} = 7\,\mathrm{TeV}$ in the most inclusive phase-space region.

The only additional systematic uncertainty due to the tuning of the track reconstruction efficiency is due to the difference between the biases introduced by the vertex correction in MC and data. The estimation of this error is done by comparing the Δz_0 distribution in $n_{\mathrm{sel}}^{\mathrm{BS}} = 2$ between data and MC. The Δz_0 distribution is a very good probe of the correlation between $n_{\mathrm{sel}}/n_{\mathrm{ch}}$ and $n_{\mathrm{sel}}^{\mathrm{BS}}$ as events with high n_{sel} tend to have small Δz_0 values, while events with $n_{\mathrm{sel}} < 2$ tend to have large Δz_0. Very good agreement is found between the data and MC. Re-weighting the Δz_0 distribution in MC to match the data or applying the vertex correction extracted from the data to the MC closure test leads to a systematic uncertainty of the order of 0.1% for $n_{\mathrm{ch}} = 2$ where this effect is most pronounced. As this error is much smaller than other systematic uncertainties considered, it is neglected. The systematic uncertainty due to track–track correlation in a single event is small and is neglected everywhere in this analysis.

7.2. Corrections to N_{ev}

The total number of events, N_{ev}, used to normalize the final distributions, is defined as the integral of the n_{ch} distributions, after all corrections are applied.

Systematic uncertainties. The systematic uncertainties on N_{ev} are obtained in the same way as for the n_{ch} distributions. Only those systematics affecting the events entering or leaving the phase-space region have an impact on N_{ev}. The total uncertainty on N_{ev} at $\sqrt{s} = 7$ TeV for the most inclusive phase-space region is 0.3%, due mostly to the track reconstruction efficiency. At $\sqrt{s} = 2.36$ TeV the total uncertainty on N_{ev} is 1.4% for the Pixel track and 2.6% for the ID track methods.

7.3. Corrections to $\frac{1}{p_T} \cdot \frac{dN_{ch}}{dp_T}$

The tracks are first corrected for the event level inefficiencies of the trigger and the vertex reconstruction. Then the tracks are corrected for the track reconstruction inefficiencies, non-primary track contamination and out of kinematic range factors. Finally, a similar unfolding method to that used on the n_{ch} distribution is used to correct the measured track p_T to the primary particle momentum. More bins are used for the unfolding than are shown in the final distributions; this is necessary in order to avoid amplification of small data MC differences with successive iterations, causing large fluctuations. For this distribution four iterations are required before convergence is reached; convergence is defined as for the n_{ch} distribution.

Systematic uncertainties. To estimate the effect on the final p_T distributions of the uncertainties affecting the correction steps prior to the unfolding, the unfolding procedure is re-run on the corrected p_T distribution shifting the distribution used as input to the unfolding procedure by the systematic uncertainties. This new p_T distribution is put through the unfolding procedure and the difference with respect to the nominal corrected p_T spectrum is taken as a systematic uncertainty.

   The high-p_T systematic uncertainties are obtained using the MC samples. The systematic uncertainty associated with the mismeasured high-p_T tracks is obtained by scaling the number of mismeasured tracks in MC to match those found in data. This new input distribution is put through the unfolding procedure and the final difference with respect to the nominal MC is taken as a systematic uncertainty. The systematic uncertainty associated with the resolution is obtained by smearing the well-measured tracks, in MC, by the resolution uncertainty obtained in section 6.3. The effect on the final unfolded distribution is taken as a systematic uncertainty. Those two high-p_T systematics are added linearly. Both cause only single-sided variations. This combined uncertainty is measured to be from -10% for $p_T = 10$ GeV to -30% for the last p_T bin ($30 < p_T < 50$ GeV) at $\sqrt{s} = 7$ TeV for the $n_{ch} \geqslant 2$, $p_T > 100$ MeV phase-space region. The variations for other phase-space regions at this energy are similar. At $\sqrt{s} = 0.9$ TeV this uncertainty is found to be -20% for all three bins above p_T of 10 GeV.

   To assess the stability of the results under varying starting hypotheses for the MC spectrum used to fill the matrix, a flat initial prior is used as an input. While convergence is only typically reached after seven iterations, instead of three for the nominal prior, the final difference in the unfolded spectra is small. The difference between the resulting distribution obtained with a flat prior and that obtained with the MC p_T spectrum as a prior is taken as a systematic uncertainty. At $\sqrt{s} = 7$ TeV this uncertainty is less than 2% for nearly all pT bins, with the exception of a couple of bins around changes in bin width, where the effect is 3–5%. At $\sqrt{s} = 0.9$ TeV, due to more limited statistics in the MC, the largest change seen is 7% with a few others around 3–4%.

7.4. Mean p_T versus n_{ch}

The correction procedure for the $\langle p_T \rangle$ versus n_{ch} distribution is designed to correct separately two components: $\sum_i p_T(i)$ versus n_{ch} and $\sum_i 1$ versus n_{ch} and take the ratio only after all corrections are applied. The sum is over all tracks and all events; the first sum is the total p_T of all tracks in that bin in n_{ch}; the second sum represents the total number of tracks in that bin. The sums will be referred to as the numerator and denominator, respectively. Each of these distributions, $\sum_i p_T(i)$ and $\sum_i 1$, is corrected in two steps.

Firstly, the two distributions as a function of n_{sel} are corrected on a track-by-track basis by applying the appropriate track weights; this track-by-track correction is applied to the data distribution and thus no longer relies on the p_T spectrum of the MC. Secondly, the matrix obtained after the final iteration of the n_{ch} unfolding described in section 7.1 is applied to each of the distributions to unfold n_{sel} to n_{ch}. Finally, the ratio of the two distributions is taken to obtain the corrected $\langle p_T \rangle$ versus n_{ch} distribution. For this distribution we exclude tracks with $p_T > \sqrt{s}/2$ as they are clearly unphysical; this removes 1 track at $\sqrt{s} = 0.9$ TeV and 1 track at $\sqrt{s} = 7$ TeV.

This unfolding procedure assumes that the tracking efficiency depends only on p_T and η and is independent of the track particle multiplicity and that the p_T spectrum of the tracks in events that migrate back from a given n_{sel} bin to a given n_{ch} bin is the same as the p_T spectrum of tracks in events in the corresponding n_{sel} bin. The fact that these assumptions are not completely valid is taken as a systematic uncertainty. This uncertainty is obtained by looking at the non-closure of the corrected distribution in the MC. This residual non-closure is, we believe, a consequence of the two main assumptions. A full parameterization of the track reconstruction efficiency in terms of p_T, η and n_{ch} would remove the need for the first assumption, while a full two-dimensional unfolding as a single step where the two dimensions were p_T and n_{ch} would remove the need for the second. Both of these are beyond the scope of the current paper. In order to understand if the amount of non-closure is a realistic estimate of the uncertainty on the method when applied to data, in particular to investigate its dependence on the p_T spectrum, the whole unfolding procedure is carried out using PYTHIA6 DW tune samples and the PYTHIA8 samples; we varied both the input distribution and the matrix used to do the unfolding. The level of non-closure is found to be similar to that obtained with the MC09 PYTHIA6 samples. We thus conclude that the level of non-closure is not strongly dependent on the p_T spectrum. This allows us to use the residual non-closure as a systematic uncertainty on the unfolding method as described in the next section.

Systematic and statistical uncertainties. For the calculation of the statistical uncertainty, the full correlation between the tracks inside the same event was not computed. The statistical uncertainty in the numerator and denominator are computed separately and then added in quadrature after taking the ratio. This is found to be a conservative estimate of the uncertainty.

Systematic uncertainties considered for the $\langle p_T \rangle$ versus n_{ch} distribution are either due to assumptions made during the correction procedure or to uncertainties on quantities taken from the MC and used during the correction procedure.

The first category refers to the assumptions on the method, the effects of which are visible in the closure test. To account for these imperfections, we apply a systematic uncertainty of 2%, which covers the non-closure in MC, except for the highest n_{ch} bin and the first few n_{ch} bins in some of the phase-space regions. For these cases a larger systematic uncertainty is applied to cover the non-closure. For the analyses with $p_T > 500$ MeV, where the size of a non-closure

is larger, a 3% systematic error is applied in the $n_{ch} = 1$ bin. This systematic uncertainty also covers the difference in non-closure between samples created using MC09 (default) and those with DW tune of PYTHIA6 and PYTHIA8. In the correction procedure we use the approximation that $n_{sel} = n_{sel}^{BS}$. The effect of such an approximation is studied on simulation and found to be negligible with respect to the other sources of uncertainty.

The second category comprises uncertainties on the track correction weights $w_{ev}(n_{sel}^{BS})$ and $w_{trk}(p_T, \eta)$ and on the migration probabilities obtained from the unfolding matrix. The dominant systematic uncertainties that affect both the track correction weights and the migration probabilities are the same as those affecting the n_{ch} distribution unfolding: the uncertainty on the track reconstruction efficiency and the effect of the difference in p_T spectra between the data and MC. These uncertainties are propagated by varying the input distribution for both $\sum_i p_T(i)$ versus n_{sel} and $\sum_i 1$ versus n_{sel}.

Smaller effects are also studied, for example the uncertainty on the rate of non-primary tracks and the effect of the systematic uncertainties affecting the high-p_T tracks mentioned in section 6.3. Excluding the systematic uncertainties due to the assumptions made during the correction procedure, the systematic uncertainties are between 0.5% and 2% for all bins in n_{ch}, all energies and all phase-space regions.

7.5. Correction for different minimum n_{ch} requirements

The only difference in the correction procedure from track to the particle level for $n_{ch} \geqslant 6$ with respect to $n_{ch} \geqslant 1$ is the need for an additional correction that takes into account the effect on the tracks due to the tighter cut on both the number of tracks and the number of particles.

The n_{ch} distribution and the number of events N_{ev} are obtained by correcting and unfolding the multiplicity distribution of the whole spectrum and then applying the higher n_{ch} cut on the final distribution. For the p_T and η track distributions an extra correction is needed. For events with $n_{sel} \geqslant 6$, the tracks are added to the distribution as for all other phase-space regions; a weight corresponding to the product of the track (w_{trk}) and event (w_{ev}) weights is applied. For events with $n_{sel} < 6$ the tracks are added to the distribution with an additional weighting factor, namely $w_{n_{ch}<6}$ that represents the probability that a track from an event with n_{sel} tracks is from an event with $n_{ch} \geqslant 6$. This additional weight is taken from the final n_{ch} unfolding matrix, after the final iteration; each column in the matrix represents the probability that an event with n_{sel} tracks has n_{ch} particles. The total probability ($p(n_{ch} \geqslant 6|n_{sel})$) for a given $n_{sel} < 6$ is therefore the sum over the matrix elements for $n_{ch} \geqslant 6$

$$w_{n_{ch}<6} = p(n_{ch} \geqslant 6|n_{sel}) = \sum_{n_{ch}\geqslant 6} M_{n_{ch},n_{sel}},$$

where $M_{n_{ch},n_{sel}}$ is the entry in the unfolding matrix for n_{ch} and n_{sel}. This weight is about 65% for $n_{sel} = 5$ and rapidly drops to 1% for $n_{sel} = 2$.

Systematic uncertainties. All uncertainties related to the distributions with the lower n_{ch} cut are taken into account. In addition, an extra systematic uncertainty due to the uncertainty on the track reconstruction efficiency is needed for the correction to higher n_{ch} selection. By varying the track reconstruction efficiency down by its uncertainty, different $w_{n_{ch}<6}$ weights are obtained. The shift in the resulting n_{ch} distribution is symmetrized and taken as an additional systematic uncertainty.

7.6. Extrapolation to $p_T = 0$

Comparing the results in our well-defined phase-space regions to other inclusive measurements from other experiments requires additional model-dependent corrections. One such correction is described here, but applied only for comparative purposes. This particular correction is derived to extrapolate the average multiplicity in the phase-space region with the lowest measured p_T to the multiplicity for all $p_T > 0$. No attempt is made to correct for the $n_{ch} \geqslant 2$ requirement. The results are quoted for the average multiplicity in the rapidity interval $|\eta| < 2.5$ and are not considered to be the main results of this paper. This correction is obtained using three independent methods: fitting the p_T spectrum to a given functional form, assuming a flat distribution at low p_T in the observed fully corrected $\frac{1}{p_T} \cdot \frac{dN_{ch}}{dp_T}$ distribution and obtaining the correction factor from the AMBT1 PYTHIA6 MC.

In the first method, the corrected p_T spectrum is fitted with a two-component Tsallis distribution

$$f(p_T) = \frac{1}{2\pi\eta'} \sum_{i=\pi,p} \frac{dN_{ch}}{dy}\bigg|_{y=0,i} \frac{(n_i-1)(n_i-2)}{(n_i T_i + m_{0,i}(n_i-1))(n_i T_i + m_{0,i})} \left[\frac{n_i T_i + m_T(p_T)_i}{n_i T_i + m_{0,i}}\right]^{-n_i}$$

$$\times \tanh^{-1}\left(\frac{p_T \sinh\eta'}{\sqrt{m_{0,i}^2 + p_T^2 \cosh^2\eta'}}\right)\bigg|_{\eta'=2.5},$$

where $m_T(p_T)$ is the transverse mass $m_T = \sqrt{p_T^2 + m_0^2}$ and m_0 is the particle rest mass $m_0 = \{m_\pi, m_p\}$ and $dN_{ch}/dy|_{y=0,i}$, T_i and n_i are the six parameters of the fit. η' represents the pseudorapidity at the edge of our acceptance, $\eta = 2.5$. $dN_{ch}/dy|_{y=0}$ represents the integrated yield of the particle production at mid-rapidity, but is left here as a free parameter of the fit. Mesons (pions and kaons) are merged into a single Tsallis function since there is insufficient information in the measured distribution to fit three independent shapes. The $\tanh^{-1}$ factor accounts for the variation in E/p of each track over the entire measured pseudorapidity range. It is derived by integrating $\frac{dy}{d\eta}d\eta$ over $|\eta| < 2.5$.

From this functional form and using the parameters obtained from the fit, the fraction of particles with $p_T < 100$ MeV is extracted. This procedure gives the correction factor to be applied to the mean charged-particle multiplicity per unit η, averaged over $|\eta| < 2.5$, in order to get the inclusive multiplicity. The correction factor from $p_T > 100$ MeV to $p_T > 0$ MeV is found to be 1.065 at $\sqrt{s} = 0.9$ TeV and 1.063 at $\sqrt{s} = 7$ TeV.

The second method assumes that the $\frac{1}{p_T} \cdot \frac{dN_{ch}}{dp_T}$ distribution is flat at low p_T. One can thus use the value of this distribution in the lowest p_T bin ($100 < p_T < 150$ MeV) to extract the value for tracks below 100 MeV. From this assumption, the fraction of particles below 100 MeV and the scale factor used to correct our observed distributions are derived. The scale factors are found to be 1.068 at $\sqrt{s} = 0.9$ TeV and 1.065 at $\sqrt{s} = 7$ TeV. The third and final method simply obtains the correction factor using one of the MC models. AMBT1 PYTHIA6 is chosen; the correction factors are found to be 1.055 at $\sqrt{s} = 0.9$ TeV and 1.051 at $\sqrt{s} = 7$ TeV. We chose to use the scale factor obtained from the functional form fit as the central value and consider the difference between this and the other two methods as a systematic uncertainty.

Systematic uncertainties. Several sources of systematic uncertainty on the calculated scale factor are considered. The dominant uncertainty comes from the difference in the scale factors

obtained from the three different extrapolation methods. The largest difference between the value obtained from the fit and the values from the MC and from the flat extrapolation is considered as the uncertainty and then symmetrized. This uncertainty is found to be 0.007 at $\sqrt{s} = 0.9\,\text{TeV}$ and 0.012 at $\sqrt{s} = 7\,\text{TeV}$.

The other sources of uncertainty are related to the fitting procedure such as the variation within the uncertainty on the fit parameters and the variation due to a change of the fit range. All sources of uncertainty are assumed to be uncorrelated and thus added in quadrature. The final scale factors, with total uncertainty, are then $1.063 \pm 0.014_{\text{tot}}$ at $\sqrt{s} = 7\,\text{TeV}$ and $1.065 \pm 0.011_{\text{tot}}$ at $\sqrt{s} = 0.9\,\text{TeV}$.

8. Total systematic uncertainties

The individual sources of systematic uncertainties have already been discussed in previous sections. The effect on the final distribution from each source is treated independently and propagated to the final distributions; the total error is the sum in quadrature from the different sources, unless explicitly mentioned in the text. In most bins of all distributions the largest uncertainty comes from the track reconstruction efficiency. The uncertainties at $\sqrt{s} = 2.36\,\text{TeV}$ are larger than at the other two energies due to the uncertainties related to the operation of the SCT at reduced bias voltage during 2.36 TeV data taking. The total uncertainties are shown as shaded bands in the final distributions presented in the next section.

9. Results and discussion

The corrected distributions for primary charged particles for events in three separate phase-space regions are shown in figures 5–13. The results are compared with predictions of models tuned to a wide range of measurements. The measured distributions are presented as inclusive-inelastic distributions within a given phase-space region with minimal model-dependent corrections to facilitate the comparison with models.

9.1. Charged-particle multiplicities as a function of the pseudorapidity

Figures 5 and 6 show the charged-particle multiplicity as a function of pseudorapidity. Figure 5 shows the distribution at all three centre-of-mass energies in the phase-space region, $n_{\text{ch}} \geqslant 1$, $p_{\text{T}} > 500\,\text{MeV}$, $|\eta| < 2.5$. The mean particle density is roughly constant for $|\eta| < 1.0$ and decreases at higher values of $|\eta|$. There is little shape variation between the models except for the DW PYTHIA6 tune, which has a flatter spectrum and a more pronounced dip at central η, especially at low $\sqrt{s}$. At all three energies the AMBT1 PYTHIA6 tune gives the best shape and normalization description of the data, although it was tuned for $n_{\text{ch}} \geqslant 6$.

Figures 6(a) and (b) show the η distributions for the most inclusive phase-space region, $n_{\text{ch}} \geqslant 2$, $p_{\text{T}} > 100\,\text{MeV}$, $|\eta| < 2.5$. There is less η variation than in the previous figure. At 900 GeV there is very little difference between the models both in shape and normalization with the exception of PHOJET, which shows excellent agreement with the data; the other models show on average too few particles. The shape of the distribution is reasonably well described by all models. At 7 TeV again all the shapes seem to model the observed spectrum reasonably well, but at this energy the difference in normalization among the models varies more widely and no model reproduces the data.
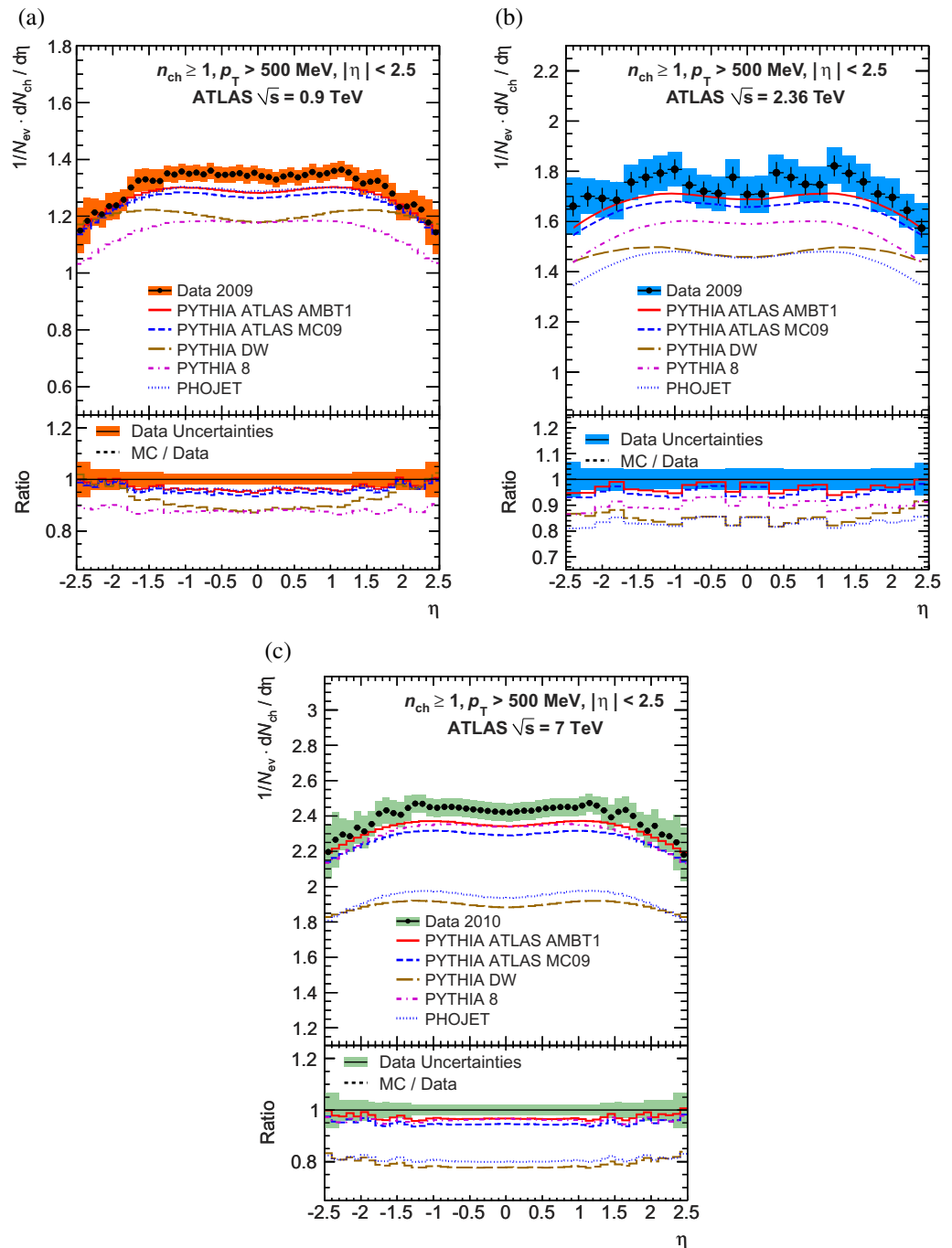
IOP Institute of Physics Φ DEUTSCHE PHYSIKALISCHE GESELLSCHAFT

Figure 5. Charged-particle multiplicities as a function of the pseudorapidity for events with $n_{ch} \geqslant 1$, $p_T > 500\,\text{MeV}$ and $|\eta| < 2.5$ at $\sqrt{s} = 0.9\,\text{TeV}$ (a), $\sqrt{s} = 2.36\,\text{TeV}$ (b) and $\sqrt{s} = 7\,\text{TeV}$ (c). The dots represent the data and the curves the predictions from different MC models. The vertical bars represent the statistical uncertainties, whereas the shaded areas show statistical and systematic uncertainties added in quadrature. The bottom insets show the ratio of the MC to the data. The values of the ratio histograms refer to the bin centroids.
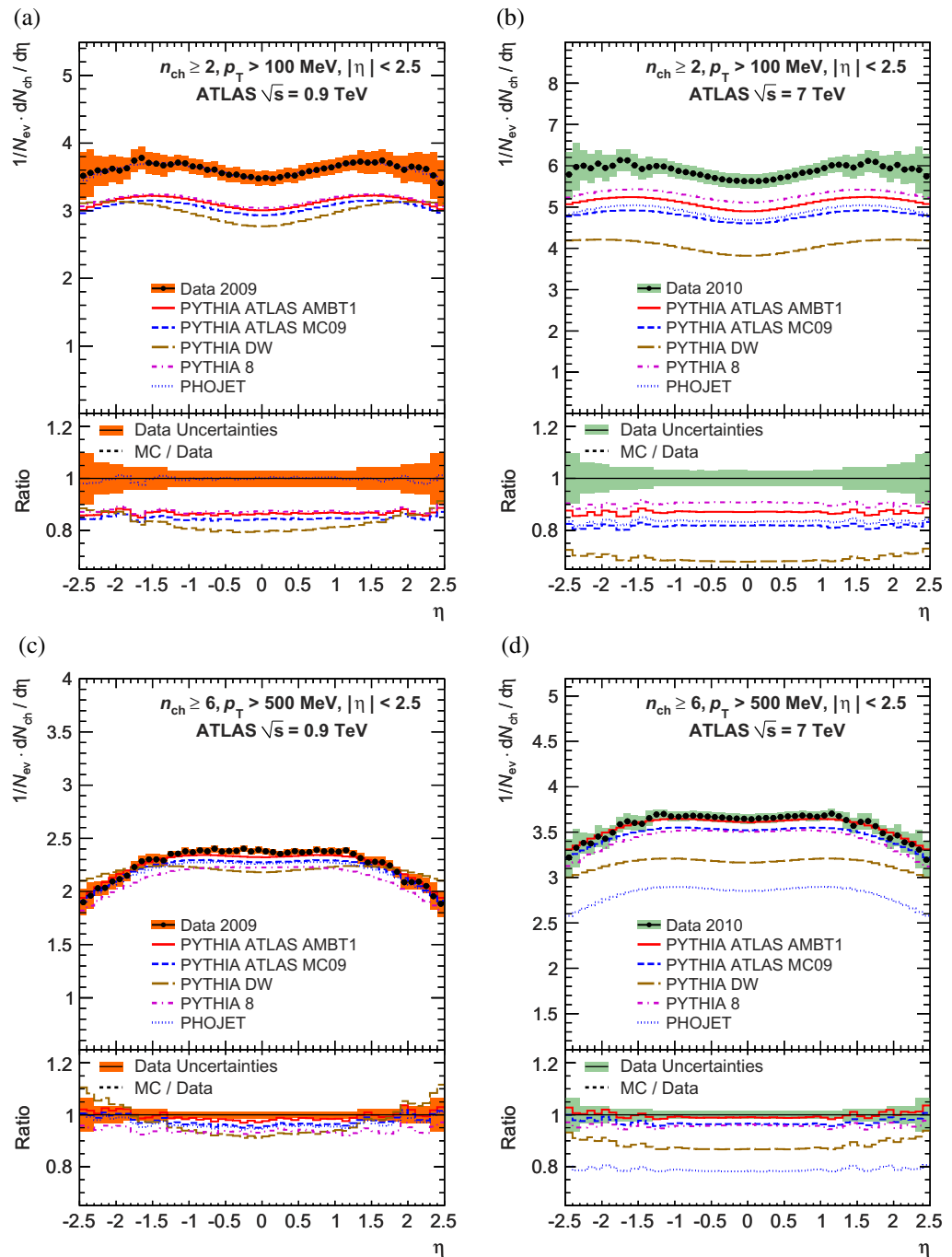
Figure 6. Charged-particle multiplicities as a function of the pseudorapidity for events with $n_{ch} \geqslant 2$, $p_T > 100$ MeV (a, b) and $n_{ch} \geqslant 6$, $p_T > 500$ MeV (c, d) and $|\eta| < 2.5$ at $\sqrt{s} = 0.9$ TeV (a, c) and $\sqrt{s} = 7$ TeV (b, d). The dots represent the data and the curves the predictions from different MC models. The vertical bars represent the statistical uncertainties, while the shaded areas show statistical and systematic uncertainties added in quadrature. The bottom insets show the ratio of the MC to the data. The values of the ratio histograms refer to the bin centroids.

Figures 6(c) and (d) show the η distributions for the phase-space region with the least amount of diffraction, $n_{ch} \geqslant 6$, $p_T > 500\,\text{MeV}$, $|\eta| < 2.5$. The distributions in this phase-space region have the largest drop at high $|\eta|$. All but PYTHIA6 DW and PHOJET at $\sqrt{s} = 7\,\text{TeV}$ show reasonable agreement in both shape and normalization at both energies.

9.2. Charged-particle multiplicities as a function of the transverse momentum

Figures 7 and 8 show the charged-particle multiplicities as a function of the transverse momentum. The first of these figures shows all three centre-of-mass energies considered in the phase-space region $n_{ch} \geqslant 1$, $p_T > 500\,\text{MeV}$ and $|\eta| < 2.5$. The observed p_T spectrum is not described by any of the models over the whole range. The region that the models have the most difficulty describing is the region above $1\,\text{GeV}$.

Figures 8(a) and (b) show the charged-particle multiplicities in the most inclusive phase-space region. At $900\,\text{GeV}$ PHOJET describes the data best over the whole range even though the agreement is still not excellent. The other models tend to underpredict the number of low-p_T particles, while at higher p_T the models vary widely. At $7\,\text{TeV}$ the effect at low p_T is more pronounced, whereas at high p_T the agreement of PYTHIA8 and PHOJET with the data is quite good. The AMBT1 and MC09 tunes of PYTHIA6 predict too many particles at higher p_T.

Figures 8(c) and (d) show the charged-particle multiplicities with the smallest contribution from diffractive events. This distribution carried the most weight in the AMBT1 tune. Considerable improvement in the agreement with data is seen between the older MC09 and the newly tuned AMBT1 but the parameters varied in this tune were not sufficient to describe the full spectrum.

9.3. Charged-particle multiplicity distribution

Figure 9 shows the charged-particle multiplicity distributions for $n_{ch} \geqslant 1$, $p_T > 500\,\text{MeV}$ and $|\eta| < 2.5$ at all three centre-of-mass energies. At low number of charged particles, all models predict more events than observed in data, which is compensated for by an underprediction in the tails of the distributions. It should be noted that due to the normalization, $1/N_{ev}$, a deviation observed in one region needs to be compensated for by one in the other direction somewhere else. Although the predictions of PHOJET at $0.9\,\text{TeV}$ model the data reasonably well, at 2.36 and $7\,\text{TeV}$ they do not model the observed spectrum. The new AMBT1 PYTHIA6 tune seems to provide the best agreement with data.

Figures 10(a) and (b) show the distribution for the most inclusive phase-space region. Here the variations between models at both low and high values of n_{ch} are increased and no model predicts the observed spectra.

Figures 10(c) and (d) show the distribution for the diffraction-reduced phase-space region. The distributions are very similar to those in figure 9 with a cut at $n_{ch} \geqslant 6$; only the normalization is different between the plots. The errors are also recomputed as there is a larger cancellation between the numerator and the denominator for this phase-space region.

9.4. Average transverse momentum as a function of the number of charged particles

The final set of distributions discussed in the main part of this paper is the average transverse momentum as a function of particle multiplicity. The measurement of $\langle p_T \rangle$ as a function of
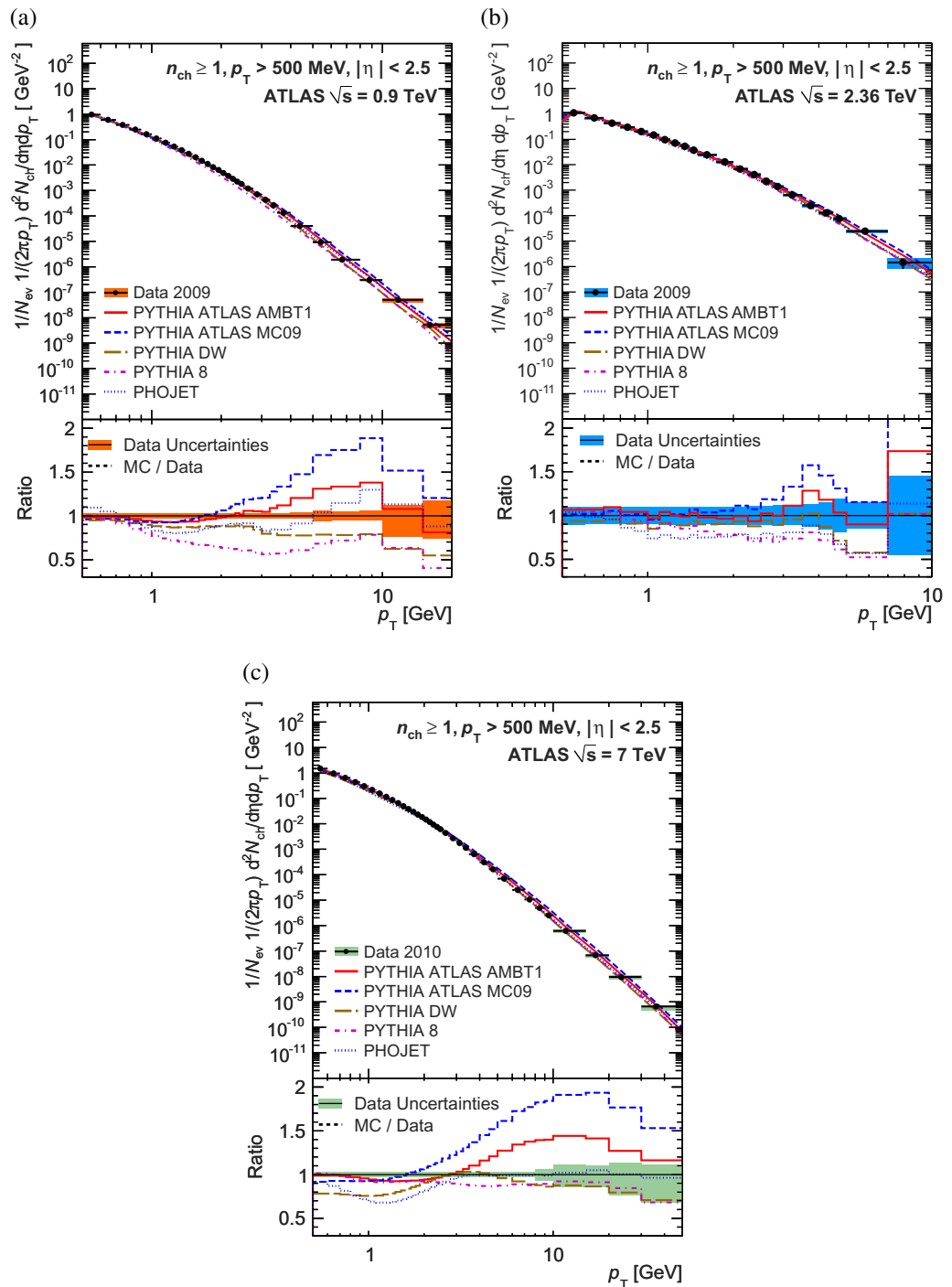
Figure 7. Charged-particle multiplicities as a function of the transverse momentum for events with $n_{ch} \geqslant 1$, $p_T > 500\,\text{MeV}$ and $|\eta| < 2.5$ at $\sqrt{s} = 0.9\,\text{TeV}$ (a), $\sqrt{s} = 2.36\,\text{TeV}$ (b) and $\sqrt{s} = 7\,\text{TeV}$ (c). The dots represent the data and the curves the predictions from different MC models. The vertical bars represent the statistical uncertainties, while the shaded areas show statistical and systematic uncertainties added in quadrature. The bottom insets show the ratio of the MC to the data. The values of the ratio histograms refer to the bin centroids.
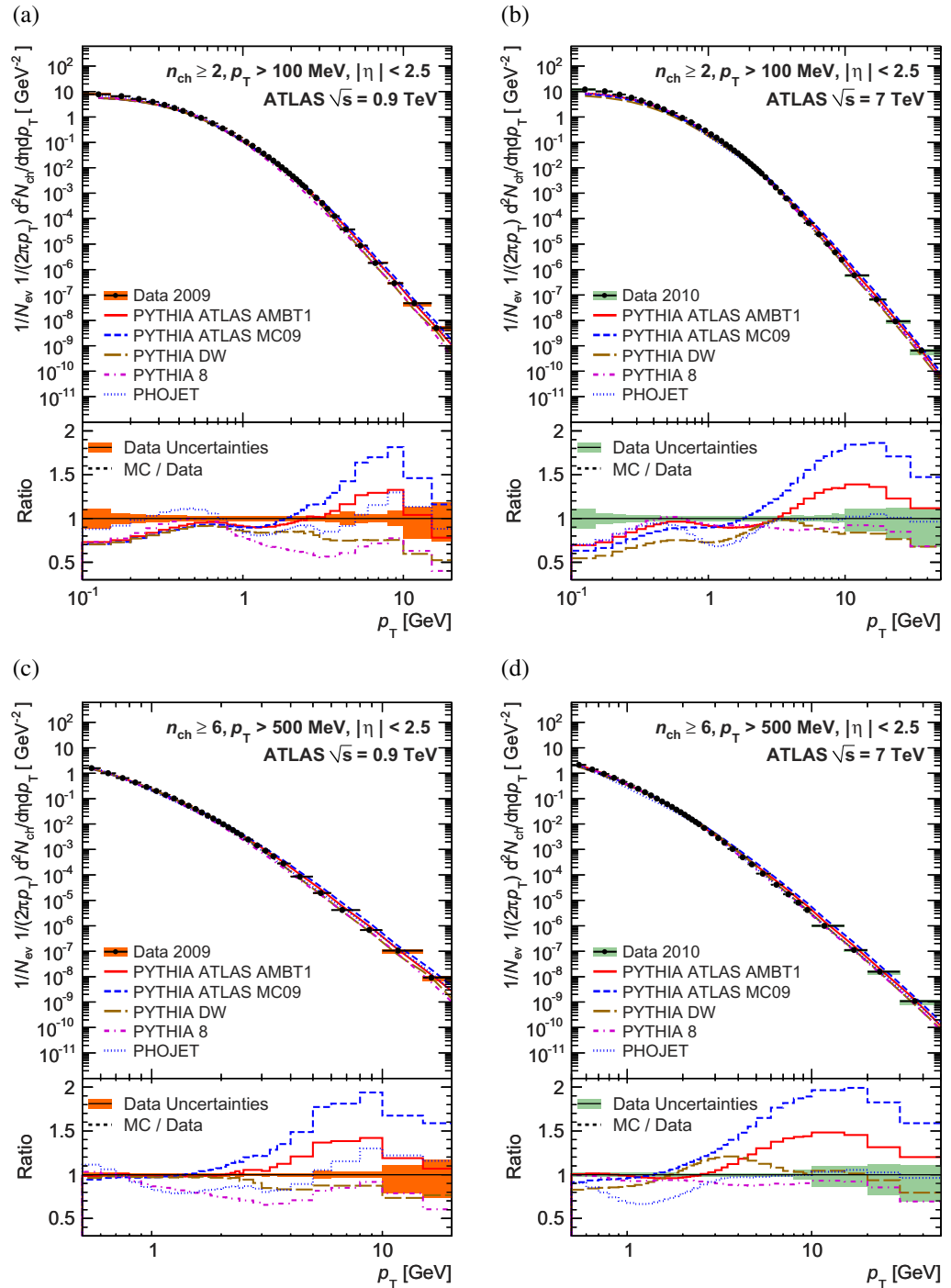
Figure 8. Charged-particle multiplicities as a function of the transverse momentum for events with $n_{ch} \geqslant 2$, $p_T > 100\,\text{MeV}$ (a, b) and $n_{ch} \geqslant 6$, $p_T > 500\,\text{MeV}$ (c, d) and $|\eta| < 2.5$ at $\sqrt{s} = 0.9\,\text{TeV}$ (a, c) and $\sqrt{s} = 7\,\text{TeV}$ (b, d). The dots represent the data and the curves the predictions from different MC models. The vertical bars represent the statistical uncertainties, while the shaded areas show statistical and systematic uncertainties added in quadrature. The bottom insets show the ratio of the MC to the data. The values of the ratio histograms refer to the bin centroids.

(a)

(b)

(c)

Figure 9. Charged-particle multiplicity distributions for events with $n_{ch} \geqslant 1$, $p_T > 500$ MeV and $|\eta| < 2.5$ at $\sqrt{s} = 0.9$ TeV (a), $\sqrt{s} = 2.36$ TeV (b) and $\sqrt{s} = 7$ TeV (c). The dots represent the data and the curves the predictions from different MC models. The vertical bars represent the statistical uncertainties, while the shaded areas show statistical and systematic uncertainties added in quadrature. The bottom insets show the ratio of the MC to the data. The values of the ratio histograms refer to the bin centroids.
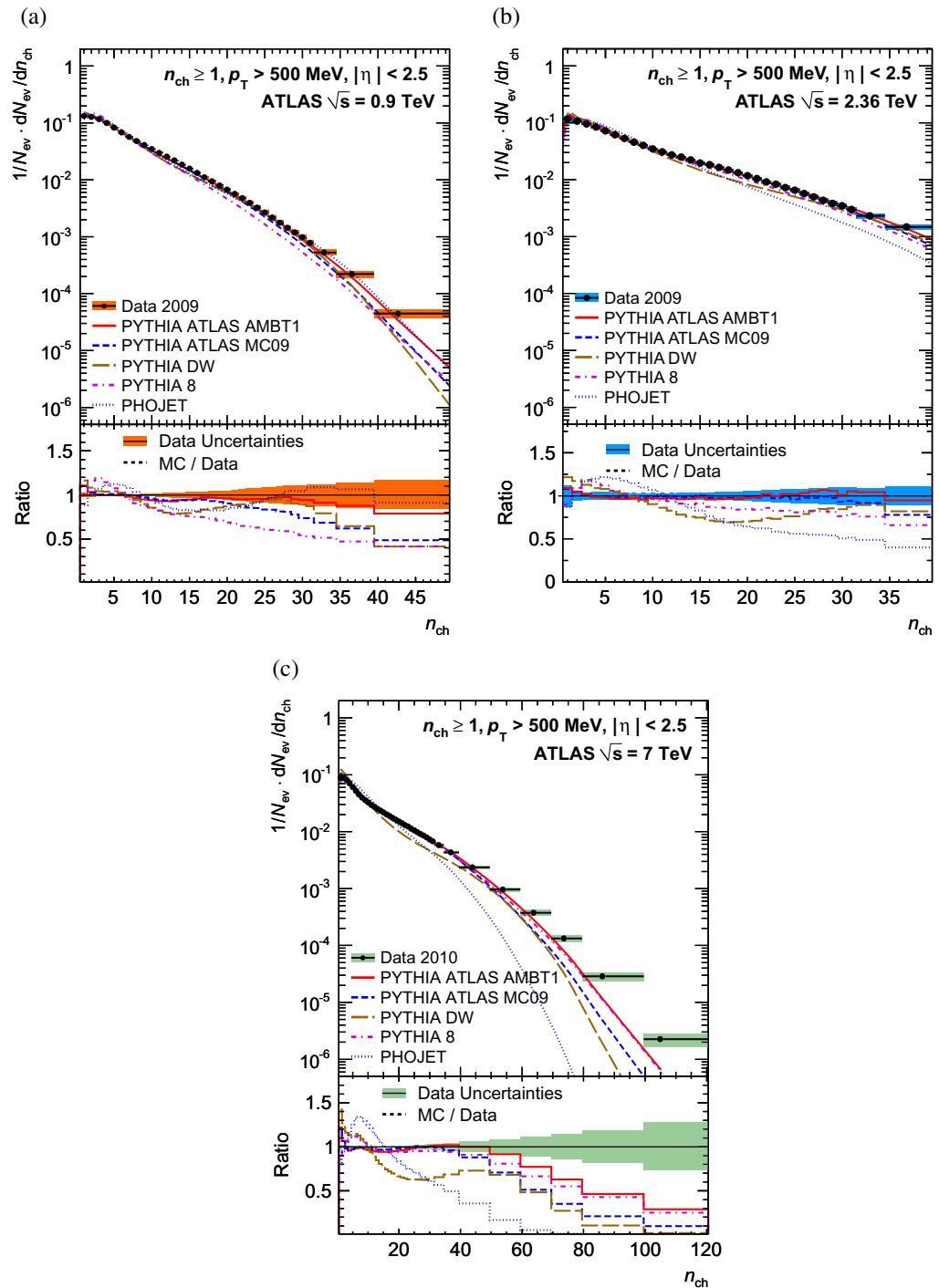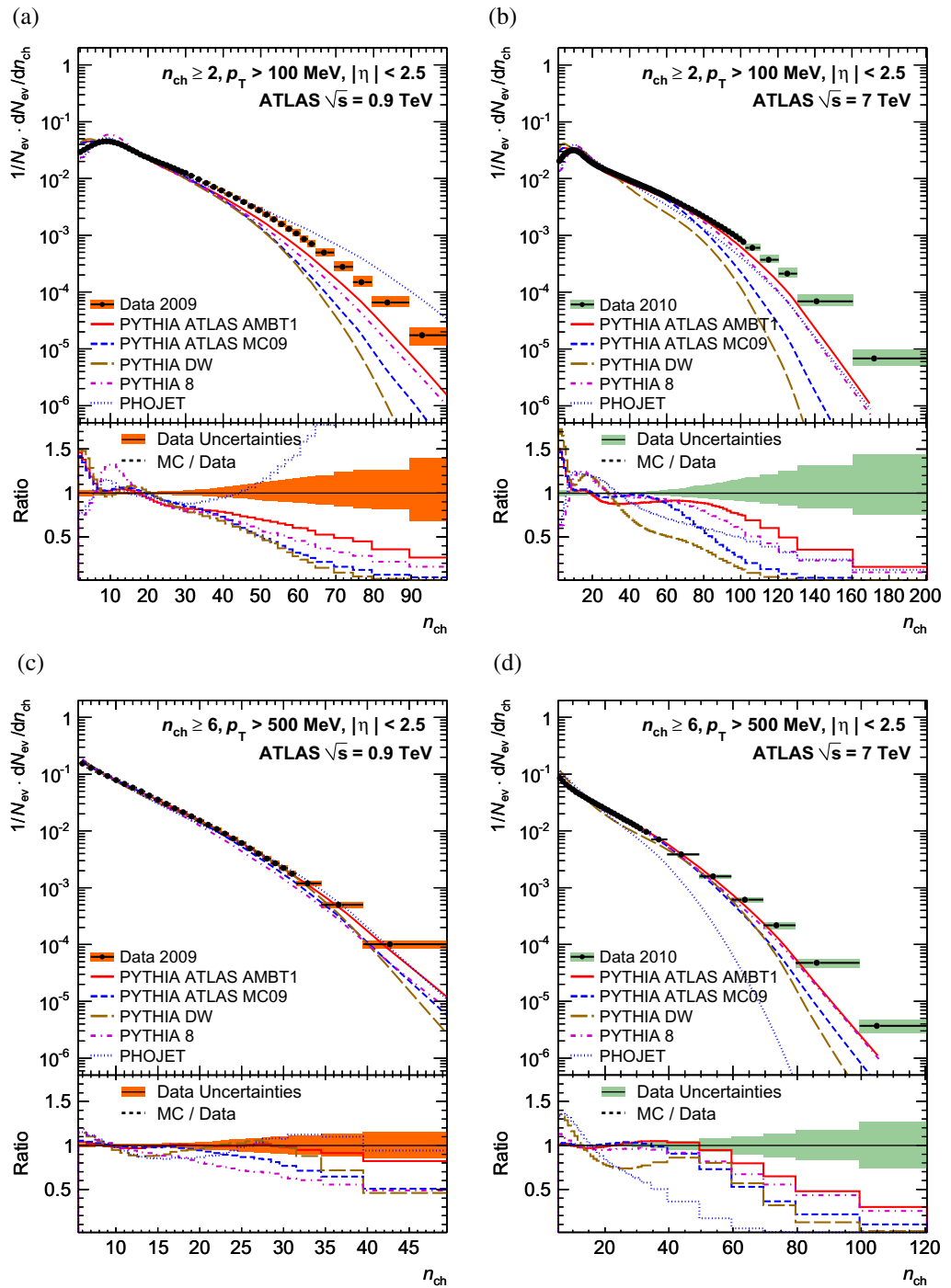
Figure 10. Charged-particle multiplicity distributions for events with $n_{ch} \geqslant 2$, $p_T > 100$ MeV (a, b) and $n_{ch} \geqslant 6$, $p_T > 500$ MeV (c, d) and $|\eta| < 2.5$ at $\sqrt{s} = 0.9$ TeV (a, c) and $\sqrt{s} = 7$ TeV (b, d). The dots represent the data and the curves the predictions from different MC models. The vertical bars represent the statistical uncertainties, while the shaded areas show statistical and systematic uncertainties added in quadrature. The bottom insets show the ratio of the MC to the data. The values of the ratio histograms refer to the bin centroids.

Figure 11. Average transverse momentum as a function of the number of charged particles in the event for events with $n_{ch} \geqslant 1$, $p_T > 500$ MeV and $|\eta| < 2.5$ at $\sqrt{s} = 0.9$ TeV (a) and $\sqrt{s} = 7$ TeV (b). The dots represent the data and the curves the predictions from different MC models. The vertical bars represent the statistical uncertainties, while the shaded areas show statistical and systematic uncertainties added in quadrature. The bottom insets show the ratio of the MC to the data. The values of the ratio histograms refer to the bin centroids.
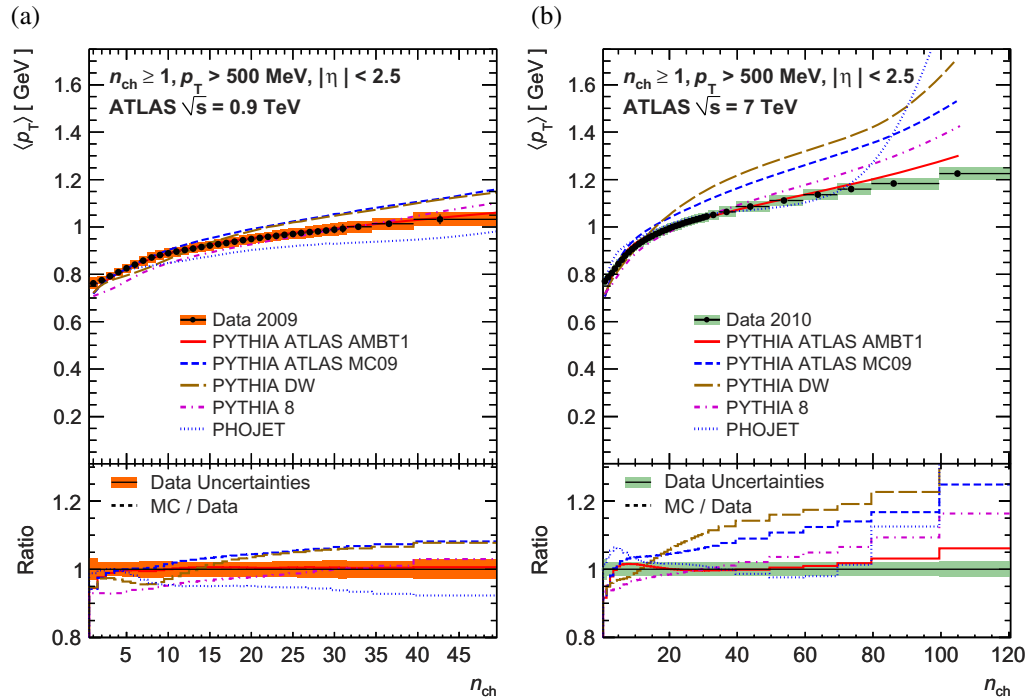
charged multiplicity at $\sqrt{s} = 2.36$ TeV is not shown because different track reconstruction methods are used for determining the p_T and multiplicity distributions, as discussed in section 4.3.2. Figure 11 shows the results for events with $n_{ch} \geqslant 1$, $p_T > 500$ MeV and $|\eta| < 2.5$. At 900 GeV the slope versus n_{ch} for high values of n_{ch} seems to be well described by most models but the absolute value is best modelled by PYTHIA6 DW. At the highest centre-of-mass energy above 20 particles the models vary widely both in slope and in absolute value; at low values of n_{ch} none of the models describe the data very well. In the more inclusive phase-space region, figures 12(a) and (b), the models vary widely, especially at high $\sqrt{s}$.

9.5. $dn_{ch} / d\eta$ at $\eta = 0$

The mean number of charged particles in the central region is computed by averaging over $|\eta| < 0.2$. The values for all three phase-space regions and all energies available are shown in figure 13 and in table 6. The result quoted at $\sqrt{s} = 2.36$ TeV is the value obtained using the Pixel track method. The phase-space region with the largest minimum p_T and the highest minimum multiplicity ($p_T > 500$ MeV; $n_{ch} \geqslant 6$), which is the region with the least amount of diffraction, is the one where the models vary the least and the energy extrapolations of most models agree best with the data. However, in this region the energy extrapolations of PYTHIA6
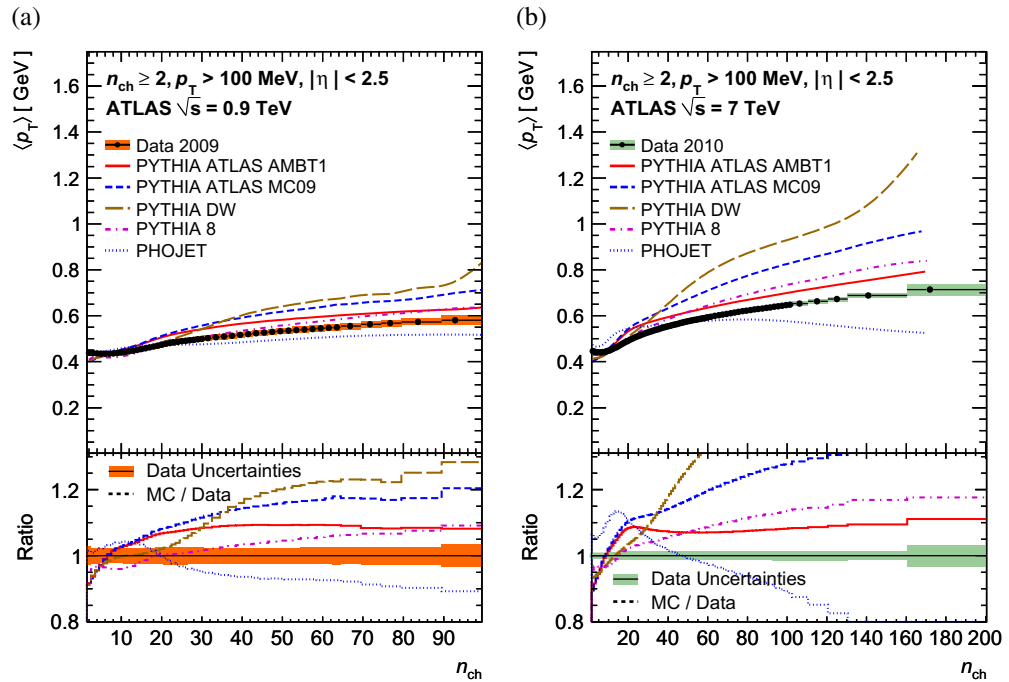
Figure 12. Average transverse momentum as a function of the number of charged particles in the event for events with $n_{ch} \geqslant 2$, $p_T > 100$ MeV and $|\eta| < 2.5$ at $\sqrt{s} = 0.9$ TeV (a) and $\sqrt{s} = 7$ TeV (b). The dots represent the data and the curves the predictions from different MC models. The vertical bars represent the statistical uncertainties, while the shaded areas show statistical and systematic uncertainties added in quadrature. The bottom insets show the ratio of the MC to the data. The values of the ratio histograms refer to the bin centroids.

and PHOJET do not agree with the data. For the most inclusive measurements, none of the models agree with the data and the spread at 7 TeV in the expected values is almost one third of the mean predicted value. The observed value is significantly higher at this energy than any of the models.

9.6. Extrapolation to $p_T = 0$

The mean multiplicities of charged particles with $p_T > 100$ MeV within the full $|\eta| < 2.5$ region are computed as the mean of the distributions shown in figures 6(a) and (b). They are found to be 3.614 ± 0.006 (stat) ± 0.170 (syst) at $\sqrt{s} = 0.9$ TeV and 5.881 ± 0.002 (stat) ± 0.276 (syst) at $\sqrt{s} = 7$ TeV. Multiplying these numbers by the model-dependent scale factors obtained in section 7.6, the averaged inclusive charged-particle multiplicity for events with two or more particles is found to be 3.849 ± 0.006 (stat) ± 0.185 (syst) at $\sqrt{s} = 0.9$ TeV and 6.252 ± 0.002 (stat) ± 0.304 (syst) at $\sqrt{s} = 7$ TeV. This result is interpreted as the average total inelastic multiplicity for events with two or more particles within $|\eta| < 2.5$. Figure 14 compares these results to recently published ALICE results [5, 6] for inclusive inelastic as well as inelastic with more than one particle. The ALICE results are quoted as averages over $|\eta| < 1.0$ and $|\eta| < 0.5$, respectively.
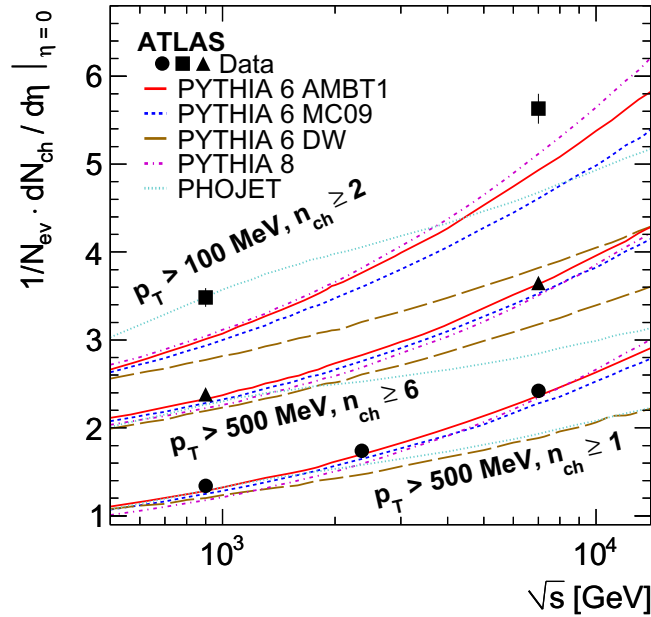
Figure 13. The average charged-particle multiplicity per unit of rapidity for $\eta = 0$ as a function of the centre-of-mass energy. The results with $n_{ch} \geqslant 2$ within the kinematic range $p_T > 100\,\text{MeV}$ and $|\eta| < 2.5$ are shown alongside the results with $n_{ch} \geqslant 1$ within the kinematic range $p_T > 500\,\text{MeV}$ and $|\eta| < 2.5$ at 0.9, 2.36 and 7 TeV. The data are compared to various particle-level MC predictions. The vertical error bars on the data represent the total uncertainty.

Table 6. $dn_{ch}d\eta$ at $\eta = 0$ for the three different phase-space regions considered in this paper for the energies where results are available. For MC, sufficient statistics were generated such that the statistical uncertainty is smaller than the last digit quoted.

Phase-space region	Energy (TeV)	$dn_{ch} / d\eta$ at $\eta = 0$	
		Measured	PYTHIA6 AMBT1 MC
$n_{ch} \geqslant 2$, $p_T > 100\,\text{MeV}$	0.9	3.483 ± 0.009 (stat) ± 0.106 (syst)	3.01
	7	5.630 ± 0.003 (stat) ± 0.169 (syst)	4.93
$n_{ch} \geqslant 1$, $p_T > 500\,\text{MeV}$	0.9	1.343 ± 0.004 (stat) ± 0.027 (syst)	1.28
	2.36	1.74 ± 0.019 (stat) ± 0.058 (syst)	1.70
	7	2.423 ± 0.001 (stat) ± 0.050 (syst)	2.36
$n_{ch} \geqslant 6$, $p_T > 500\,\text{MeV}$	0.9	2.380 ± 0.009 (stat) ± 0.027 (syst)	2.33
	7	3.647 ± 0.002 (stat) ± 0.052 (syst)	3.63

10. Conclusions

Charged-particle multiplicity measurements made with the ATLAS detector using the first collisions delivered by the LHC during 2009 and 2010 are presented. Based on over 300 000 proton–proton inelastic interactions at 900 GeV, just under 6000 at 2.36 TeV and over 10 million
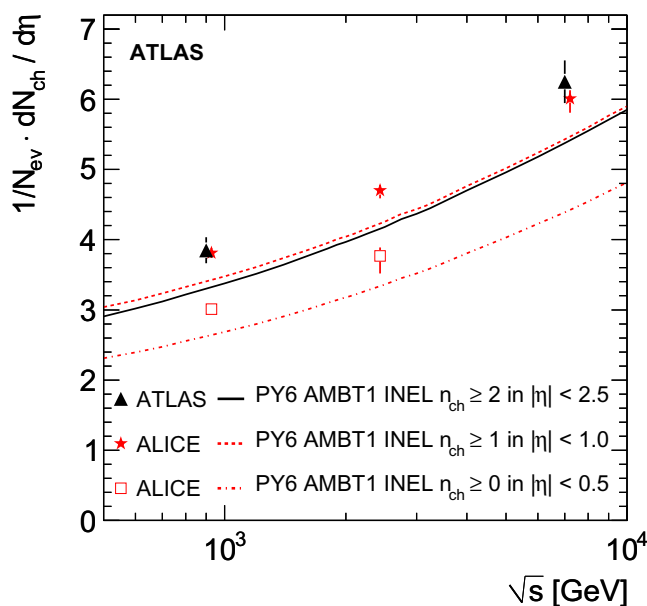
Figure 14. The average charged-particle multiplicity per unit of rapidity as a function of the centre-of-mass energy. The ATLAS results are for $n_{ch} \geqslant 2$ in the region $|\eta| < 2.5$. For comparison, ALICE results for $n_{ch} \geqslant 1$ in the region $|\eta| < 1.0$ and $n_{ch} \geqslant 0$ in the region $|\eta| < 0.5$ are shown. It should be noted that the ALICE points have been slightly shifted horizontally for clarity. The data points are compared to PYTHIA6 AMBT1 predictions for the same phase-space regions.

at 7 TeV, the properties of events in three well-defined phase-space regions were studied. The data were corrected with minimal model dependence to obtain inclusive distributions. The selected kinematic range and the precision of this analysis highlight clear differences between MC models and the measured distributions. In all the kinematic regions considered, the particle multiplicities are higher than predicted by the MC models.

The three different phase-space regions studied, from the most inclusive to the one with the smallest diffractive contribution, highlight various aspects of the charged-particle spectra. In general, the agreement between the models and the data is better in the phase-space regions with higher minimum p_T cut-off, where diffractive contributions are less significant.

For the $\sqrt{s} = 0.9$ TeV measurements with the p_T threshold of 500 MeV, these results supersede the results presented in [1].

Acknowledgments

IOP Institute of Physics **Φ** DEUTSCHE PHYSIKALISCHE GESELLSCHAFT

Table A.1. ATLAS observables and ranges of distributions used in the AMBT1 tuning.

Analysis	Observable	Tuning range
ATLAS 0.9 TeV, minimum bias, $n_{ch} \geqslant 6$	$\frac{1}{N_{ev}} \cdot \frac{dN_{ch}}{d\eta}$	$-2.5 < \eta < 2.5$
ATLAS 0.9 TeV, minimum bias, $n_{ch} \geqslant 6$	$\frac{1}{N_{ev}} \cdot \frac{1}{2\pi p_T} \cdot \frac{d^2 N_{ch}}{d\eta dp_T}$	$p_T \geqslant 5.0$ GeV
ATLAS 0.9 TeV, minimum bias, $n_{ch} \geqslant 6$	$\frac{1}{N_{ev}} \cdot \frac{dN_{ev}}{dn_{ch}}$	$n_{ch} \geqslant 20$
ATLAS 0.9 TeV, minimum bias, $n_{ch} \geqslant 6$	$\langle p_T \rangle$ versus n_{ch}	$n_{ch} \geqslant 10$
ATLAS 0.9 TeV, UE in minimum bias	$\langle \frac{d^2 N_{ch}}{d\eta d\phi} \rangle$ versus p_T^{lead} (towards)	$p_T^{lead} \geqslant 5.5$ GeV
ATLAS 0.9 TeV, UE in minimum bias	$\langle \frac{d^2 N_{ch}}{d\eta d\phi} \rangle$ versus p_T^{lead} (transverse)	$p_T^{lead} \geqslant 5.5$ GeV
ATLAS 0.9 TeV, UE in minimum bias	$\langle \frac{d^2 N_{ch}}{d\eta d\phi} \rangle$ versus p_T^{lead} (away)	$p_T^{lead} \geqslant 5.5$ GeV
ATLAS 0.9 TeV, UE in minimum bias	$\langle \frac{d^2 \sum p_T}{d\eta d\phi} \rangle$ versus p_T^{lead} (towards)	$p_T^{lead} \geqslant 5.5$ GeV
ATLAS 0.9 TeV, UE in minimum bias	$\langle \frac{d^2 \sum p_T}{d\eta d\phi} \rangle$ versus p_T^{lead} (transverse)	$p_T^{lead} \geqslant 5.5$ GeV
ATLAS 0.9 TeV, UE in minimum bias	$\langle \frac{d^2 \sum p_T}{d\eta d\phi} \rangle$ versus p_T^{lead} (away)	$p_T^{lead} \geqslant 5.5$ GeV
ATLAS 7 TeV, minimum bias, $n_{ch} \geqslant 6$	$\frac{1}{N_{ev}} \cdot \frac{dN_{ch}}{d\eta}$	$-2.5 < \eta < 2.5$
ATLAS 7 TeV, minimum bias, $n_{ch} \geqslant 6$	$\frac{1}{N_{ev}} \cdot \frac{1}{2\pi p_T} \cdot \frac{d^2 N_{ch}}{d\eta dp_T}$	$p_T \geqslant 5.0$ GeV
ATLAS 7 TeV, minimum bias, $n_{ch} \geqslant 6$	$\frac{1}{N_{ev}} \cdot \frac{dN_{ev}}{dn_{ch}}$	$n_{ch} \geqslant 40$
ATLAS 7 TeV, minimum bias, $n_{ch} \geqslant 6$	$\langle p_T \rangle$ versus n_{ch}	$n_{ch} \geqslant 10$
ATLAS 7 TeV, UE in minimum bias	$\langle \frac{d^2 N_{ch}}{d\eta d\phi} \rangle$ versus p_T^{lead} (towards)	$p_T^{lead} \geqslant 10$ GeV
ATLAS 7 TeV, UE in minimum bias	$\langle \frac{d^2 N_{ch}}{d\eta d\phi} \rangle$ versus p_T^{lead} (transverse)	$p_T^{lead} \geqslant 10$ GeV
ATLAS 7 TeV, UE in minimum bias	$\langle \frac{d^2 N_{ch}}{d\eta d\phi} \rangle$ versus p_T^{lead} (away)	$p_T^{lead} \geqslant 10$ GeV
ATLAS 7 TeV, UE in minimum bias	$\langle \frac{d^2 \sum p_T}{d\eta d\phi} \rangle$ versus p_T^{lead} (towards)	$p_T^{lead} \geqslant 10$ GeV
ATLAS 7 TeV, UE in minimum bias	$\langle \frac{d^2 \sum p_T}{d\eta d\phi} \rangle$ versus p_T^{lead} (transverse)	$p_T^{lead} \geqslant 10$ GeV
ATLAS 7 TeV, UE in minimum bias	$\langle \frac{d^2 \sum p_T}{d\eta d\phi} \rangle$ versus p_T^{lead} (away)	$p_T^{lead} \geqslant 10$ GeV

Table A.2. Tevatron datasets used in the AMBT1 tuning. No specific cuts on the tuning ranges were made.

Observables

CDF Run I UE in dijet events [49] (leading jet analysis)
  N_{ch} density versus leading jet p_T (transverse), JET20
  N_{ch} density versus leading jet p_T (towards), JET20
  N_{ch} density versus leading jet p_T (away), JET20
  $\sum p_T$ density versus leading jet p_T (transverse), JET20
  $\sum p_T$ density versus leading jet p_T (towards), JET20
  $\sum p_T$ density versus leading jet p_T (away), JET20
  N_{ch} density versus leading jet p_T (transverse), min bias
  N_{ch} density versus leading jet p_T (towards), min bias
  N_{ch} density versus leading jet p_T (away), min bias
  $\sum p_T$ density versus leading jet p_T (transverse), min bias
  $\sum p_T$ density versus leading jet p_T (towards), min bias
  $\sum p_T$ density versus leading jet p_T (away), min bias
  p_T distribution (transverse), leading $p_T > 5$ GeV
  p_T distribution (transverse), leading $p_T > 30$ GeV

CDF Run I UE in MIN/MAX-cones [50] ('MIN-MAX' analysis)
  $\langle p_T^{max} \rangle$ versus E_T^{lead}, $\sqrt{s} = 1800$ GeV
  $\langle p_T^{min} \rangle$ versus E_T^{lead}, $\sqrt{s} = 1800$ GeV
  $\langle p_T^{diff} \rangle$ versus E_T^{lead}, $\sqrt{s} = 1800$ GeV
  $\langle N_{max} \rangle$ versus E_T^{lead}, $\sqrt{s} = 1800$ GeV
  $\langle N_{min} \rangle$ versus E_T^{lead}, $\sqrt{s} = 1800$ GeV
  Swiss Cheese p_T^{sum} versus E_T^{lead} (2 jets), $\sqrt{s} = 1800$ GeV
  $\langle p_T^{max} \rangle$ versus E_T^{lead}, $\sqrt{s} = 630$ GeV
  $\langle p_T^{min} \rangle$ versus E_T^{lead}, $\sqrt{s} = 630$ GeV
  $\langle p_T^{diff} \rangle$ versus E_T^{lead}, $\sqrt{s} = 630$ GeV
  Swiss Cheese p_T^{sum} versus E_T^{lead} (2 jets), $\sqrt{s} = 630$ GeV

D0 Run II dijet angular correlations [51]
  Dijet azimuthal angle, $p_T^{max} \in [75, 100]$ GeV
  Dijet azimuthal angle, $p_T^{max} \in [100, 130]$ GeV
  Dijet azimuthal angle, $p_T^{max} \in [130, 180]$ GeV
  Dijet azimuthal angle, $p_T^{max} > 180$ GeV

CDF Run II minimum bias [52]
  $\langle p_T \rangle$ of charged particles versus N_{ch}, $\sqrt{s} = 1960$ GeV

CDF Run I Z p_T [53]
  $\frac{d\sigma}{dp_T^Z}$, $\sqrt{s} = 1800$ GeV

Table B.1. Number of events and tracks in the two additional phase-space regions and energies considered in this appendix.

Phase-space region		$\sqrt{s} = 0.9$ TeV		$\sqrt{s} = 7$ TeV	
n_{ch}	min p_T	Events	Tracks	Events	Tracks
20	100 MeV	69 833	1 966 059	4 029 563	153 553 344
1	2.5 GeV	19 016	22 233	1 715 637	2 690 534

Table B.2. $dn_{ch} / d\eta$ at $\eta = 0$ for the additional two different phase-space regions considered in this paper for $\sqrt{s} = 0.9$ TeV and $\sqrt{s} = 7$ TeV.

Phase-space region	Energy (TeV)	$dn_{ch} / d\eta$ at $\eta = 0$ measured
$n_{ch} \geqslant 20$, $p_T > 100$ MeV	0.9	6.596 ± 0.025 (stat) ± 0.080 (syst)
	7	9.077 ± 0.005 (stat) ± 0.157 (syst)
$n_{ch} \geqslant 1$, $p_T > 2.5$ GeV	0.9	0.281 ± 0.006 (stat) ± 0.0005 (syst)
	7	0.362 ± 0.001 (stat) ± 0.002 (syst)

Appendix A. Distributions used in AMBT1 tuning

Tables A.1 and A.2 show the list of all distributions from ATLAS and the Tevatron, respectively, used in the ATLAS Minimum Bias Tune 1 (AMBT1). The 'Analysis' column refers to the event selection used in the particular analysis. The 'Tuning range' column refers to the portion of the phase-space region that is considered for the tune.

Appendix B. Additional phase-space regions

Two additional phase-space regions are considered in this appendix:

- at least 20 charged particles in the kinematic range $|\eta| < 2.5$ and $p_T > 100$ MeV,
- at least one charged particle in the kinematic range $|\eta| < 2.5$ and $p_T > 2.5$ GeV.

The correction procedures as well as methods used to extract the systematic uncertainties are identical to the three phase-space regions presented in the main part of the paper. The first phase-space region is chosen to be compared to the other diffraction-reduced phase-space region with six particles above 500 MeV and allows the study of the interplay between the number of particles and the p_T, in particular for the study of diffraction models. The second additional phase-space region is chosen so as to be less influenced by non-perturbative parts of the ND modelling and to be useful in predicting high-p_T particle rates, for example for trigger studies.

Table B.1 shows the number of selected events and tracks for these two additional phase-space regions at both $\sqrt{s} = 0.9$ TeV and $\sqrt{s} = 7$ TeV. Figures B.1–B.4 show the four kinematic
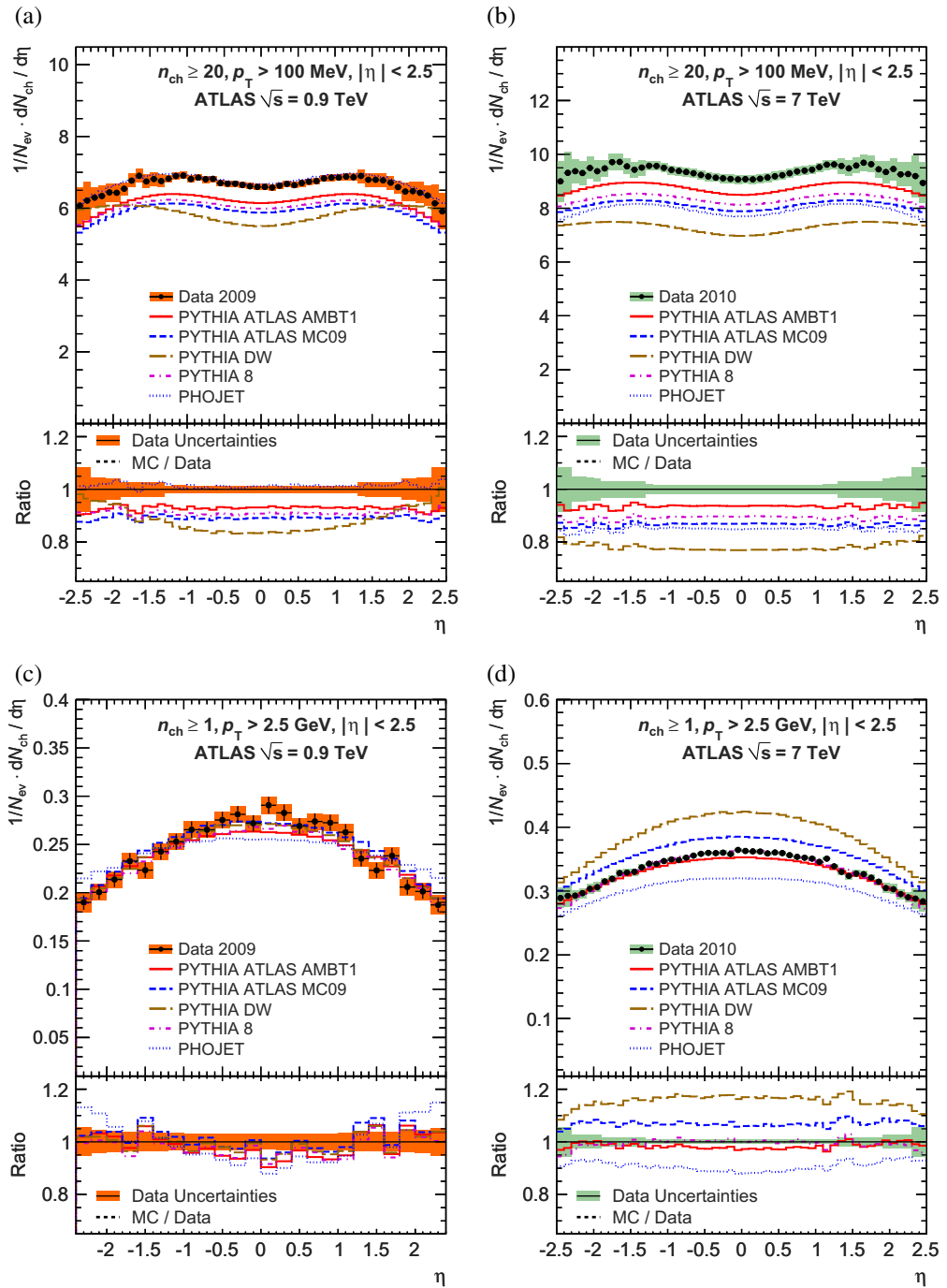
Figure B.1. Charged-particle multiplicities as a function of the pseudorapidity for events with $n_{ch} \geqslant 20$, $p_T > 100$ MeV (a, b) and $n_{ch} \geqslant 1$, $p_T > 2.5$ GeV (c, d) and $|\eta| < 2.5$ at $\sqrt{s} = 0.9$ TeV (a, c) and $\sqrt{s} = 7$ TeV (b, d). The dots represent the data and the curves the predictions from different MC models. The vertical bars represent the statistical uncertainties, while the shaded areas show statistical and systematic uncertainties added in quadrature. The bottom insets show the ratio of the MC to the data. The values of the ratio histograms refer to the bin centroids.
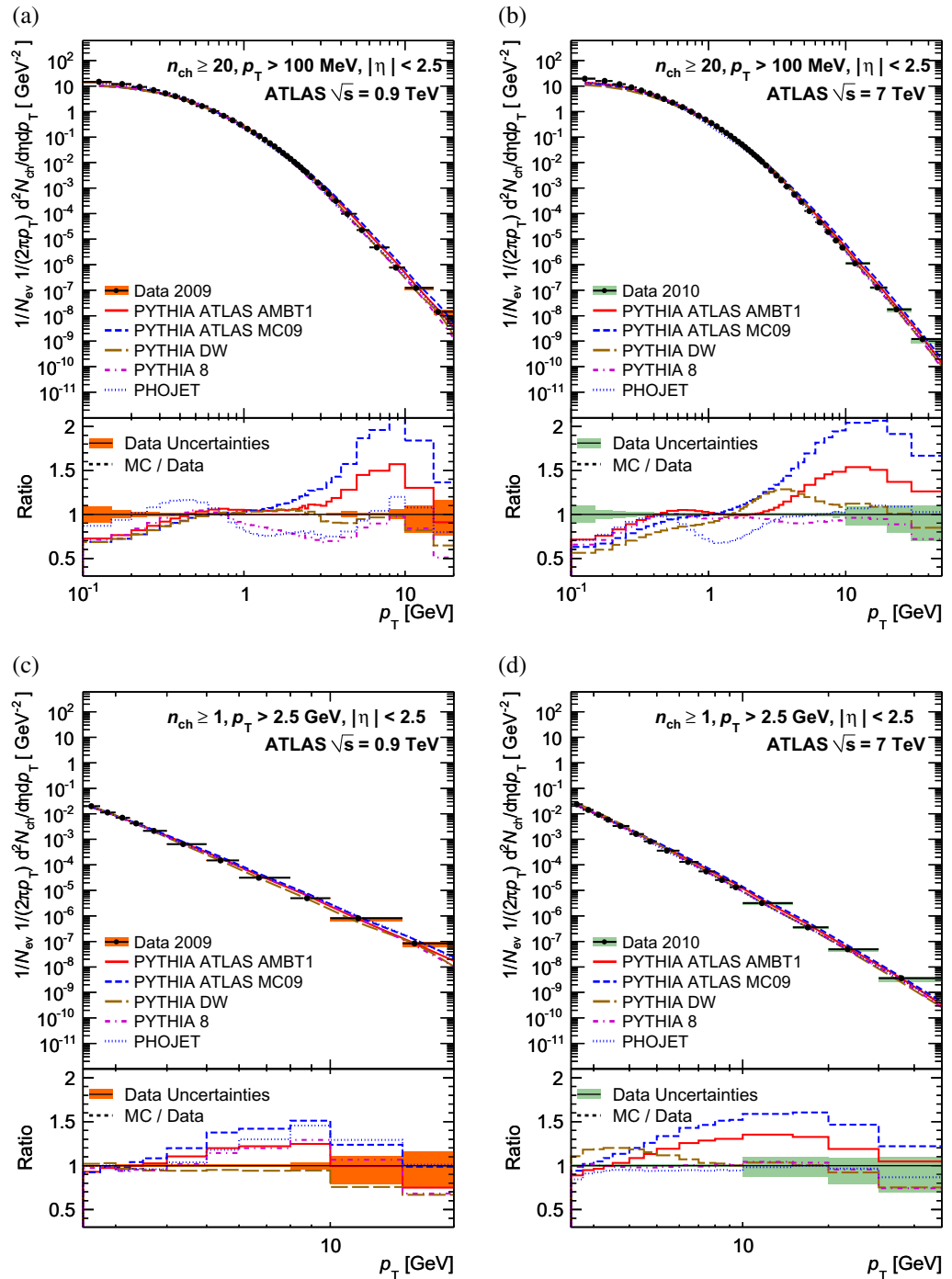
Figure B.2. Charged-particle multiplicities as a function of the transverse momentum for events with $n_{ch} \geqslant 20$, $p_T > 100$ MeV (a, b) and $n_{ch} \geqslant 1$, $p_T > 2.5$ GeV (c, d) and $|\eta| < 2.5$ at $\sqrt{s} = 0.9$ TeV (a, c) and $\sqrt{s} = 7$ TeV (b, d). The dots represent the data and the curves the predictions from different MC models. The vertical bars represent the statistical uncertainties, while the shaded areas show statistical and systematic uncertainties added in quadrature. The bottom insets show the ratio of the MC to the data. The values of the ratio histograms refer to the bin centroids.
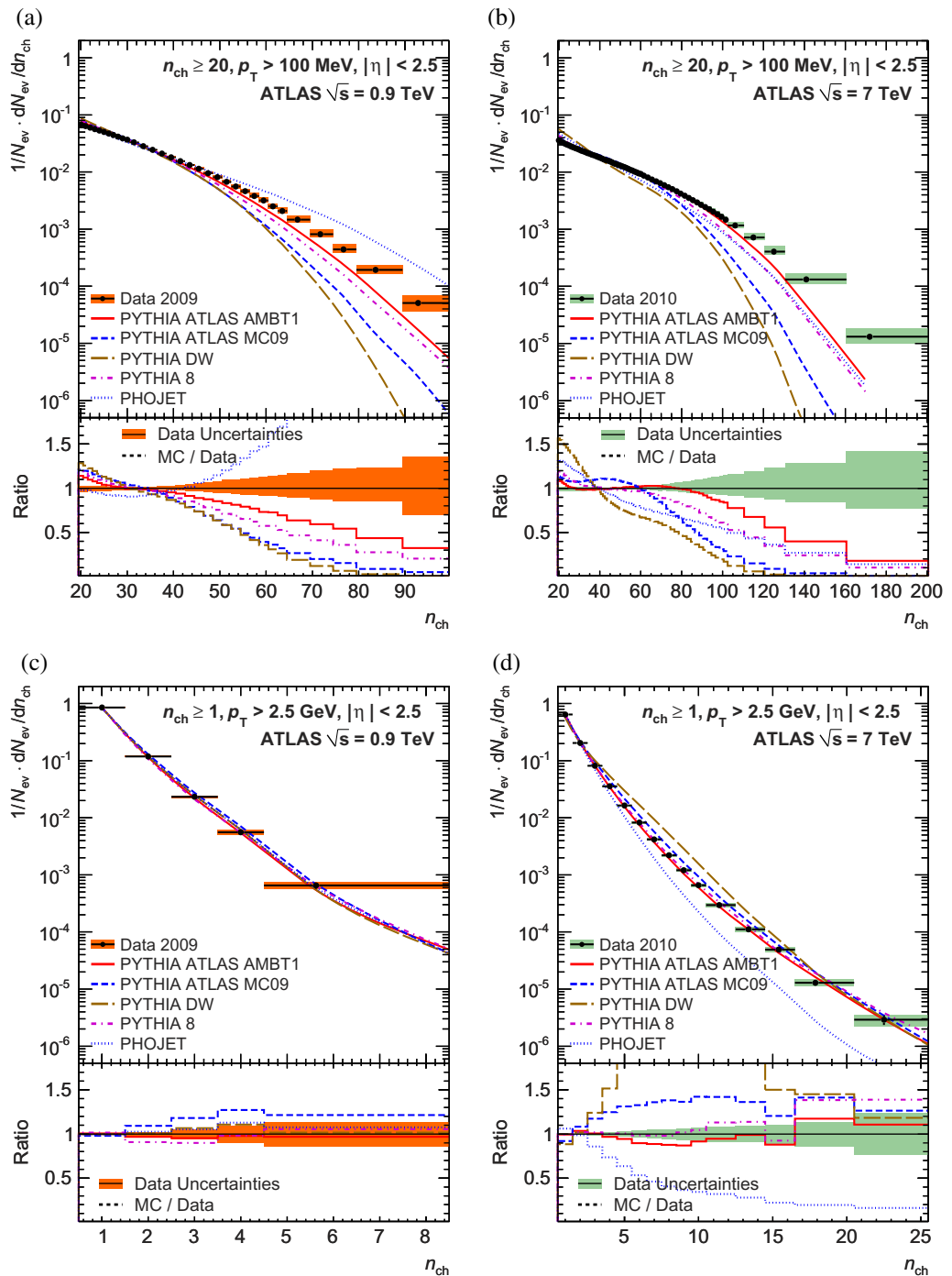
Figure B.3. Charged-particle multiplicity distributions for events with $n_{ch} \geqslant 20$, $p_T > 100$ MeV (a, b) and $n_{ch} \geqslant 1$, $p_T > 2.5$ GeV (c, d) and $|\eta| < 2.5$ at $\sqrt{s} = 0.9$ TeV (a, c) and $\sqrt{s} = 7$ TeV (b, d). The dots represent the data and the curves the predictions from different MC models. The vertical bars represent the statistical uncertainties, while the shaded areas show statistical and systematic uncertainties added in quadrature. The bottom insets show the ratio of the MC to the data. The values of the ratio histograms refer to the bin centroids.
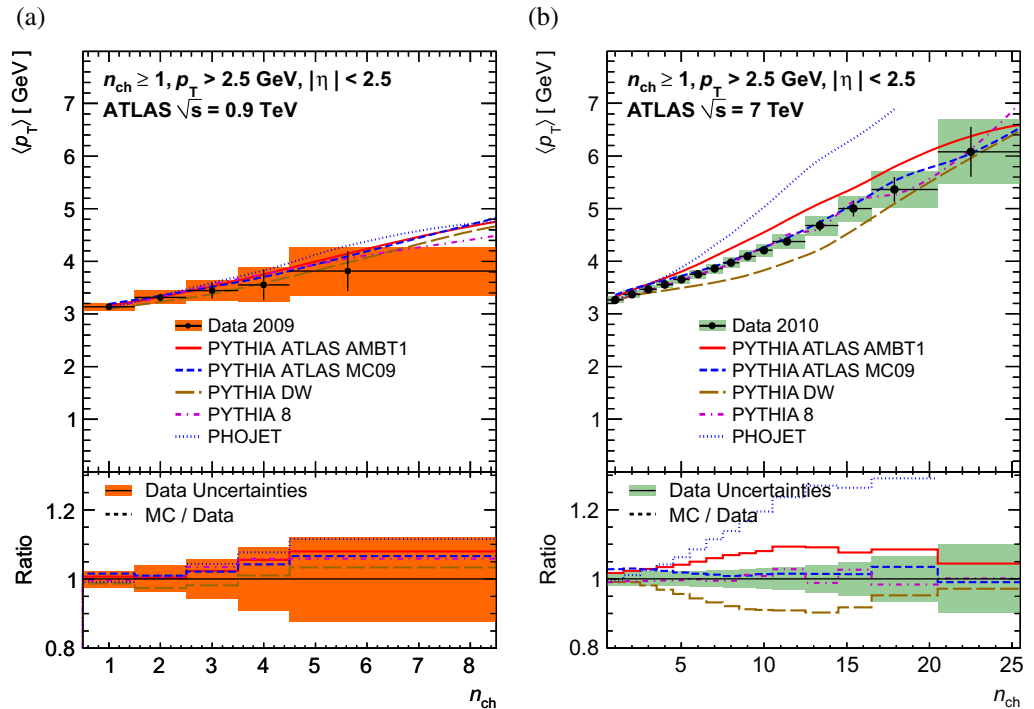
Figure B.4. Average transverse momentum as a function of the number of charged particles in the event for events with $n_{ch} \geqslant 1$, $p_T > 2.5$ GeV and $|\eta| < 2.5$ at $\sqrt{s} = 0.9$ TeV (a) and $\sqrt{s} = 7$ TeV (b). The dots represent the data and the curves the predictions from different MC models. The vertical bars represent the statistical uncertainties, while the shaded areas show statistical and systematic uncertainties added in quadrature. The bottom insets show the ratio of the MC to the data. The values of the ratio histograms refer to the bin centroids.

distributions. Table B.2 shows the results for the mean track multiplicity at central eta (obtained as the average between $-0.2 < \eta < 0.2$). Figure B.5 shows the mean track multiplicity at central rapidity for all centre-of-mass energies and phase-space regions presented in this paper, along with predictions from PYTHIA6 AMBT1.

The ATLAS Collaboration

G Aad[48], B Abbott[111], J Abdallah[11], A A Abdelalim[49], A Abdesselam[118], O Abdinov[10], B Abi[112], M Abolins[88], H Abramowicz[153], H Abreu[115], E Acerbi[89a,89b], B S Acharya[164a,164b], M Ackers[20], D L Adams[24], T N Addy[56], J Adelman[175], M Aderholz[99], S Adomeit[98], P Adragna[75], T Adye[129], S Aefsky[22], J A Aguilar-Saavedra[124b,178], M Aharrouche[81], S P Ahlen[21], F Ahles[48], A Ahmad[148], M Ahsan[40], G Aielli[133a,133b], T Akdogan[18a], T P A Åkesson[79], G Akimoto[155], A V Akimov[94], M S Alam[1], M A Alam[76], S Albrand[55], M Aleksa[29], I N Aleksandrov[65], M Aleppo[89a,89b], F Alessandria[89a], C Alexa[25a], G Alexander[153], G Alexandre[49], T Alexopoulos[9], M Alhroob[20], M Aliev[15], G Alimonti[89a], J Alison[120], M Aliyev[10], P P Allport[73], S E Allwood-Spiers[53], J Almond[82], A Aloisio[102a,102b], R Alon[171], A Alonso[79], J Alonso[14], M G Alviggi[102a,102b], K Amako[66], P Amaral[29], C Amelung[22], V V Ammosov[128], A Amorim[124a,179], G Amorós[167], N Amram[153], C Anastopoulos[139], T Andeen[34], C F Anders[20], K J Anderson[30], A Andreazza[89a,89b],
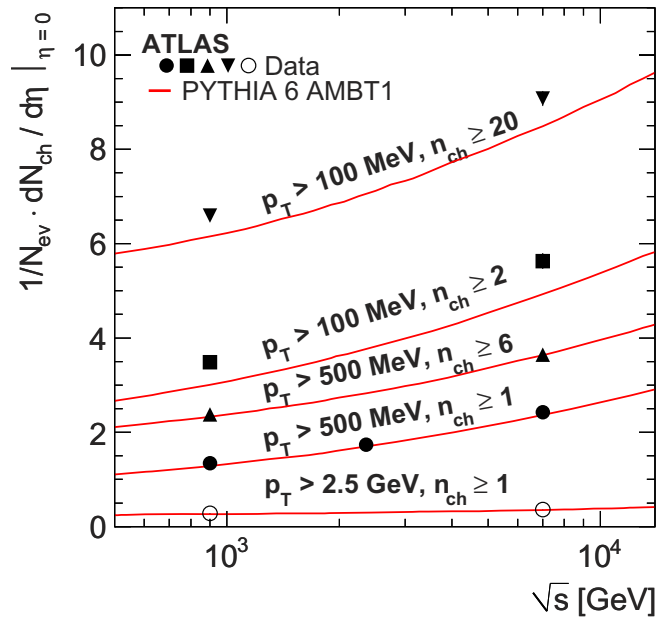
Figure B.5. The average charged-particle multiplicity per unit of rapidity for $\eta = 0$ as a function of the centre-of-mass energy. All the measured phase-space regions and energies are shown as triangles and compared to predictions from PYTHIA6 AMBT1 tune. The phase-space region label is above the corresponding curves and points. Combined statistical and systematic uncertainties are approximately equal to or smaller than the data points.

V Andrei[58a], M-L Andrieux[55], X S Anduaga[70], A Angerami[34], F Anghinolfi[29], N Anjos[124a], A Annovi[47], A Antonaki[8], M Antonelli[47], S Antonelli[19a,19b], J Antos[144b], F Anulli[132a], S Aoun[83], L Aperio Bella[4], R Apolle[118], G Arabidze[88], I Aracena[143], Y Arai[66], A T H Arce[44], J P Archambault[28], S Arfaoui[29,180], J-F Arguin[14], E Arik[18a,208], M Arik[18a], A J Armbruster[87], K E Arms[109], S R Armstrong[24], O Arnaez[81], C Arnault[115], A Artamonov[95], G Artoni[132a,132b], D Arutinov[20], S Asai[155], R Asfandiyarov[172], S Ask[27], B Åsman[146a,146b], L Asquith[5], K Assamagan[24], A Astbury[169], A Astvatsatourov[52], G Atoian[175], B Aubert[4], B Auerbach[175], E Auge[115], K Augsten[127], M Aurousseau[4], N Austin[73], R Avramidou[9], D Axen[168], C Ay[54], G Azuelos[93,181], Y Azuma[155], M A Baak[29], G Baccaglioni[89a], C Bacci[134a,134b], A M Bach[14], H Bachacou[136], K Bachas[29], G Bachy[29], M Backes[49], E Badescu[25a], P Bagnaia[132a,132b], S Bahinipati[2], Y Bai[32a], D C Bailey[158], T Bain[158], J T Baines[129], O K Baker[175], S Baker[77], F Baltasar Dos Santos Pedrosa[29], E Banas[38], P Banerjee[93], Sw Banerjee[169], D Banfi[89a,89b], A Bangert[137], V Bansal[169], H S Bansil[17], L Barak[171], S P Baranov[94], A Barashkou[65], A Barbaro Galtieri[14], T Barber[27], E L Barberio[86], D Barberis[50a,50b], M Barbero[20], D Y Bardin[65], T Barillari[99], M Barisonzi[174], T Barklow[143], N Barlow[27], B M Barnett[129], R M Barnett[14], A Baroncelli[134a], A J Barr[118], F Barreiro[80], J Barreiro Guimarães da Costa[57], P Barrillon[115], R Bartoldus[143], A E Barton[71], D Bartsch[20], R L Bates[53], L Batkova[144a], J R Batley[27], A Battaglia[16], M Battistin[29], G Battistoni[89a], F Bauer[136], H S Bawa[143], B Beare[158], T Beau[78], P H Beauchemin[118], R Beccherle[50a], P Bechtle[41], H P Beck[16], M Beckingham[48], K H Becks[174], A J Beddall[18c], A Beddall[18c], V A Bednyakov[65], C Bee[83], M Begel[24], S Behar Harpaz[152], P K Behera[63], M Beimforde[99], C Belanger-Champagne[166], P J Bell[49], W H Bell[49], G Bella[153],

L Bellagamba[19a], F Bellina[29], G Bellomo[89a,89b], M Bellomo[119a], A Belloni[57], K Belotskiy[96], O Beltramello[29], S Ben Ami[152], O Benary[153], D Benchekroun[135a], C Benchouk[83], M Bendel[81], B H Benedict[163], N Benekos[165], Y Benhammou[153], D P Benjamin[44], M Benoit[115], J R Bensinger[22], K Benslama[130], S Bentvelsen[105], D Berge[29], E Bergeaas Kuutmann[41], N Berger[4], F Berghaus[169], E Berglund[49], J Beringer[14], K Bernardet[83], P Bernat[115], R Bernhard[48], C Bernius[24], T Berry[76], A Bertin[19a,19b], F Bertinelli[29], F Bertolucci[122a,122b], M I Besana[89a,89b], N Besson[136], S Bethke[99], W Bhimji[45], R M Bianchi[29], M Bianco[72a,72b], O Biebel[98], J Biesiada[14], M Biglietti[132a,132b], H Bilokon[47], M Bindi[19a,19b], A Bingul[18c], C Bini[132a,132b], C Biscarat[177], U Bitenc[48], K M Black[21], R E Blair[5], J-B Blanchard[115], G Blanchot[29], C Blocker[22], J Blocki[38], A Blondel[49], W Blum[81], U Blumenschein[54], G J Bobbink[105], V B Bobrovnikov[107], A Bocci[44], R Bock[29], C R Boddy[118], M Boehler[41], J Boek[174], N Boelaert[35], S Böser[77], J A Bogaerts[29], A Bogdanchikov[107], A Bogouch[90,208], C Bohm[146a], V Boisvert[76], T Bold[163,182], V Boldea[25a], M Bona[75], M Boonekamp[136], G Boorman[76], C N Booth[139], P Booth[139], J R A Booth[17], S Bordoni[78], C Borer[16], A Borisov[128], G Borissov[71], I Borjanovic[12a], S Borroni[132a,132b], K Bos[105], D Boscherini[19a], M Bosman[11], H Boterenbrood[105], D Botterill[129], J Bouchami[93], J Boudreau[123], E V Bouhova-Thacker[71], C Boulahouache[123], C Bourdarios[115], N Bousson[83], A Boveia[30], J Boyd[29], I R Boyko[65], N I Bozhko[128], I Bozovic-Jelisavcic[12b], J Bracinik[17], A Braem[29], E Brambilla[72a,72b], P Branchini[134a], G W Brandenburg[57], A Brandt[7], G Brandt[41], O Brandt[54], U Bratzler[156], B Brau[84], J E Brau[114], H M Braun[174], B Brelier[158], J Bremer[29], R Brenner[166], S Bressler[152], D Breton[115], N D Brett[118], P G Bright-Thomas[17], D Britton[53], F M Brochu[27], I Brock[20], R Brock[88], T J Brodbeck[71], E Brodet[153], F Broggi[89a], C Bromberg[88], G Brooijmans[34], W K Brooks[31b], G Brown[82], E Brubaker[30], P A Bruckman de Renstrom[38], D Bruncko[144b], R Bruneliere[48], S Brunet[61], A Bruni[19a], G Bruni[19a], M Bruschi[19a], T Buanes[13], F Bucci[49], J Buchanan[118], N J Buchanan[2], P Buchholz[141], R M Buckingham[118], A G Buckley[45], S I Buda[25a], I A Budagov[65], B Budick[108], V Büscher[81], L Bugge[117], D Buira-Clark[118], E J Buis[105], O Bulekov[96], M Bunse[42], T Buran[117], H Burckhart[29], S Burdin[73], T Burgess[13], S Burke[129], E Busato[33], P Bussey[53], C P Buszello[166], F Butin[29], B Butler[143], J M Butler[21], C M Buttar[53], J M Butterworth[77], W Buttinger[27], T Byatt[77], S Cabrera Urbán[167], M Caccia[89a,89b], D Caforio[19a,19b], O Cakir[3a], P Calafiura[14], G Calderini[78], P Calfayan[98], R Calkins[106], L P Caloba[23a], R Caloi[132a,132b], D Calvet[33], S Calvet[33], A Camard[78], P Camarri[133a,133b], M Cambiaghi[119a,119b], D Cameron[117], J Cammin[20], S Campana[29], M Campanelli[77], V Canale[102a,102b], F Canelli[30], A Canepa[159a], J Cantero[80], L Capasso[102a,102b], M D M Capeans Garrido[29], I Caprini[25a], M Caprini[25a], D Capriotti[99], M Capua[36a,36b], R Caputo[148], C Caramarcu[25a], R Cardarelli[133a], T Carli[29], G Carlino[102a], L Carminati[89a,89b], B Caron[159a], S Caron[48], C Carpentieri[48], G D Carrillo Montoya[172], S Carron Montero[158], A A Carter[75], J R Carter[27], J Carvalho[124a,183], D Casadei[108], M P Casado[11], M Cascella[122a,122b], C Caso[50a,50b,208], A M Castaneda Hernandez[172], E Castaneda-Miranda[172], V Castillo Gimenez[167], N F Castro[124b,178], G Cataldi[72a], F Cataneo[29], A Catinaccio[29], J R Catmore[71], A Cattai[29], G Cattani[133a,133b], S Caughron[88], A Cavallari[132a,132b], P Cavalleri[78], D Cavalli[89a], M Cavalli-Sforza[11], V Cavasinni[122a,122b], A Cazzato[72a,72b], F Ceradini[134a,134b], C Cerna[83], A S Cerqueira[23a], A Cerri[29], L Cerrito[75], F Cerutti[47], S A Cetin[18b], F Cevenini[102a,102b], A Chafaq[135a], D Chakraborty[106], K Chan[2], B Chapleau[85], J D Chapman[27], J W Chapman[87], E Chareyre[78], D G Charlton[17], V Chavda[82], S Cheatham[71], S Chekanov[5], S V Chekulaev[159a], G A Chelkov[65], H Chen[24], L Chen[2], S Chen[32c], T Chen[32c], X Chen[172], S Cheng[32a], A Cheplakov[65], V F Chepurnov[65], R Cherkaoui El Moursli[135d], V Chernyatin[24], E Cheu[6], S L Cheung[158], L Chevalier[136], F Chevallier[136], G Chiefari[102a,102b], L Chikovani[51], J T Childers[58a], A Chilingarov[71], G Chiodini[72a], M V Chizhov[65], G Choudalakis[30], S

Chouridou[137], I A Christidi[77], A Christov[48], D Chromek-Burckhart[29], M L Chu[151], J Chudoba[125], G Ciapetti[132a,132b], A K Ciftci[3a], R Ciftci[3a], D Cinca[33], V Cindro[74], M D Ciobotaru[163], C Ciocca[19a,19b], A Ciocio[14], M Cirilli[87], M Ciubancan[25a], A Clark[49], P J Clark[45], W Cleland[123], J C Clemens[83], B Clement[55], C Clement[146a,146b], R W Clifft[129], Y Coadou[83], M Cobal[164a,164c], A Coccaro[50a,50b], J Cochran[64], P Coe[118], J G Cogan[143], J Coggeshall[165], E Cogneras[177], C D Cojocaru[28], J Colas[4], A P Colijn[105], C Collard[115], N J Collins[17], C Collins-Tooth[53], J Collot[55], G Colon[84], R Coluccia[72a,72b], G Comune[88], P Conde Muiño[124a], E Coniavitis[118], M C Conidi[11], M Consonni[104], S Constantinescu[25a], C Conta[119a,119b], F Conventi[102a,184], J Cook[29], M Cooke[14], B D Cooper[75], A M Cooper-Sarkar[118], N J Cooper-Smith[76], K Copic[34], T Cornelissen[50a,50b], M Corradi[19a], S Correard[83], F Corriveau[85,185], A Cortes-Gonzalez[165], G Cortiana[99], G Costa[89a], M J Costa[167], D Costanzo[139], T Costin[30], D Côté[29], R Coura Torres[23a], L Courneyea[169], G Cowan[76], C Cowden[27], B E Cox[82], K Cranmer[108], M Cristinziani[20], G Crosetti[36a,36b], R Crupi[72a,72b], S Crépé-Renaudin[55], C Cuenca Almenar[175], T Cuhadar Donszelmann[139], S Cuneo[50a,50b], M Curatolo[47], C J Curtis[17], P Cwetanski[61], H Czirr[141], Z Czyczula[117], S D'Auria[53], M D'Onofrio[73], A D'Orazio[132a,132b], A Da Rocha Gesualdi Mello[23a], P V M Da Silva[23a], C Da Via[82], W Dabrowski[37], A Dahlhoff[48], T Dai[87], C Dallapiccola[84], S J Dallison[129,208], M Dam[35], M Dameri[50a,50b], D S Damiani[137], H O Danielsson[29], R Dankers[105], D Dannheim[99], V Dao[49], G Darbo[50a], G L Darlea[25b], C Daum[105], J P Dauvergne[29], W Davey[86], T Davidek[126], N Davidson[86], R Davidson[71], M Davies[93], A R Davison[77], E Dawe[142], I Dawson[139], J W Dawson[5,208], R K Daya[39], K De[7], R de Asmundis[102a], S De Castro[19a,19b], S De Cecco[78], J de Graat[98], N De Groot[104], P de Jong[105], E De La Cruz-Burelo[87], C De La Taille[115], B De Lotto[164a,164c], L De Mora[71], L De Nooij[105], M De Oliveira Branco[29], D De Pedis[132a], P de Saintignon[55], A De Salvo[132a], U De Sanctis[164a,164c], A De Santo[149], J B De Vivie De Regie[115], S Dean[77], G Dedes[99], D V Dedovich[65], J Degenhardt[120], M Dehchar[118], M Deile[98], C Del Papa[164a,164c], J Del Peso[80], T Del Prete[122a,122b], A Dell'Acqua[29], L Dell'Asta[89a,89b], M Della Pietra[102a,184], D della Volpe[102a,102b], M Delmastro[29], P Delpierre[83], N Delruelle[29], P A Delsart[55], C Deluca[148], S Demers[175], M Demichev[65], B Demirkoz[11], J Deng[163], S P Denisov[128], C Dennis[118], D Derendarz[38], J E Derkaoui[135c], F Derue[78], P Dervan[73], K Desch[20], E Devetak[148], P O Deviveiros[158], A Dewhurst[129], B DeWilde[148], S Dhaliwal[158], R Dhullipudi[24,186], A Di Ciaccio[133a,133b], L Di Ciaccio[4], A Di Girolamo[29], B Di Girolamo[29], S Di Luise[134a,134b], A Di Mattia[88], R Di Nardo[133a,133b], A Di Simone[133a,133b], R Di Sipio[19a,19b], M A Diaz[31a], F Diblen[18c], E B Diehl[87], H Dietl[99], J Dietrich[48], T A Dietzsch[58a], S Diglio[115], K Dindar Yagci[39], J Dingfelder[20], C Dionisi[132a,132b], P Dita[25a], S Dita[25a], F Dittus[29], F Djama[83], R Djilkibaev[108], T Djobava[51], M A B do Vale[23a], A Do Valle Wemans[124a], T K O Doan[4], M Dobbs[85], R Dobinson[29,208], D Dobos[42], E Dobson[29], M Dobson[163], J Dodd[34], O B Dogan[18a,208], C Doglioni[118], T Doherty[53], Y Doi[66,208], J Dolejsi[126], I Dolenc[74], Z Dolezal[126], B A Dolgoshein[96], T Dohmae[155], M Donadelli[23b], M Donega[120], J Donini[55], J Dopke[174], A Doria[102a], A Dos Anjos[172], M Dosil[11], A Dotti[122a,122b], M T Dova[70], J D Dowell[17], A D Doxiadis[105], A T Doyle[53], Z Drasal[126], J Drees[174], N Dressnandt[120], H Drevermann[29], C Driouichi[35], M Dris[9], J G Drohan[77], J Dubbert[99], T Dubbs[137], S Dube[14], E Duchovni[171], G Duckeck[98], A Dudarev[29], F Dudziak[115], M Dührssen[29], I P Duerdoth[82], L Duflot[115], M-A Dufour[85], M Dunford[29], H Duran Yildiz[3b], R Duxfield[139], M Dwuznik[37], F Dydak[29], D Dzahini[55], M Düren[52], J Ebke[98], S Eckert[48], S Eckweiler[81], K Edmonds[81], C A Edwards[76], I Efthymiopoulos[49], W Ehrenfeld[41], T Ehrich[99], T Eifert[29], G Eigen[13], K Einsweiler[14], E Eisenhandler[75], T Ekelof[166], M El Kacimi[4], M Ellert[166], S Elles[4], F Ellinghaus[81], K Ellis[75], N Ellis[29], J Elmsheuser[98], M Elsing[29], R Ely[14], D Emeliyanov[129], R Engelmann[148], A Engl[98], B Epp[62], A Eppig[87], J Erdmann[54], A Ereditato[16], D Eriksson[146a],

J Ernst[1], M Ernst[24], J Ernwein[136], D Errede[165], S Errede[165], E Ertel[81], M Escalier[115], C Escobar[167], X Espinal Curull[11], B Esposito[47], F Etienne[83], A I Etienvre[136], E Etzion[153], D Evangelakou[54], H Evans[61], L Fabbri[19a,19b], C Fabre[29], K Facius[35], R M Fakhrutdinov[128], S Falciano[132a], A C Falou[115], Y Fang[172], M Fanti[89a,89b], A Farbin[7], A Farilla[134a], J Farley[148], T Farooque[158], S M Farrington[118], P Farthouat[29], D Fasching[172], P Fassnacht[29], D Fassouliotis[8], B Fatholahzadeh[158], A Favareto[89a,89b], L Fayard[115], S Fazio[36a,36b], R Febbraro[33], P Federic[144a], O L Fedin[121], I Fedorko[29], W Fedorko[88], M Fehling-Kaschek[48], L Feligioni[83], D Fellmann[5], C U Felzmann[86], C Feng[32d], E J Feng[30], A B Fenyuk[128], J Ferencei[144b], D Ferguson[172], J Ferland[93], B Fernandes[124a,187], W Fernando[109], S Ferrag[53], J Ferrando[118], V Ferrara[41], A Ferrari[166], P Ferrari[105], R Ferrari[119a], A Ferrer[167], M L Ferrer[47], D Ferrere[49], C Ferretti[87], A Ferretto Parodi[50a,50b], M Fiascaris[30], F Fiedler[81], A Filipčič[74], A Filippas[9], F Filthaut[104], M Fincke-Keeler[169], M C N Fiolhais[124a,183], L Fiorini[11], A Firan[39], G Fischer[41], P Fischer[20], M J Fisher[109], S M Fisher[129], J Flammer[29], M Flechl[48], I Fleck[141], J Fleckner[81], P Fleischmann[173], S Fleischmann[20], T Flick[174], L R Flores Castillo[172], M J Flowerdew[99], F Föhlisch[58a], M Fokitis[9], T Fonseca Martin[16], D A Forbush[138], A Formica[136], A Forti[82], D Fortin[159a], J M Foster[82], D Fournier[115], A Foussat[29], A J Fowler[44], K Fowler[137], H Fox[71], P Francavilla[122a,122b], S Franchino[119a,119b], D Francis[29], T Frank[171], M Franklin[57], S Franz[29], M Fraternali[119a,119b], S Fratina[120], S T French[27], R Froeschl[29], D Froidevaux[29], J A Frost[27], C Fukunaga[156], E Fullana Torregrosa[29], J Fuster[167], C Gabaldon[29], O Gabizon[171], T Gadfort[24], S Gadomski[49], G Gagliardi[50a,50b], P Gagnon[61], C Galea[98], E J Gallas[118], M V Gallas[29], V Gallo[16], B J Gallop[129], P Gallus[125], E Galyaev[40], K K Gan[109], Y S Gao[143,188], V A Gapienko[128], A Gaponenko[14], F Garberson[175], M Garcia-Sciveres[14], C García[167], J E García Navarro[49], R W Gardner[30], N Garelli[29], H Garitaonandia[105], V Garonne[29], J Garvey[17], C Gatti[47], G Gaudio[119a], O Gaumer[49], B Gaur[141], L Gauthier[136], I L Gavrilenko[94], C Gay[168], G Gaycken[20], J-C Gayde[29], E N Gazis[9], P Ge[32d], C N P Gee[129], Ch Geich-Gimbel[20], K Gellerstedt[146a,146b], C Gemme[50a], A Gemmell[53], M H Genest[98], S Gentile[132a,132b], F Georgatos[9], S George[76], P Gerlach[174], A Gershon[153], C Geweniger[58a], H Ghazlane[135d], P Ghez[4], N Ghodbane[33], B Giacobbe[19a], S Giagu[132a,132b], V Giakoumopoulou[8], V Giangiobbe[122a,122b], F Gianotti[29], B Gibbard[24], A Gibson[158], S M Gibson[29], G F Gieraltowski[5], L M Gilbert[118], M Gilchriese[14], O Gildemeister[29], V Gilewsky[91], D Gillberg[28], A R Gillman[129], D M Gingrich[2,181], J Ginzburg[153], N Giokaris[8], R Giordano[102a,102b], F M Giorgi[15], P Giovannini[99], P F Giraud[136], D Giugni[89a], P Giusti[19a], B K Gjelsten[117], L K Gladilin[97], C Glasman[80], J Glatzer[48], A Glazov[41], K W Glitza[174], G L Glonti[65], J Godfrey[142], J Godlewski[29], M Goebel[41], T Göpfert[43], C Goeringer[81], C Gössling[42], T Göttfert[99], S Goldfarb[87], D Goldin[39], T Golling[175], N P Gollub[29], S N Golovnia[128], A Gomes[124a,189], L S Gomez Fajardo[41], R Gonçalo[76], L Gonella[20], C Gong[32b], A Gonidec[29], S Gonzalez[172], S González de la Hoz[167], M L Gonzalez Silva[26], S Gonzalez-Sevilla[49], J J Goodson[148], L Goossens[29], P A Gorbounov[95], H A Gordon[24], I Gorelov[103], G Gorfine[174], B Gorini[29], E Gorini[72a,72b], A Gorišek[74], E Gornicki[38], S A Gorokhov[128], B T Gorski[29], V N Goryachev[128], B Gosdzik[41], M Gosselink[105], M I Gostkin[65], M Gouanère[4], I Gough Eschrich[163], M Gouighri[135a], D Goujdami[135a], M P Goulette[49], A G Goussiou[138], C Goy[4], I Grabowska-Bold[163,182], V Grabski[176], P Grafström[29], C Grah[174], K-J Grahn[147], F Grancagnolo[72a], S Grancagnolo[15], V Grassi[148], V Gratchev[121], N Grau[34], H M Gray[34,190], J A Gray[148], E Graziani[134a], O G Grebenyuk[121], D Greenfield[129], T Greenshaw[73], Z D Greenwood[24,186], I M Gregor[41], P Grenier[143], E Griesmayer[46], J Griffiths[138], N Grigalashvili[65], A A Grillo[137], K Grimm[148], S Grinstein[11], P L Y Gris[33], Y V Grishkevich[97], J-F Grivaz[115], J Grognuz[29], M Groh[99], E Gross[171], J Grosse-Knetter[54], J Groth-Jensen[79], M Gruwe[29], K Grybel[141], V J Guarino[5], C Guicheney[33], A Guida[72a,72b], T Guillemin[4], S Guindon[54], H

Guler[85,191], J Gunther[125], B Guo[158], J Guo[34], A Gupta[30], Y Gusakov[65], V N Gushchin[128], A Gutierrez[93], P Gutierrez[111], N Guttman[153], O Gutzwiller[172], C Guyot[136], C Gwenlan[118], C B Gwilliam[73], A Haas[143], S Haas[29], C Haber[14], R Hackenburg[24], H K Hadavand[39], D R Hadley[17], P Haefner[99], F Hahn[29], S Haider[29], Z Hajduk[38], H Hakobyan[176], J Haller[54], K Hamacher[174], A Hamilton[49], S Hamilton[161], H Han[32a], L Han[32b], K Hanagaki[116], M Hance[120], C Handel[81], P Hanke[58a], C J Hansen[166], J R Hansen[35], J B Hansen[35], J D Hansen[35], P H Hansen[35], P Hansson[143], K Hara[160], G A Hare[137], T Harenberg[174], D Harper[87], R D Harrington[21], O M Harris[138], K Harrison[17], J C Hart[129], J Hartert[48], F Hartjes[105], T Haruyama[66], A Harvey[56], S Hasegawa[101], Y Hasegawa[140], S Hassani[136], M Hatch[29], D Hauff[99], S Haug[16], M Hauschild[29], R Hauser[88], M Havranek[125], B M Hawes[118], C M Hawkes[17], R J Hawkings[29], D Hawkins[163], T Hayakawa[67], D Hayden[76], H S Hayward[73], S J Haywood[129], E Hazen[21], M He[32d], S J Head[17], V Hedberg[79], L Heelan[28], S Heim[88], B Heinemann[14], S Heisterkamp[35], L Helary[4], M Heldmann[48], M Heller[115], S Hellman[146a,146b], C Helsens[11], R C W Henderson[71], M Henke[58a], A Henrichs[54], A M Henriques Correia[29], S Henrot-Versille[115], F Henry-Couannier[83], C Hensel[54], T Henß[174], Y Hernández Jiménez[167], R Herrberg[15], A D Hershenhorn[152], G Herten[48], R Hertenberger[98], L Hervas[29], N P Hessey[105], A Hidvegi[146a], E Higón-Rodriguez[167], D Hill[5,208], J C Hill[27], N Hill[5], K H Hiller[41], S Hillert[20], S J Hillier[17], I Hinchliffe[14], E Hines[120], M Hirose[116], F Hirsch[42], D Hirschbuehl[174], J Hobbs[148], N Hod[153], M C Hodgkinson[139], P Hodgson[139], A Hoecker[29], M R Hoeferkamp[103], J Hoffman[39], D Hoffmann[83], M Hohlfeld[81], M Holder[141], A Holmes[118], S O Holmgren[146a], T Holy[127], J L Holzbauer[88], R J Homer[17], Y Homma[67], T Horazdovsky[127], C Horn[143], S Horner[48], K Horton[118], J-Y Hostachy[55], T Hott[99], S Hou[151], M A Houlden[73], A Hoummada[135a], J Howarth[82], D F Howell[118], I Hristova[41], J Hrivnac[115], I Hruska[125], T Hryn'ova[4], P J Hsu[175], S-C Hsu[14], G S Huang[111], Z Hubacek[127], F Hubaut[83], F Huegging[20], T B Huffman[118], E W Hughes[34], G Hughes[71], R E Hughes-Jones[82], M Huhtinen[29], P Hurst[57], M Hurwitz[14], U Husemann[41], N Huseynov[65,192], J Huston[88], J Huth[57], G Iacobucci[102a], G Iakovidis[9], M Ibbotson[82], I Ibragimov[141], R Ichimiya[67], L Iconomidou-Fayard[115], J Idarraga[115], M Idzik[37], P Iengo[4], O Igonkina[105], Y Ikegami[66], M Ikeno[66], Y Ilchenko[39], D Iliadis[154], D Imbault[78], M Imhaeuser[174], M Imori[155], T Ince[20], J Inigo-Golfin[29], P Ioannou[8], M Iodice[134a], G Ionescu[4], A Irles Quiles[167], K Ishii[66], A Ishikawa[67], M Ishino[66], R Ishmukhametov[39], T Isobe[155], C Issever[118], S Istin[18a], Y Itoh[101], A V Ivashin[128], W Iwanski[38], H Iwasaki[66], J M Izen[40], V Izzo[102a], B Jackson[120], J N Jackson[73], P Jackson[143], M R Jaekel[29], V Jain[61], K Jakobs[48], S Jakobsen[35], J Jakubek[127], D K Jana[111], E Jankowski[158], E Jansen[77], A Jantsch[99], M Janus[20], G Jarlskog[79], L Jeanty[57], K Jelen[37], I Jen-La Plante[30], P Jenni[29], A Jeremie[4], P Jež[35], S Jézéquel[4], H Ji[172], W Ji[81], J Jia[148], Y Jiang[32b], M Jimenez Belenguer[29], G Jin[32b], S Jin[32a], O Jinnouchi[157], M D Joergensen[35], D Joffe[39], L G Johansen[13], M Johansen[146a,146b], K E Johansson[146a], P Johansson[139], S Johnert[41], K A Johns[6], K Jon-And[146a,146b], G Jones[82], R W L Jones[71], T W Jones[77], T J Jones[73], O Jonsson[29], K K Joo[158], C Joram[29], P M Jorge[124a,179], J Joseph[14], X Ju[130], V Juranek[125], P Jussel[62], V V Kabachenko[128], S Kabana[16], M Kaci[167], A Kaczmarska[38], P Kadlecik[35], M Kado[115], H Kagan[109], M Kagan[57], S Kaiser[99], E Kajomovitz[152], S Kalinin[174], L V Kalinovskaya[65], S Kama[39], N Kanaya[155], M Kaneda[155], T Kanno[157], V A Kantserov[96], J Kanzaki[66], B Kaplan[175], A Kapliy[30], J Kaplon[29], D Kar[43], M Karagoz[118], M Karnevskiy[41], K Karr[5], V Kartvelishvili[71], A N Karyukhin[128], L Kashif[57], A Kasmi[39], R D Kass[109], A Kastanas[13], M Kataoka[4], Y Kataoka[155], E Katsoufis[9], J Katzy[41], V Kaushik[6], K Kawagoe[67], T Kawamoto[155], G Kawamura[81], M S Kayl[105], V A Kazanin[107], M Y Kazarinov[65], S I Kazi[86], J R Keates[82], R Keeler[169], R Kehoe[39], M Keil[54], G D Kekelidze[65], M Kelly[82], J Kennedy[98], C J Kenney[143], M Kenyon[53], O Kepka[125], N Kerschen[29], B P Kerševan[74], S Kersten[174], K Kessoku[155], C

Ketterer[48], M Khakzad[28], F Khalil-zada[10], H Khandanyan[165], A Khanov[112], D Kharchenko[65], A Khodinov[148], A G Kholodenko[128], A Khomich[58a], T J Khoo[27], G Khoriauli[20], N Khovanskiy[65], V Khovanskiy[95], E Khramov[65], J Khubua[51], G Kilvington[76], H Kim[7], M S Kim[2], P C Kim[143], S H Kim[160], N Kimura[170], O Kind[15], B T King[73], M King[67], R S B King[118], J Kirk[129], G P Kirsch[118], L E Kirsch[22], A E Kiryunin[99], D Kisielewska[37], T Kittelmann[123], A M Kiver[128], H Kiyamura[67], E Kladiva[144b], J Klaiber-Lodewigs[42], M Klein[73], U Klein[73], K Kleinknecht[81], M Klemetti[85], A Klier[171], A Klimentov[24], R Klingenberg[42], E B Klinkby[35], T Klioutchnikova[29], P F Klok[104], S Klous[105], E-E Kluge[58a], T Kluge[73], P Kluit[105], S Kluth[99], E Kneringer[62], J Knobloch[29], A Knue[54], B R Ko[44], T Kobayashi[155], M Kobel[43], B Koblitz[29], M Kocian[143], A Kocnar[113], P Kodys[126], K Köneke[29], A C König[104], S Koenig[81], S König[48], L Köpke[81], F Koetsveld[104], P Koevesarki[20], T Koffas[29], E Koffeman[105], F Kohn[54], Z Kohout[127], T Kohriki[66], T Koi[143], T Kokott[20], G M Kolachev[107], H Kolanoski[15], V Kolesnikov[65], I Koletsou[89a,89b], J Koll[88], D Kollar[29], M Kollefrath[48], S D Kolya[82], A A Komar[94], J R Komaragiri[142], T Kondo[66], T Kono[41,193], A I Kononov[48], R Konoplich[108,194], N Konstantinidis[77], A Kootz[174], S Koperny[37], S V Kopikov[128], K Korcyl[38], K Kordas[154], V Koreshev[128], A Korn[14], A Korol[107], I Korolkov[11], E V Korolkova[139], V A Korotkov[128], O Kortner[99], S Kortner[99], V V Kostyukhin[20], M J Kotamäki[29], S Kotov[99], V M Kotov[65], C Kourkoumelis[8], A Koutsman[105], R Kowalewski[169], T Z Kowalski[37], W Kozanecki[136], A S Kozhin[128], V Kral[127], V A Kramarenko[97], G Kramberger[74], O Krasel[42], M W Krasny[78], A Krasznahorkay[108], J Kraus[88], A Kreisel[153], F Krejci[127], J Kretzschmar[73], N Krieger[54], P Krieger[158], K Kroeninger[54], H Kroha[99], J Kroll[120], J Kroseberg[20], J Krstic[12a], U Kruchonak[65], H Krüger[20], Z V Krumshteyn[65], A Kruth[20], T Kubota[155], S Kuehn[48], A Kugel[58c], T Kuhl[174], D Kuhn[62], V Kukhtin[65], Y Kulchitsky[90], S Kuleshov[31b], C Kummer[98], M Kuna[83], N Kundu[118], J Kunkle[120], A Kupco[125], H Kurashige[67], M Kurata[160], Y A Kurochkin[90], V Kus[125], W Kuykendall[138], M Kuze[157], P Kuzhir[91], O Kvasnicka[125], R Kwee[15], A La Rosa[29], L La Rotonda[36a,36b], L Labarga[80], J Labbe[4], C Lacasta[167], F Lacava[132a,132b], H Lacker[15], D Lacour[78], V R Lacuesta[167], E Ladygin[65], R Lafaye[4], B Laforge[78], T Lagouri[80], S Lai[48], E Laisne[55], M Lamanna[29], C L Lampen[6], W Lampl[6], E Lancon[136], U Landgraf[48], M P J Landon[75], H Landsman[152], J L Lane[82], C Lange[41], A J Lankford[163], F Lanni[24], K Lantzsch[29], V V Lapin[128,208], S Laplace[4], C Lapoire[20], J F Laporte[136], T Lari[89a], A V Larionov[128], A Larner[118], C Lasseur[29], M Lassnig[29], W Lau[118], P Laurelli[47], A Lavorato[118], W Lavrijsen[14], P Laycock[73], A B Lazarev[65], A Lazzaro[89a,89b], O Le Dortz[78], E Le Guirriec[83], C Le Maner[158], E Le Menedeu[136], M Leahu[29], A Lebedev[64], C Lebel[93], T LeCompte[5], F Ledroit-Guillon[55], H Lee[105], J S H Lee[150], S C Lee[151], L Lee[175], M Lefebvre[169], M Legendre[136], A Leger[49], B C LeGeyt[120], F Legger[98], C Leggett[14], M Lehmacher[20], G Lehmann Miotto[29], M Lehto[139], X Lei[6], M A L Leite[23b], R Leitner[126], D Lellouch[171], J Lellouch[78], M Leltchouk[34], V Lendermann[58a], K J C Leney[145b], T Lenz[174], G Lenzen[174], B Lenzi[136], K Leonhardt[43], S Leontsinis[9], C Leroy[93], J-R Lessard[169], J Lesser[146a], C G Lester[27], A Leung Fook Cheong[172], J Levêque[83], D Levin[87], L J Levinson[171], M S Levitski[128], M Lewandowska[21], M Leyton[15], B Li[83], H Li[172], S Li[32b], X Li[87], Z Liang[39], Z Liang[118,195], B Liberti[133a], P Lichard[29], M Lichtnecker[98], K Lie[165], W Liebig[13], R Lifshitz[152], J N Lilley[17], A Limosani[86], M Limper[63], S C Lin[151,196], F Linde[105], J T Linnemann[88], E Lipeles[120], L Lipinsky[125], A Lipniacka[13], T M Liss[165], A Lister[49], A M Litke[137], C Liu[28], D Liu[151,197], H Liu[87], J B Liu[87], M Liu[32b], S Liu[2], Y Liu[32b], M Livan[119a,119b], S S A Livermore[118], A Lleres[55], S L Lloyd[75], E Lobodzinska[41], P Loch[6], W S Lockman[137], S Lockwitz[175], T Loddenkoetter[20], F K Loebinger[82], A Loginov[175], C W Loh[168], T Lohse[15], K Lohwasser[48], M Lokajicek[125], J Loken[118], V P Lombardo[89a,89b], R E Long[71], L Lopes[124a,179], D Lopez Mateos[34,190], M Losada[162], P Loscutoff[14], F Lo Sterzo[132a,132b], M J Losty[159a], X Lou[40], A Lounis[115], K F Loureiro[162], J Love[21],

P A Love[71], A J Lowe[143], F Lu[32a], J Lu[2], L Lu[39], H J Lubatti[138], C Luci[132a,132b], A Lucotte[55], A Ludwig[43], D Ludwig[41], I Ludwig[48], J Ludwig[48], F Luehring[61], G Luijckx[105], D Lumb[48], L Luminari[132a], E Lund[117], B Lund-Jensen[147], B Lundberg[79], J Lundberg[146a,146b], J Lundquist[35], M Lungwitz[81], A Lupi[122a,122b], G Lutz[99], D Lynn[24], J Lys[14], E Lytken[79], H Ma[24], L L Ma[172], M Maaßen[48], J A Macana Goia[93], G Maccarrone[47], A Macchiolo[99], B Maček[74], J Machado Miguens[124a,179], D Macina[49], R Mackeprang[35], R J Madaras[14], W F Mader[43], R Maenner[58c], T Maeno[24], P Mättig[174], S Mättig[41], P J Magalhaes Martins[124a,183], L Magnoni[29], E Magradze[51], C A Magrath[104], Y Mahalalel[153], K Mahboubi[48], G Mahout[17], C Maiani[132a,132b], C Maidantchik[23a], A Maio[124a,189], S Majewski[24], Y Makida[66], N Makovec[115], P Mal[6], Pa Malecki[38], P Malecki[38], V P Maleev[121], F Malek[55], U Mallik[63], D Malon[5], S Maltezos[9], V Malyshev[107], S Malyukov[65], R Mameghani[98], J Mamuzic[12b], A Manabe[66], L Mandelli[89a], I Mandić[74], R Mandrysch[15], J Maneira[124a], P S Mangeard[88], I D Manjavidze[65], A Mann[54], P M Manning[137], A Manousakis-Katsikakis[8], B Mansoulie[136], A Manz[99], A Mapelli[29], L Mapelli[29], L March[80], J F Marchand[29], F Marchese[133a,133b], M Marchesotti[29], G Marchiori[78], M Marcisovsky[125], A Marin[21,208], C P Marino[61], F Marroquim[23a], R Marshall[82], Z Marshall[34,190], F K Martens[158], S Marti-Garcia[167], A J Martin[175], B Martin[29], B Martin[88], F F Martin[120], J P Martin[93], Ph Martin[55], T A Martin[17], B Martin dit Latour[49], M Martinez[11], V Martinez Outschoorn[57], A C Martyniuk[82], M Marx[82], F Marzano[132a], A Marzin[111], L Masetti[81], T Mashimo[155], R Mashinistov[94], J Masik[82], A L Maslennikov[107], M Maß[42], I Massa[19a,19b], G Massaro[105], N Massol[4], A Mastroberardino[36a,36b], T Masubuchi[155], M Mathes[20], P Matricon[115], H Matsumoto[155], H Matsunaga[155], T Matsushita[67], C Mattravers[118,198], J M Maugain[29], S J Maxfield[73], E N May[5], A Mayne[139], R Mazini[151], M Mazur[20], M Mazzanti[89a], E Mazzoni[122a,122b], S P Mc Kee[87], A McCarn[165], R L McCarthy[148], T G McCarthy[28], N A McCubbin[129], K W McFarlane[56], J A Mcfayden[139], H McGlone[53], G Mchedlidze[51], R A McLaren[29], T Mclaughlan[17], S J McMahon[129], T R McMahon[76], T J McMahon[17], R A McPherson[169,185], A Meade[84], J Mechnich[105], M Mechtel[174], M Medinnis[41], R Meera-Lebbai[111], T Meguro[116], R Mehdiyev[93], S Mehlhase[41], A Mehta[73], K Meier[58a], J Meinhardt[48], B Meirose[79], C Melachrinos[30], B R Mellado Garcia[172], L Mendoza Navas[162], Z Meng[151,197], A Mengarelli[19a,19b], S Menke[99], C Menot[29], E Meoni[11], D Merkl[98], P Mermod[118], L Merola[102a,102b], C Meroni[89a], F S Merritt[30], A Messina[29], J Metcalfe[103], A S Mete[64], S Meuser[20], C Meyer[81], J-P Meyer[136], J Meyer[173], J Meyer[54], T C Meyer[29], W T Meyer[64], J Miao[32d], S Michal[29], L Micu[25a], R P Middleton[129], P Miele[29], S Migas[73], L Mijović[41], G Mikenberg[171], M Mikestikova[125], B Mikulec[49], M Mikuž[74], D W Miller[143], R J Miller[88], W J Mills[168], C Mills[57], A Milov[171], D A Milstead[146a,146b], D Milstein[171], A A Minaenko[128], M Miñano[167], I A Minashvili[65], A I Mincer[108], B Mindur[37], M Mineev[65], Y Ming[130], L M Mir[11], G Mirabelli[132a], L Miralles Verge[11], A Misiejuk[76], A Mitra[118], J Mitrevski[137], G Y Mitrofanov[128], V A Mitsou[167], S Mitsui[66], P S Miyagawa[82], K Miyazaki[67], J U Mjörnmark[79], T Moa[146a,146b], P Mockett[138], S Moed[57], V Moeller[27], K Mönig[41], N Möser[20], S Mohapatra[148], B Mohn[13], W Mohr[48], S Mohrdieck-Möck[99], A M Moisseev[128,208], R Moles-Valls[167], J Molina-Perez[29], L Moneta[49], J Monk[77], E Monnier[83], S Montesano[89a,89b], F Monticelli[70], S Monzani[19a,19b], R W Moore[2], G F Moorhead[86], C Mora Herrera[49], A Moraes[53], A Morais[124a,179], N Morange[136], J Morel[54], G Morello[36a,36b], D Moreno[81], M Moreno Llácer[167], P Morettini[50a], M Morii[57], J Morin[75], Y Morita[66], A K Morley[29], G Mornacchi[29], M-C Morone[49], J D Morris[75], H G Moser[99], M Mosidze[51], J Moss[109], R Mount[143], E Mountricha[9], S V Mouraviev[94], E J W Moyse[84], M Mudrinic[12b], F Mueller[58a], J Mueller[123], K Mueller[20], T A Müller[98], D Muenstermann[42], A Muijs[105], A Muir[168], Y Munwes[153], K Murakami[66], W J Murray[129], I Mussche[105], E Musto[102a,102b], A G Myagkov[128], M Myska[125], J Nadal[11], K Nagai[160], K

Nagano[66], Y Nagasaka[60], A M Nairz[29], Y Nakahama[115], K Nakamura[155], I Nakano[110], G Nanava[20], A Napier[161], M Nash[77,198], I Nasteva[82], N R Nation[21], T Nattermann[20], T Naumann[41], G Navarro[162], H A Neal[87], E Nebot[80], P Yu Nechaeva[94], A Negri[119a,119b], G Negri[29], S Nektarijevic[49], A Nelson[64], S Nelson[143], T K Nelson[143], S Nemecek[125], P Nemethy[108], A A Nepomuceno[23a], M Nessi[29], S Y Nesterov[121], M S Neubauer[165], A Neusiedl[81], R M Neves[108], P Nevski[24], P R Newman[17], R B Nickerson[118], R Nicolaidou[136], L Nicolas[139], B Nicquevert[29], F Niedercorn[115], J Nielsen[137], T Niinikoski[29], A Nikiforov[15], V Nikolaenko[128], K Nikolaev[65], I Nikolic-Audit[78], K Nikolopoulos[24], H Nilsen[48], P Nilsson[7], Y Ninomiya[155], A Nisati[132a], T Nishiyama[67], R Nisius[99], L Nodulman[5], M Nomachi[116], I Nomidis[154], H Nomoto[155], M Nordberg[29], B Nordkvist[146a,146b], O Norniella Francisco[11], P R Norton[129], J Novakova[126], M Nozaki[66], M Nožička[41], I M Nugent[159a], A-E Nuncio-Quiroz[20], G Nunes Hanninger[20], T Nunnemann[98], E Nurse[77], T Nyman[29], B J O'Brien[45], S W O'Neale[17,208], D C O'Neil[142], V O'Shea[53], F G Oakham[28,181], H Oberlack[99], J Ocariz[78], A Ochi[67], S Oda[155], S Odaka[66], J Odier[83], G A Odino[50a,50b], H Ogren[61], A Oh[82], S H Oh[44], C C Ohm[146a,146b], T Ohshima[101], H Ohshita[140], T K Ohska[66], T Ohsugi[59], S Okada[67], H Okawa[163], Y Okumura[101], T Okuyama[155], M Olcese[50a], A G Olchevski[65], M Oliveira[124a,183], D Oliveira Damazio[24], E Oliver Garcia[167], D Olivito[120], A Olszewski[38], J Olszowska[38], C Omachi[67], A Onofre[124a,199], P U E Onyisi[30], C J Oram[159a], G Ordonez[104], M J Oreglia[30], F Orellana[49], Y Oren[153], D Orestano[134a,134b], I Orlov[107], C Oropeza Barrera[53], R S Orr[158], E O Ortega[130], B Osculati[50a,50b], R Ospanov[120], C Osuna[11], G Otero y Garzon[26], J P Ottersbach[105], M Ouchrif[135c], F Ould-Saada[117], A Ouraou[136], Q Ouyang[32a], M Owen[82], S Owen[139], A Oyarzun[31b], O K Øye[13], V E Ozcan[77], N Ozturk[7], A Pacheco Pages[11], C Padilla Aranda[11], E Paganis[139], F Paige[24], K Pajchel[117], S Palestini[29], D Pallin[33], A Palma[124a,179], J D Palmer[17], Y B Pan[172], E Panagiotopoulou[9], B Panes[31a], N Panikashvili[87], S Panitkin[24], D Pantea[25a], M Panuskova[125], V Paolone[123], A Paoloni[133a,133b], A Papadelis[146a], Th D Papadopoulou[9], A Paramonov[5], S J Park[54], W Park[24,200], M A Parker[27], F Parodi[50a,50b], J A Parsons[34], U Parzefall[48], E Pasqualucci[132a], A Passeri[134a], F Pastore[134a,134b], Fr Pastore[29], G Pásztor[49,201], S Pataraia[172], N Patel[150], J R Pater[82], S Patricelli[102a,102b], T Pauly[29], M Pecsy[144a], M I Pedraza Morales[172], S V Peleganchuk[107], H Peng[172], R Pengo[29], A Penson[34], J Penwell[61], M Perantoni[23a], K Perez[34,190], T Perez Cavalcanti[41], E Perez Codina[11], M T Pérez García-Estañ[167], V Perez Reale[34], I Peric[20], L Perini[89a,89b], H Pernegger[29], R Perrino[72a], P Perrodo[4], S Persembe[3a], P Perus[115], V D Peshekhonov[65], O Peters[105], B A Petersen[29], J Petersen[29], T C Petersen[35], E Petit[83], A Petridis[154], C Petridou[154], E Petrolo[132a], F Petrucci[134a,134b], D Petschull[41], M Petteni[142], R Pezoa[31b], A Phan[86], A W Phillips[27], P W Phillips[129], G Piacquadio[29], E Piccaro[75], M Piccinini[19a,19b], A Pickford[53], R Piegaia[26], J E Pilcher[30], A D Pilkington[82], J Pina[124a,189], M Pinamonti[164a,164c], A Pinder[118], J L Pinfold[2], J Ping[32c], B Pinto[124a,179], O Pirotte[29], C Pizio[89a,89b], R Placakyte[41], M Plamondon[169], W G Plano[82], M-A Pleier[24], A V Pleskach[128], A Poblaguev[24], S Poddar[58a], F Podlyski[33], L Poggioli[115], T Poghosyan[20], M Pohl[49], F Polci[55], G Polesello[119a], A Policicchio[138], A Polini[19a], J Poll[75], V Polychronakos[24], D M Pomarede[136], D Pomeroy[22], K Pommès[29], L Pontecorvo[132a], B G Pope[88], G A Popeneciu[25a], D S Popovic[12a], A Poppleton[29], X Portell Bueso[48], R Porter[163], C Posch[21], G E Pospelov[99], S Pospisil[127], I N Potrap[99], C J Potter[149], C T Potter[85], G Poulard[29], J Poveda[172], R Prabhu[77], P Pralavorio[83], S Prasad[57], R Pravahan[7], S Prell[64], K Pretzl[16], L Pribyl[29], D Price[61], L E Price[5], M J Price[29], P M Prichard[73], D Prieur[123], M Primavera[72a], K Prokofiev[29], F Prokoshin[31b], S Protopopescu[24], J Proudfoot[5], X Prudent[43], H Przysiezniak[4], S Psoroulas[20], E Ptacek[114], J Purdham[87], M Purohit[24,200], P Puzo[115], Y Pylypchenko[117], J Qian[87], Z Qian[83], Z Qin[41], A Quadt[54], D R Quarrie[14], W B Quayle[172], F Quinonez[31a], M Raas[104], V Radescu[58b], B

Radics[20], T Rador[18a], F Ragusa[89a,89b], G Rahal[177], A M Rahimi[109], S Rajagopalan[24], S Rajek[42], M Rammensee[48], M Rammes[141], M Ramstedt[146a,146b], K Randrianarivony[28], P N Ratoff[71], F Rauscher[98], E Rauter[99], M Raymond[29], A L Read[117], D M Rebuzzi[119a,119b], A Redelbach[173], G Redlinger[24], R Reece[120], K Reeves[40], A Reichold[105], E Reinherz-Aronis[153], A Reinsch[114], I Reisinger[42], D Reljic[12a], C Rembser[29], Z L Ren[151], A Renaud[115], P Renkel[39], B Rensch[35], M Rescigno[132a], S Resconi[89a], B Resende[136], P Reznicek[98], R Rezvani[158], A Richards[77], R Richter[99], E Richter-Was[38,202], M Ridel[78], S Rieke[81], M Rijpstra[105], M Rijssenbeek[148], A Rimoldi[119a,119b], L Rinaldi[19a], R R Rios[39], I Riu[11], G Rivoltella[89a,89b], F Rizatdinova[112], E Rizvi[75], S H Robertson[85,185], A Robichaud-Veronneau[49], D Robinson[27], J E M Robinson[77], M Robinson[114], A Robson[53], J G Rocha de Lima[106], C Roda[122a,122b], D Roda Dos Santos[29], S Rodier[80], D Rodriguez[162], Y Rodriguez Garcia[15], A Roe[54], S Roe[29], O Røhne[117], V Rojo[1], S Rolli[161], A Romaniouk[96], V M Romanov[65], G Romeo[26], D Romero Maltrana[31a], L Roos[78], E Ros[167], S Rosati[138], M Rose[76], G A Rosenbaum[158], E I Rosenberg[64], P L Rosendahl[13], L Rosselet[49], V Rossetti[11], E Rossi[102a,102b], L P Rossi[50a], L Rossi[89a,89b], M Rotaru[25a], I Roth[171], J Rothberg[138], I Rottländer[20], D Rousseau[115], C R Royon[136], A Rozanov[83], Y Rozen[152], X Ruan[115], I Rubinskiy[41], B Ruckert[98], N Ruckstuhl[105], V I Rud[97], G Rudolph[62], F Rühr[6], A Ruiz-Martinez[64], E Rulikowska-Zarebska[37], V Rumiantsev[91,208], L Rumyantsev[65], K Runge[48], O Runolfsson[20], Z Rurikova[48], N A Rusakovich[65], D R Rust[61], J P Rutherfoord[6], C Ruwiedel[14], P Ruzicka[125], Y F Ryabov[121], V Ryadovikov[128], P Ryan[88], M Rybar[126], G Rybkin[115], N C Ryder[118], S Rzaeva[10], A F Saavedra[150], I Sadeh[153], H F-W Sadrozinski[137], R Sadykov[65], F Safai Tehrani[132a,132b], H Sakamoto[155], G Salamanna[105], A Salamon[133a], M Saleem[111], D Salihagic[99], A Salnikov[143], J Salt[167], B M Salvachua Ferrando[5], D Salvatore[36a,36b], F Salvatore[149], A Salzburger[29], D Sampsonidis[154], B H Samset[117], H Sandaker[13], H G Sander[81], M P Sanders[98], M Sandhoff[174], P Sandhu[158], T Sandoval[27], R Sandstroem[105], S Sandvoss[174], D P C Sankey[129], A Sansoni[47], C Santamarina Rios[85], C Santoni[33], R Santonico[133a,133b], H Santos[124a], J G Saraiva[124a,189], T Sarangi[172], E Sarkisyan-Grinbaum[7], F Sarri[122a,122b], G Sartisohn[174], O Sasaki[66], T Sasaki[66], N Sasao[68], I Satsounkevitch[90], G Sauvage[4], J B Sauvan[115], P Savard[158,181], V Savinov[123], P Savva[9], L Sawyer[24,186], D H Saxon[53], L P Says[33], C Sbarra[19a,19b], A Sbrizzi[19a,19b], O Scallon[93], D A Scannicchio[163], J Schaarschmidt[43], P Schacht[99], U Schäfer[81], S Schaetzel[58b], A C Schaffer[115], D Schaile[98], R D Schamberger[148], A G Schamov[107], V Scharf[58a], V A Schegelsky[121], D Scheirich[87], M I Scherzer[14], C Schiavi[50a,50b], J Schieck[98], M Schioppa[36a,36b], S Schlenker[29], J L Schlereth[5], E Schmidt[48], M P Schmidt[175,208], K Schmieden[20], C Schmitt[81], M Schmitz[20], A Schöning[58b], M Schott[29], D Schouten[142], J Schovancova[125], M Schram[85], A Schreiner[63], C Schroeder[81], N Schroer[58c], S Schuh[29], G Schuler[29], J Schultes[174], H-C Schultz-Coulon[58a], H Schulz[15], J W Schumacher[20], M Schumacher[48], B A Schumm[137], Ph Schune[136], C Schwanenberger[82], A Schwartzman[143], Ph Schwemling[78], R Schwienhorst[88], R Schwierz[43], J Schwindling[136], W G Scott[129], J Searcy[114], E Sedykh[121], E Segura[11], S C Seidel[103], A Seiden[137], F Seifert[43], J M Seixas[23a], G Sekhniaidze[102a], D M Seliverstov[121], B Sellden[146a], G Sellers[73], M Seman[144b], N Semprini-Cesari[19a,19b], C Serfon[98], L Serin[115], R Seuster[99], H Severini[111], M E Sevior[86], A Sfyrla[29], E Shabalina[54], M Shamim[114], L Y Shan[32a], J T Shank[21], Q T Shao[86], M Shapiro[14], P B Shatalov[95], L Shaver[6], C Shaw[53], K Shaw[164a,164c], D Sherman[175], P Sherwood[77], A Shibata[108], S Shimizu[29], M Shimojima[100], T Shin[56], A Shmeleva[94], M J Shochet[30], D Short[118], M A Shupe[6], P Sicho[125], A Sidoti[15], A Siebel[174], F Siegert[48], J Siegrist[14], Dj Sijacki[12a], O Silbert[171], J Silva[124a,203], Y Silver[153], D Silverstein[143], S B Silverstein[146a], V Simak[127], Lj Simic[12a], S Simion[115], B Simmons[77], M Simonyan[35], P Sinervo[158], N B Sinev[114], V Sipica[141], G Siragusa[81], A N Sisakyan[65], S Yu Sivoklokov[97], J Sjölin[146a,146b], T B Sjursen[13], L A

Skinnari[14], K Skovpen[107], P Skubic[111], N Skvorodnev[22], M Slater[17], T Slavicek[127], K Sliwa[161], T J Sloan[71], J Sloper[29], V Smakhtin[171], S Yu Smirnov[96], L N Smirnova[97], O Smirnova[79], B C Smith[57], D Smith[143], K M Smith[53], M Smizanska[71], K Smolek[127], A A Snesarev[94], S W Snow[82], J Snow[111], J Snuverink[105], S Snyder[24], M Soares[124a], R Sobie[169,185], J Sodomka[127], A Soffer[153], C A Solans[167], M Solar[127], J Solc[127], U Soldevila[167], E Solfaroli Camillocci[132a,132b], A A Solodkov[128], O V Solovyanov[128], J Sondericker[24], N Soni[2], V Sopko[127], B Sopko[127], M Sorbi[89a,89b], M Sosebee[7], A Soukharev[107], S Spagnolo[72a,72b], F Spanò[34], R Spighi[19a], G Spigo[29], F Spila[132a,132b], E Spiriti[134a], R Spiwoks[29], M Spousta[126], T Spreitzer[158], B Spurlock[7], R D St Denis[53], T Stahl[141], J Stahlman[120], R Stamen[58a], E Stanecka[29], R W Stanek[5], C Stanescu[134a], S Stapnes[117], E A Starchenko[128], J Stark[55], P Staroba[125], P Starovoitov[91], A Staude[98], P Stavina[144a], G Stavropoulos[14], G Steele[53], P Steinbach[43], P Steinberg[24], I Stekl[127], B Stelzer[142], H J Stelzer[41], O Stelzer-Chilton[159a], H Stenzel[52], K Stevenson[75], G A Stewart[53], T Stockmanns[20], M C Stockton[29], K Stoerig[48], G Stoicea[25a], S Stonjek[99], P Strachota[126], A R Stradling[7], A Straessner[43], J Strandberg[87], S Strandberg[146a,146b], A Strandlie[117], M Strang[109], E Strauss[143], M Strauss[111], P Strizenec[144b], R Ströhmer[173], D M Strom[114], J A Strong[76,208], R Stroynowski[39], J Strube[129], B Stugu[13], I Stumer[24,208], J Stupak[148], P Sturm[174], D A Soh[151,195], D Su[143], S Subramania[2], Y Sugaya[116], T Sugimoto[101], C Suhr[106], K Suita[67], M Suk[126], V V Sulin[94], S Sultansoy[3d], T Sumida[29], X Sun[55], J E Sundermann[48], K Suruliz[164a,164b], S Sushkov[11], G Susinno[36a,36b], M R Sutton[139], Y Suzuki[66], Yu M Sviridov[128], S Swedish[168], I Sykora[144a], T Sykora[126], B Szeless[29], J Sánchez[167], D Ta[105], K Tackmann[29], A Taffard[163], R Tafirout[159a], A Taga[117], N Taiblum[153], Y Takahashi[101], H Takai[24], R Takashima[69], H Takeda[67], T Takeshita[140], M Talby[83], A Talyshev[107], M C Tamsett[24], J Tanaka[155], R Tanaka[115], S Tanaka[131], S Tanaka[66], Y Tanaka[100], K Tani[67], N Tannoury[83], G P Tappern[29], S Tapprogge[81], D Tardif[158], S Tarem[152], F Tarrade[24], G F Tartarelli[89a], P Tas[126], M Tasevsky[125], E Tassi[36a,36b], M Tatarkhanov[14], C Taylor[77], F E Taylor[92], G Taylor[137], G N Taylor[86], W Taylor[159b], M Teixeira Dias Castanheira[75], P Teixeira-Dias[76], K K Temming[48], H Ten Kate[29], P K Teng[151], Y D Tennenbaum-Katan[152], S Terada[66], K Terashi[155], J Terron[80], M Terwort[41,193], M Testa[47], R J Teuscher[158,185], C M Tevlin[82], J Thadome[174], J Therhaag[20], T Theveneaux-Pelzer[78], M Thioye[175], S Thoma[48], J P Thomas[17], E N Thompson[84], P D Thompson[17], P D Thompson[158], A S Thompson[53], E Thomson[120], M Thomson[27], R P Thun[87], T Tic[125], V O Tikhomirov[94], Y A Tikhonov[107], C J W P Timmermans[104], P Tipton[175], F J Tique Aires Viegas[29], S Tisserant[83], J Tobias[48], B Toczek[37], T Todorov[4], S Todorova-Nova[161], B Toggerson[163], J Tojo[66], S Tokár[144a], K Tokunaga[67], K Tokushuku[66], K Tollefson[88], M Tomoto[101], L Tompkins[14], K Toms[103], A Tonazzo[134a,134b], G Tong[32a], A Tonoyan[13], C Topfel[16], N D Topilin[65], I Torchiani[29], E Torrence[114], E Torró Pastor[167], J Toth[83,201], F Touchard[83], D R Tovey[139], D Traynor[75], T Trefzger[173], J Treis[20], L Tremblet[29], A Tricoli[29], I M Trigger[159a], S Trincaz-Duvoid[78], T N Trinh[78], M F Tripiana[70], N Triplett[64], W Trischuk[158], A Trivedi[24,200], B Trocmé[55], C Troncon[89a], M Trottier-McDonald[142], A Trzupek[38], C Tsarouchas[29], J C-L Tseng[118], M Tsiakiris[105], P V Tsiareshka[90], D Tsionou[4], G Tsipolitis[9], V Tsiskaridze[48], E G Tskhadadze[51], I I Tsukerman[95], V Tsulaia[123], J-W Tsung[20], S Tsuno[66], D Tsybychev[148], A Tua[139], J M Tuggle[30], M Turala[38], D Turecek[127], I Turk Cakir[3e], E Turlay[105], P M Tuts[34], A Tykhonov[74], M Tylmad[146a,146b], M Tyndel[129], D Typaldos[17], H Tyrvainen[29], G Tzanakos[8], K Uchida[20], I Ueda[155], R Ueno[28], M Ugland[13], M Uhlenbrock[20], M Uhrmacher[54], F Ukegawa[160], G Unal[29], D G Underwood[5], A Undrus[24], G Unel[163], Y Unno[66], D Urbaniec[34], E Urkovsky[153], P Urquijo[49], P Urrejola[31a], G Usai[7], M Uslenghi[119a,119b], L Vacavant[83], V Vacek[127], B Vachon[85], S Vahsen[14], C Valderanis[99], J Valenta[125], P Valente[132a], S Valentinetti[19a,19b], S Valkar[126], E Valladolid Gallego[167], S Vallecorsa[152], J A Valls Ferrer[167], H van der Graaf[105],

E van der Kraaij[105], E van der Poel[105], D van der Ster[29], B Van Eijk[105], N van Eldik[84], P van Gemmeren[5], Z van Kesteren[105], I van Vulpen[105], W Vandelli[29], G Vandoni[29], A Vaniachine[5], P Vankov[41], F Vannucci[78], F Varela Rodriguez[29], R Vari[132a], E W Varnes[6], D Varouchas[14], A Vartapetian[7], K E Varvell[150], V I Vassilakopoulos[56], F Vazeille[33], G Vegni[89a,89b], J J Veillet[115], C Vellidis[8], F Veloso[124a], R Veness[29], S Veneziano[132a], A Ventura[72a,72b], D Ventura[138], S Ventura[47], M Venturi[48], N Venturi[16], V Vercesi[119a], M Verducci[138], W Verkerke[105], J C Vermeulen[105], A Vest[43], M C Vetterli[142,181], I Vichou[165], T Vickey[145b,204], G H A Viehhauser[118], S Viel[168], M Villa[19a,19b], M Villaplana Perez[167], E Vilucchi[47], M G Vincter[28], E Vinek[29], V B Vinogradov[65], M Virchaux[136,208], S Viret[33], J Virzi[14], A Vitale[19a,19b], O Vitells[171], I Vivarelli[48], F Vives Vaque[11], S Vlachos[9], M Vlasak[127], N Vlasov[20], A Vogel[20], P Vokac[127], M Volpi[11], G Volpini[89a], H von der Schmitt[99], J von Loeben[99], H von Radziewski[48], E von Toerne[20], V Vorobel[126], A P Vorobiev[128], V Vorwerk[11], M Vos[167], R Voss[29], T T Voss[174], J H Vossebeld[73], A S Vovenko[128], N Vranjes[12a], M Vranjes Milosavljevic[12a], V Vrba[125], M Vreeswijk[105], T Vu Anh[81], R Vuillermet[29], I Vukotic[115], W Wagner[174], P Wagner[120], H Wahlen[174], J Wakabayashi[101], J Walbersloh[42], S Walch[87], J Walder[71], R Walker[98], W Walkowiak[141], R Wall[175], P Waller[73], C Wang[44], H Wang[172], J Wang[151], J Wang[32d], J C Wang[138], R Wang[103], S M Wang[151], A Warburton[85], C P Ward[27], M Warsinsky[48], P M Watkins[17], A T Watson[17], M F Watson[17], G Watts[138], S Watts[82], A T Waugh[150], B M Waugh[77], J Weber[42], M Weber[129], M S Weber[16], P Weber[54], A R Weidberg[118], J Weingarten[54], C Weiser[48], H Wellenstein[22], P S Wells[29], M Wen[47], T Wenaus[24], S Wendler[123], Z Weng[151,195], T Wengler[29], S Wenig[29], N Wermes[20], M Werner[48], P Werner[29], M Werth[163], M Wessels[58a], K Whalen[28], S J Wheeler-Ellis[163], S P Whitaker[21], A White[7], M J White[86], S White[24], S R Whitehead[118], D Whiteson[163], D Whittington[61], F Wicek[115], D Wicke[174], F J Wickens[129], W Wiedenmann[172], M Wielers[129], P Wienemann[20], C Wiglesworth[73], L A M Wiik[48], A Wildauer[167], M A Wildt[41,193], I Wilhelm[126], H G Wilkens[29], J Z Will[98], E Williams[34], H H Williams[120], W Willis[34], S Willocq[84], J A Wilson[17], M G Wilson[143], A Wilson[87], I Wingerter-Seez[4], S Winkelmann[48], F Winklmeier[29], M Wittgen[143], M W Wolter[38], H Wolters[124a,183], G Wooden[118], B K Wosiek[38], J Wotschack[29], M J Woudstra[84], K Wraight[53], C Wright[53], B Wrona[73], S L Wu[172], X Wu[49], Y Wu[32b], E Wulf[34], R Wunstorf[42], B M Wynne[45], L Xaplanteris[9], S Xella[35], S Xie[48], Y Xie[32a], C Xu[32b], D Xu[139], G Xu[32a], B Yabsley[150], M Yamada[66], A Yamamoto[66], K Yamamoto[64], S Yamamoto[155], T Yamamura[155], J Yamaoka[44], T Yamazaki[155], Y Yamazaki[67], Z Yan[21], H Yang[87], U K Yang[82], Y Yang[61], Y Yang[32a], Z Yang[146a,146b], S Yanush[91], W-M Yao[14], Y Yao[14], Y Yasu[66], J Ye[39], S Ye[24], M Yilmaz[3c], R Yoosoofmiya[123], K Yorita[170], R Yoshida[5], C Young[143], S Youssef[21], D Yu[24], J Yu[7], J Yu[32c,205], L Yuan[32a,206], A Yurkewicz[148], V G Zaets[128], R Zaidan[63], A M Zaitsev[128], Z Zajacova[29], Yo K Zalite[121], L Zanello[132a,132b], P Zarzhitsky[39], A Zaytsev[107], M Zdrazil[14], C Zeitnitz[174], M Zeller[175], P F Zema[29], A Zemla[38], C Zendler[20], A V Zenin[128], O Zenin[128], T Ženiš[144a], Z Zenonos[122a,122b], S Zenz[14], D Zerwas[115], G Zevi della Porta[57], Z Zhan[32d], D Zhang[32b], H Zhang[88], J Zhang[5], X Zhang[32d], Z Zhang[115], L Zhao[108], T Zhao[138], Z Zhao[32b], A Zhemchugov[65], S Zheng[32a], J Zhong[151,207], B Zhou[87], N Zhou[163], Y Zhou[151], C G Zhu[32d], H Zhu[41], Y Zhu[172], X Zhuang[98], V Zhuravlov[99], D Zieminska[61], B Zilka[144a], R Zimmermann[20], S Zimmermann[20], S Zimmermann[48], M Ziolkowski[141], R Zitoun[4], L Živković[34], V V Zmouchko[128,208], G Zobernig[172], A Zoccoli[19a,19b], Y Zolnierowski[4], A Zsenei[29], M zur Nedden[15], V Zutshi[106] and L Zwalinski[29]

[1] University at Albany, 1400 Washington Ave, Albany, NY 12222, USA
[2] University of Alberta, Department of Physics, Centre for Particle Physics, Edmonton, AB T6G 2G7, Canada

58

IOP Institute of Physics   ΦDEUTSCHE PHYSIKALISCHE GESELLSCHAFT

[3a] Ankara University, Faculty of Sciences, Department of Physics, TR 061000 Tandogan, Ankara, Turkey

[3b] Dumlupinar University, Faculty of Arts and Sciences, Department of Physics, Kutahya, Turkey

[3c] Gazi University, Faculty of Arts and Sciences, Department of Physics, 06500, Teknikokullar, Ankara, Turkey

[3d] TOBB University of Economics and Technology, Faculty of Arts and Sciences, Division of Physics, 06560, Sogutozu, Ankara Turkey

[3e] Turkish Atomic Energy Authority, 06530, Lodumlu, Ankara, Turkey

[4] LAPP, Université de Savoie, CNRS/IN2P3, Annecy-le-Vieux, France

[5] Argonne National Laboratory, High Energy Physics Division, 9700 S. Cass Avenue, Argonne IL 60439, USA

[6] University of Arizona, Department of Physics, Tucson, AZ 85721, USA

[7] The University of Texas at Arlington, Department of Physics, Box 19059, Arlington, TX 76019, USA

[8] University of Athens, Nuclear & Particle Physics, Department of Physics, Panepistimiopouli, Zografou, GR 15771 Athens, Greece

[9] National Technical University of Athens, Physics Department, 9-Iroon Polytechniou, GR 15780 Zografou, Greece

[10] Institute of Physics, Azerbaijan Academy of Sciences, H. Javid Avenue 33, AZ 143 Baku, Azerbaijan

[11] Institut de Física d'Altes Energies, IFAE, Edifici Cn, Universitat Autònoma de Barcelona, ES - 08193 Bellaterra (Barcelona), Spain

[12a] University of Belgrade, Institute of Physics, P.O. Box 57, 11001 Belgrade, Serbia

[12b] Vinca Institute of Nuclear Sciences, M. Petrovica Alasa 12-14, 11000 Belgrade, Serbia, Serbia

[13] University of Bergen, Department for Physics and Technology, Allegaten 55, NO - 5007 Bergen, Norway

[14] Lawrence Berkeley National Laboratory and University of California, Physics Division, MS50B-6227, 1 Cyclotron Road, Berkeley, CA 94720, USA

[15] Humboldt University, Institute of Physics, Berlin, Newtonstr. 15, D-12489 Berlin, Germany

[16] University of Bern, Albert Einstein Center for Fundamental Physics, Laboratory for High Energy Physics, Sidlerstrasse 5, CH - 3012 Bern, Switzerland

[17] University of Birmingham, School of Physics and Astronomy, Edgbaston, Birmingham B15 2TT, United Kingdom

[18a] Bogazici University, Faculty of Sciences, Department of Physics, TR - 80815 Bebek-Istanbul, Turkey

[18b] Dogus University, Faculty of Arts and Sciences, Department of Physics, 34722, Kadikoy, Istanbul, Turkey

[18c] Gaziantep University, Faculty of Engineering, Department of Physics Engineering, 27310, Sehitkamil, Gaziantep, Turkey

[18d] Istanbul Technical University, Faculty of Arts and Sciences, Department of Physics, 34469, Maslak, Istanbul, Turkey

[19a] INFN Sezione di Bologna, viale C. Berti Pichat, 6/2, IT - 40127 Bologna, Italy

[19b] Università di Bologna, Dipartimento di Fisica, viale C. Berti Pichat, 6/2, IT - 40127 Bologna, Italy

[20] University of Bonn, Physikalisches Institut, Nussallee 12, D - 53115 Bonn, Germany

[21] Boston University, Department of Physics, 590 Commonwealth Avenue, Boston, MA 02215, USA

[22] Brandeis University, Department of Physics, MS057, 415 South Street, Waltham, MA 02454, USA

[23a] Universidade Federal do Rio De Janeiro, COPPE/EE/IF, Caixa Postal 68528, Ilha do Fundao, BR - 21945-970 Rio de Janeiro, Brazil

[23b] Universidade de Sao Paulo, Instituto de Fisica, R.do Matao Trav. R.187, Sao Paulo - SP, 05508 - 900, Brazil

[24] Brookhaven National Laboratory, Physics Department, Bldg. 510A, Upton, NY 11973, USA

[25a] National Institute of Physics and Nuclear Engineering, Bucharest-Magurele, Str. Atomistilor 407, P.O. Box MG-6, R-077125, Romania

[25b] University Politehnica Bucharest, Rectorat - AN 001, 313 Splaiul Independentei, sector 6, 060042 Bucuresti, Romania

[25c] West University in Timisoara, Bd. Vasile Parvan 4, Timisoara, Romania

[26] Universidad de Buenos Aires, FCEyN, Dto. Fisica, Pab I - C. Universitaria, 1428 Buenos Aires, Argentina

[27] University of Cambridge, Cavendish Laboratory, J J Thomson Avenue, Cambridge CB3 0HE, United Kingdom

[28] Carleton University, Department of Physics, 1125 Colonel By Drive, Ottawa ON K1S 5B6, Canada

[29] CERN, CH - 1211 Geneva 23, Switzerland

[30] University of Chicago, Enrico Fermi Institute, 5640 S. Ellis Avenue, Chicago, IL 60637, USA

[31a] Pontificia Universidad Católica de Chile, Facultad de Fisica, Departamento de Fisica, Avda. Vicuna Mackenna 4860, San Joaquin, Santiago, Chile

[31b] Universidad Técnica Federico Santa María, Departamento de Física, Avda. Espãna 1680, Casilla 110-V, Valparaíso, Chile

[32a] Institute of High Energy Physics, Chinese Academy of Sciences, P.O. Box 918, 19 Yuquan Road, Shijing Shan District, CN - Beijing 100049, China

[32b] University of Science & Technology of China (USTC), Department of Modern Physics, Hefei, CN - Anhui 230026, China

[32c] Nanjing University, Department of Physics, Nanjing, CN - Jiangsu 210093, China

[32d] Shandong University, High Energy Physics Group, Jinan, CN - Shandong 250100, China

[33] Laboratoire de Physique Corpusculaire, Clermont Université, Université Blaise Pascal, CNRS/IN2P3, FR - 63177 Aubiere Cedex, France

[34] Columbia University, Nevis Laboratory, 136 So. Broadway, Irvington, NY 10533, USA

[35] University of Copenhagen, Niels Bohr Institute, Blegdamsvej 17, DK - 2100 Kobenhavn 0, Denmark

[36a] INFN Gruppo Collegato di Cosenza, IT-87036 Arcavacata di Rende, Italy

[36b] Università della Calabria, Dipartimento di Fisica, IT-87036 Arcavacata di Rende, Italy

[37] Faculty of Physics and Applied Computer Science of the AGH-University of Science and Technology, (FPACS, AGH-UST), al. Mickiewicza 30, PL-30059 Cracow, Poland

[38] The Henryk Niewodniczanski Institute of Nuclear Physics, Polish Academy of Sciences, ul. Radzikowskiego 152, PL - 31342 Krakow, Poland

[39] Southern Methodist University, Physics Department, 106 Fondren Science Building, Dallas, TX 75275-0175, USA

[40] University of Texas at Dallas, 800 West Campbell Road, Richardson, TX 75080-3021, USA

[41] DESY, Notkestr. 85, D-22603 Hamburg and Platanenallee 6, D-15738 Zeuthen, Germany

[42] TU Dortmund, Experimentelle Physik IV, DE - 44221 Dortmund, Germany

[43] Technical University Dresden, Institut für Kern- und Teilchenphysik, Zellescher Weg 19, D-01069 Dresden, Germany

[44] Duke University, Department of Physics, Durham, NC 27708, USA

[45] University of Edinburgh, School of Physics & Astronomy, James Clerk Maxwell Building, The Kings Buildings, Mayfield Road, Edinburgh EH9 3JZ, United Kingdom

[46] Fachhochschule Wiener Neustadt; Johannes Gutenbergstrasse 3 AT - 2700 Wiener Neustadt, Austria

[47] INFN Laboratori Nazionali di Frascati, via Enrico Fermi 40, IT-00044 Frascati, Italy

[48] Albert-Ludwigs-Universität, Fakultät für Mathematik und Physik, Hermann-Herder Str. 3, D - 79104 Freiburg i.Br., Germany

[49] Université de Genève, Section de Physique, 24 rue Ernest Ansermet, CH - 1211 Geneve 4, Switzerland

[50a] INFN Sezione di Genova, via Dodecaneso 33, IT - 16146 Genova, Italy

[50b] Università di Genova, Dipartimento di Fisica, via Dodecaneso 33, IT - 16146 Genova, Italy

[51] Institute of Physics of the Georgian Academy of Sciences, 6 Tamarashvili St., GE - 380077 Tbilisi; Tbilisi State University, HEP Institute, University St. 9, GE - 380086 Tbilisi, Georgia

[52] Justus-Liebig-Universität Giessen, II Physikalisches Institut, Heinrich-Buff Ring 16, D-35392 Giessen, Germany

[53] University of Glasgow, Department of Physics and Astronomy, Glasgow G12 8QQ, United Kingdom

[54] Georg-August-Universität, II. Physikalisches Institut, Friedrich-Hund Platz 1, D-37077 Göttingen, Germany

[55] LPSC, CNRS/IN2P3 and Univ. Joseph Fourier Grenoble, 53 avenue des Martyrs, FR-38026 Grenoble Cedex, France

[56] Hampton University, Department of Physics, Hampton, VA 23668, USA

[57] Harvard University, Laboratory for Particle Physics and Cosmology, 18 Hammond Street, Cambridge, MA 02138, USA

[58a] Ruprecht-Karls-Universität Heidelberg: Kirchhoff-Institut für Physik, Im Neuenheimer Feld 227, D-69120 Heidelberg, Germany

[58b] Physikalisches Institut, Philosophenweg 12, D-69120 Heidelberg, Germany

[58c] ZITI Ruprecht-Karls-University Heidelberg, Lehrstuhl für Informatik V, B6, 23-29, DE - 68131 Mannheim, Germany

[59] Hiroshima University, Faculty of Science, 1-3-1 Kagamiyama, Higashihiroshima-shi, JP - Hiroshima 739-8526, Japan

[60] Hiroshima Institute of Technology, Faculty of Applied Information Science, 2-1-1 Miyake Saeki-ku, Hiroshima-shi, JP - Hiroshima 731-5193, Japan

[61] Indiana University, Department of Physics, Swain Hall West 117, Bloomington, IN 47405-7105, USA

[62] Institut für Astro- und Teilchenphysik, Technikerstrasse 25, A - 6020 Innsbruck, Austria

[63] University of Iowa, 203 Van Allen Hall, Iowa City, IA 52242-1479, USA

[64] Iowa State University, Department of Physics and Astronomy, Ames High Energy Physics Group, Ames, IA 50011-3160, USA

[65] Joint Institute for Nuclear Research, JINR Dubna, RU-141980 Moscow Region, Russia, Russia

[66] KEK, High Energy Accelerator Research Organization, 1-1 Oho, Tsukuba-shi, Ibaraki-ken 305-0801, Japan

[67] Kobe University, Graduate School of Science, 1-1 Rokkodai-cho, Nada-ku, JP Kobe 657-8501, Japan

[68] Kyoto University, Faculty of Science, Oiwake-cho, Kitashirakawa, Sakyou-ku, Kyoto-shi, JP - Kyoto 606-8502, Japan

[69] Kyoto University of Education, 1 Fukakusa, Fujimori, fushimi-ku, Kyoto-shi, JP - Kyoto 612-8522, Japan

[70] Universidad Nacional de La Plata, FCE, Departamento de Física, IFLP (CONICET-UNLP), C.C. 67, 1900 La Plata, Argentina

[71] Lancaster University, Physics Department, Lancaster LA1 4YB, United Kingdom

[72a] INFN Sezione di Lecce, Via Arnesano IT - 73100 Lecce, Italy

[72b] Università del Salento, Dipartimento di Fisica, Via Arnesano IT - 73100 Lecce, Italy

[73] University of Liverpool, Oliver Lodge Laboratory, P.O. Box 147, Oxford Street, Liverpool L69 3BX, United Kingdom

[74] Jožef Stefan Institute and University of Ljubljana, Department of Physics, SI-1000 Ljubljana, Slovenia

[75] Queen Mary University of London, Department of Physics, Mile End Road, London E1 4NS, United Kingdom

[76] Royal Holloway, University of London, Department of Physics, Egham Hill, Egham, Surrey TW20 0EX, United Kingdom

[77] University College London, Department of Physics and Astronomy, Gower Street, London WC1E 6BT, United Kingdom

[78] Laboratoire de Physique Nucléaire et de Hautes Energies, Université Pierre et Marie Curie (Paris 6), Université Denis Diderot (Paris-7), CNRS/IN2P3, Tour 33, 4 place Jussieu, FR - 75252 Paris Cedex 05, France

[79] Fysiska institutionen, Lunds universitet, Box 118, SE - 221 00 Lund, Sweden

[80] Universidad Autonoma de Madrid, Facultad de Ciencias, Departamento de Fisica Teorica, ES - 28049 Madrid, Spain

[81] Universität Mainz, Institut für Physik, Staudinger Weg 7, DE - 55099 Mainz, Germany

[82] University of Manchester, School of Physics and Astronomy, Manchester M13 9PL, United Kingdom

[83] CPPM, Aix-Marseille Université, CNRS/IN2P3, Marseille, France

[84] University of Massachusetts, Department of Physics, 710 North Pleasant Street, Amherst, MA 01003, USA

[85] McGill University, High Energy Physics Group, 3600 University Street, Montreal, Quebec H3A 2T8, Canada

[86] University of Melbourne, School of Physics, AU - Parkville, Victoria 3010, Australia

[87] The University of Michigan, Department of Physics, 2477 Randall Laboratory, 500 East University, Ann Arbor, MI 48109-1120, USA

[88] Michigan State University, Department of Physics and Astronomy, High Energy Physics Group, East Lansing, MI 48824-2320, USA

[89a] INFN Sezione di Milano, via Celoria 16, IT - 20133 Milano, Italy

[89b] Università di Milano, Dipartimento di Fisica, via Celoria 16, IT - 20133 Milano, Italy

[90] B.I. Stepanov Institute of Physics, National Academy of Sciences of Belarus, Independence Avenue 68, Minsk 220072, Republic of Belarus

[91] National Scientific & Educational Centre for Particle & High Energy Physics, NC PHEP BSU, M. Bogdanovich St. 153, Minsk 220040, Republic of Belarus

[92] Massachusetts Institute of Technology, Department of Physics, Room 24-516, Cambridge, MA 02139, USA

[93] University of Montreal, Group of Particle Physics, C.P. 6128, Succursale Centre-Ville, Montreal, Quebec, H3C 3J7, Canada

[94] P.N. Lebedev Institute of Physics, Academy of Sciences, Leninsky pr. 53, RU - 117 924 Moscow, Russia

[95] Institute for Theoretical and Experimental Physics (ITEP), B. Cheremushkinskaya ul. 25, RU 117 218 Moscow, Russia

[96] Moscow Engineering & Physics Institute (MEPhI), Kashirskoe Shosse 31, RU - 115409 Moscow, Russia

[97] Lomonosov Moscow State University Skobeltsyn Institute of Nuclear Physics (MSU SINP), 1(2), Leninskie gory, GSP-1, Moscow 119991 Russian Federation, Russia

[98] Ludwig-Maximilians-Universität München, Fakultät für Physik, Am Coulombwall 1, DE - 85748 Garching, Germany

[99] Max-Planck-Institut für Physik, (Werner-Heisenberg-Institut), Föhringer Ring 6, 80805 München, Germany

[100] Nagasaki Institute of Applied Science, 536 Aba-machi, JP Nagasaki 851-0193, Japan

[101] Nagoya University, Graduate School of Science, Furo-Cho, Chikusa-ku, Nagoya, 464-8602, Japan

[102a] INFN Sezione di Napoli, Complesso Universitario di Monte Sant'Angelo, via Cinthia, IT - 80126 Napoli, Italy

[102b] Università di Napoli, Dipartimento di Scienze Fisiche, Complesso Universitario di Monte Sant'Angelo, via Cinthia, IT - 80126 Napoli, Italy

[103] University of New Mexico, Department of Physics and Astronomy, MSC07 4220, Albuquerque, NM 87131, USA

[104] Radboud University Nijmegen/NIKHEF, Department of Experimental High Energy Physics, Heyendaalseweg 135, NL-6525 AJ, Nijmegen, Netherlands

[105] Nikhef National Institute for Subatomic Physics, and University of Amsterdam, Science Park 105, 1098 XG Amsterdam, Netherlands

[106] Department of Physics, Northern Illinois University, LaTourette Hall Normal Road, DeKalb, IL 60115, USA

[107] Budker Institute of Nuclear Physics (BINP), RU - Novosibirsk 630 090, Russia

[108] New York University, Department of Physics, 4 Washington Place, New York NY 10003, USA

[109] Ohio State University, 191 West Woodruff Ave, Columbus, OH 43210-1117, USA

[110] Okayama University, Faculty of Science, Tsushimanaka 3-1-1, Okayama 700-8530, Japan

[111] University of Oklahoma, Homer L. Dodge Department of Physics and Astronomy, 440 West Brooks, Room 100, Norman, OK 73019-0225, USA

[112] Oklahoma State University, Department of Physics, 145 Physical Sciences Building, Stillwater, OK 74078-3072, USA

[113] Palacký University, 17.listopadu 50a, 772 07 Olomouc, Czech Republic

[114] University of Oregon, Center for High Energy Physics, Eugene, OR 97403-1274, USA

[115] LAL, Univ. Paris-Sud, IN2P3/CNRS, Orsay, France

[116] Osaka University, Graduate School of Science, Machikaneyama-machi 1-1, Toyonaka, Osaka 560-0043, Japan

[117] University of Oslo, Department of Physics, P.O. Box 1048, Blindern, NO - 0316 Oslo 3, Norway

[118] Oxford University, Department of Physics, Denys Wilkinson Building, Keble Road, Oxford OX1 3RH, United Kingdom

[119a] INFN Sezione di Pavia, Via Bassi 6, IT-27100 Pavia, Italy

[119b] Università di Pavia, Dipartimento di Fisica Nucleare e Teorica, Via Bassi 6, IT-27100 Pavia, Italy

[120] University of Pennsylvania, Department of Physics, High Energy Physics Group, 209 S. 33rd Street, Philadelphia, PA 19104, USA

[121] Petersburg Nuclear Physics Institute, RU - 188 300 Gatchina, Russia

[122a] INFN Sezione di Pisa, Largo B. Pontecorvo 3, IT - 56127 Pisa, Italy

[122b] Università di Pisa, Dipartimento di Fisica E. Fermi, Largo B. Pontecorvo 3, IT - 56127 Pisa, Italy

[123] University of Pittsburgh, Department of Physics and Astronomy, 3941 O'Hara Street, Pittsburgh, PA 15260, USA

[124a] Laboratorio de Instrumentacao e Fisica Experimental de Particulas - LIP, Avenida Elias Garcia 14-1, PT - 1000-149 Lisboa, Portugal, Spain

[124b] Universidad de Granada, Departamento de Fisica Teorica y del Cosmos and CAFPE, E-18071 Granada, Spain

[125] Institute of Physics, Academy of Sciences of the Czech Republic, Na Slovance 2, CZ - 18221 Praha 8, Czech Republic

[126] Charles University in Prague, Faculty of Mathematics and Physics, Institute of Particle and Nuclear Physics, V Holesovickach 2, CZ - 18000 Praha 8, Czech Republic

[127] Czech Technical University in Prague, Zikova 4, CZ - 166 35 Praha 6, Czech Republic

[128] State Research Center Institute for High Energy Physics, Moscow Region, 142281, Protvino, Pobeda street, 1, Russia

[129] Rutherford Appleton Laboratory, Science and Technology Facilities Council, Harwell Science and Innovation Campus, Didcot OX11 0QX, United Kingdom

[130] University of Regina, Physics Department, Canada

[131] Ritsumeikan University, Noji Higashi 1 chome 1-1, JP - Kusatsu, Shiga 525-8577, Japan

[132a] INFN Sezione di Roma I, Piazzale A. Moro 2, IT- 00185 Roma, Italy

[132b] Università La Sapienza, Dipartimento di Fisica, Piazzale A. Moro 2, IT- 00185 Roma, Italy

[133a] INFN Sezione di Roma Tor Vergata, via della Ricerca Scientifica, IT-00133 Roma, Italy

[133b] Università di Roma Tor Vergata, Dipartimento di Fisica, via della Ricerca Scientifica, IT-00133 Roma, Italy

[134a] INFN Sezione di Roma Tre, via della Vasca Navale 84, IT-00146 Roma, Italy

[134b] Università Roma Tre, Dipartimento di Fisica, via della Vasca Navale 84, IT-00146 Roma, Italy

[135a] Réseau Universitaire de Physique des Hautes Energies (RUPHE): Université Hassan II, Faculté des Sciences Ain Chock, B.P. 5366, MA - Casablanca, Morocco

[135b] Centre National de l'Energie des Sciences Techniques Nucleaires (CNESTEN), B.P. 1382 R.P. 10001 Rabat 10001, Morocco

[135c] Université Mohamed Premier, LPTPM, Faculté des Sciences, B.P.717. Bd. Mohamed VI, 60000, Oujda, Morocco

[135d] Université Mohammed V, Faculté des Sciences, 4 Avenue Ibn Battouta, BP 1014 RP, 10000 Rabat, Morocco

[136] CEA, DSM/IRFU, Centre d'Etudes de Saclay, FR - 91191 Gif-sur-Yvette, France

[137] University of California Santa Cruz, Santa Cruz Institute for Particle Physics (SCIPP), Santa Cruz, CA 95064, USA

[138] University of Washington, Seattle, Department of Physics, Box 351560, Seattle, WA 98195-1560, USA

[139] University of Sheffield, Department of Physics & Astronomy, Hounsfield Road, Sheffield S3 7RH, United Kingdom

[140] Shinshu University, Department of Physics, Faculty of Science, 3-1-1 Asahi, Matsumoto-shi, JP - Nagano 390-8621, Japan

[141] Universität Siegen, Fachbereich Physik, D 57068 Siegen, Germany

[142] Simon Fraser University, Department of Physics, 8888 University Drive, CA - Burnaby, BC V5A 1S6, Canada

[143] SLAC National Accelerator Laboratory, Stanford, California 94309, USA

[144a] Comenius University, Faculty of Mathematics, Physics & Informatics, Mlynska dolina F2, SK - 84248 Bratislava, Slovak Republic

[144b] Institute of Experimental Physics of the Slovak Academy of Sciences, Dept. of Subnuclear Physics, Watsonova 47, SK - 04353 Kosice, Slovak Republic

[145a] University of Johannesburg, Department of Physics, PO Box 524, Auckland Park, Johannesburg 2006, South Africa

[145b] School of Physics, University of the Witwatersrand, Private Bag 3, Wits 2050, Johannesburg, South Africa, South Africa

[146a] Stockholm University: Department of Physics, AlbaNova, SE - 106 91 Stockholm, Sweden

[146b] The Oskar Klein Centre, AlbaNova, SE - 106 91 Stockholm, Sweden

[147] Royal Institute of Technology (KTH), Physics Department, SE - 106 91 Stockholm, Sweden

[148] Stony Brook University, Department of Physics and Astronomy, Nicolls Road, Stony Brook, NY 11794-3800, USA

[149] University of Sussex, Department of Physics and Astronomy Pevensey 2 Building, Falmer, Brighton BN1 9QH, United Kingdom

[150] University of Sydney, School of Physics, AU - Sydney NSW 2006, Australia

[151] Insitute of Physics, Academia Sinica, TW - Taipei 11529, Taiwan

[152] Technion, Israel Inst. of Technology, Department of Physics, Technion City, IL - Haifa 32000, Israel

[153] Tel Aviv University, Raymond and Beverly Sackler School of Physics and Astronomy, Ramat Aviv, IL - Tel Aviv 69978, Israel

[154] Aristotle University of Thessaloniki, Faculty of Science, Department of Physics, Division of Nuclear & Particle Physics, University Campus, GR - 54124, Thessaloniki, Greece

[155] The University of Tokyo, International Center for Elementary Particle Physics and Department of Physics, 7-3-1 Hongo, Bunkyo-ku, JP - Tokyo 113-0033, Japan

[156] Tokyo Metropolitan University, Graduate School of Science and Technology, 1-1 Minami-Osawa, Hachioji, Tokyo 192-0397, Japan

[157] Tokyo Institute of Technology, Department of Physics, 2-12-1 O-Okayama, Meguro, Tokyo 152-8551, Japan

[158] University of Toronto, Department of Physics, 60 Saint George Street, Toronto M5S 1A7, Ontario, Canada

[159a] TRIUMF, 4004 Wesbrook Mall, Vancouver, B.C. V6T 2A3, Canada

[159b] York University, Department of Physics and Astronomy, 4700 Keele St., Toronto, Ontario, M3J 1P3, Canada

[160] University of Tsukuba, Institute of Pure and Applied Sciences, 1-1-1 Tennoudai, Tsukuba-shi, JP - Ibaraki 305-8571, Japan

[161] Tufts University, Science & Technology Center, 4 Colby Street, Medford, MA 02155, USA

[162] Universidad Antonio Narino, Centro de Investigaciones, Cra 3 Este No.47A-15, Bogota, Colombia

[163] University of California, Irvine, Department of Physics & Astronomy, CA 92697-4575, USA

[164a] INFN Gruppo Collegato di Udine, via delle Scienze 208, IT - 33100 Udine, Italy

[164b] ICTP, Strada Costiera 11, IT-34014, Trieste, Italy

[164c] Università di Udine, Dipartimento di Fisica, via delle Scienze 208, IT - 33100 Udine, Italy

[165] University of Illinois, Department of Physics, 1110 West Green Street, Urbana, Illinois 61801, USA

[166] University of Uppsala, Department of Physics and Astronomy, P.O. Box 516, SE -751 20 Uppsala, Sweden

[167] Instituto de Física Corpuscular (IFIC) Centro Mixto UVEG-CSIC, Apdo. 22085 ES-46071 Valencia, Dept. Física At. Mol. y Nuclear; Dept. Ing. Electrónica; Univ. of Valencia, and Inst. de Microelectrónica de Barcelona (IMB-CNM-CSIC) 08193 Bellaterra, Spain

[168] University of British Columbia, Department of Physics, 6224 Agricultural Road, CA - Vancouver, B.C. V6T 1Z1, Canada

[169] University of Victoria, Department of Physics and Astronomy, P.O. Box 3055, Victoria B.C., V8W 3P6, Canada

[170] Waseda University, WISE, 3-4-1 Okubo, Shinjuku-ku, Tokyo, 169-8555, Japan

[171] The Weizmann Institute of Science, Department of Particle Physics, P.O. Box 26, IL - 76100 Rehovot, Israel

[172] University of Wisconsin, Department of Physics, 1150 University Avenue, WI 53706 Madison, Wisconsin, USA

[173] Julius-Maximilians-University of Würzburg, Physikalisches Institute, Am Hubland, 97074 Würzburg, Germany

[174] Bergische Universität, Fachbereich C, Physik, Postfach 100127, Gauss-Strasse 20, D- 42097 Wuppertal, Germany

[175] Yale University, Department of Physics, PO Box 208121, New Haven CT, 06520-8121, USA

[176] Yerevan Physics Institute, Alikhanian Brothers Street 2, AM - 375036 Yerevan, Armenia

[177] Centre de Calcul CNRS/IN2P3, Domaine scientifique de la Doua, 27 bd du 11 Novembre 1918, 69622 Villeurbanne Cedex, France

[178] Also at LIP, Portugal

[179] Also at Faculdade de Ciencias, Universidade de Lisboa, Lisboa, Portugal

[180] Also at CPPM, Marseille, France.

[181] Also at TRIUMF, Vancouver, Canada

[182] Also at FPACS, AGH-UST, Cracow, Poland

[183] Also at Department of Physics, University of Coimbra, Coimbra, Portugal

[184] Also at Università di Napoli Parthenope, Napoli, Italy

[185] Also at Institute of Particle Physics (IPP), Canada

[186] Also at Louisiana Tech University, Ruston, USA

[187] Also at Universidade de Lisboa, Lisboa, Portugal

[188] At California State University, Fresno, USA

[189] Also at Faculdade de Ciencias, Universidade de Lisboa and at Centro de Fisica Nuclear da Universidade de Lisboa, Lisboa, Portugal

[190] Also at California Institute of Technology, Pasadena, USA

[191] Also at University of Montreal, Montreal, Canada

[192] Also at Baku Institute of Physics, Baku, Azerbaijan

[193] Also at Institut für Experimentalphysik, Universität Hamburg, Hamburg, Germany

[194] Also at Manhattan College, New York, USA

[195] Also at School of Physics and Engineering, Sun Yat-sen University, Guangzhou, China

[196] Also at Taiwan Tier-1, ASGC, Academia Sinica, Taipei, Taiwan

[197] Also at School of Physics, Shandong University, Jinan, China

[198] Also at Rutherford Appleton Laboratory, Didcot, UK

[199] Also at Departamento de Fisica, Universidade de Minho, Braga, Portugal

[200] Also at Department of Physics and Astronomy, University of South Carolina, Columbia, USA

[201] Also at KFKI Research Institute for Particle and Nuclear Physics, Budapest, Hungary

[202] Also at Institute of Physics, Jagiellonian University, Cracow, Poland

[203] Also at Centro de Fisica Nuclear da Universidade de Lisboa, Lisboa, Portugal

[204] Also at Department of Physics, Oxford University, Oxford, UK

[205] Also at CEA, Gif sur Yvette, France

[206] Also at LPNHE, Paris, France

[207] Also at Nanjing University, Nanjing Jiangsu, China

[208] Deceased

References

[1] Aad G *et al* (ATLAS Collaboration) 2010 Charged-particle multiplicities in *pp* interactions at $\sqrt{s} = 900$ GeV measured with the ATLAS detector at the LHC *Phys. Lett.* B **688** 21–42 (arXiv:1003.3124 [hep-ex])

[2] Khachatryan V *et al* (CMS Collaboration) 2011 Charged particle multiplicities in *pp* interactions at $\sqrt{s} = 0.9$, 2.36 and 7 TeV *J. High Energy Phys.* JHEP01(2011)079 (arXiv:1011.5531 [hep-ex])

[3] Khachatryan V *et al* (CMS Collaboration) 2010 Transverse momentum and pseudorapidity distributions of charged hadrons in *pp* collisions at $\sqrt{s} = 7$ TeV *Phys. Rev. Lett.* **105** 022002 (arXiv:1005.3299 [hep-ex])

IOP Institute of Physics **Φ** DEUTSCHE PHYSIKALISCHE GESELLSCHAFT

[4] Khachatryan V *et al* (CMS Collaboration) 2010 Transverse momentum and pseudorapidity distributions of charged hadrons in pp collisions at $\sqrt{s} = 0.9$ and 2.36 TeV *J. High Energy Phys.* JHEP02(2010)041 (arXiv:1002.0621 [hep-ex])

[5] Aamodt K *et al* (ALICE Collaboration) 2010 Charged-particle multiplicity measured in proton–proton collisions at $\sqrt{s} = 7$ TeV with ALICE at LHC *Eur. Phys. J.* C **68** 345–54 (arXiv:1004.3514 [hep-ex])

[6] Aamodt K *et al* (ALICE Collaboration) 2010 First proton–proton collisions at the LHC as observed with the ALICE detector: measurement of the charged particle pseudorapidity density at $\sqrt{s} = 900$ GeV *Eur. Phys. J.* C **65** 111–25 (arXiv:0911.5430 [hep-ex])

[7] Aaltonen T *et al* (CDF Collaboration) 2009 Measurement of particle production and inclusive differential cross sections in $p\bar{p}$ collisions at $\sqrt{s} =1.96$ TeV *Phys. Rev.* D **79** 112005 (arXiv:0904.1098 [hep-ex])

[8] Alexopoulos T *et al* (E735 Collaboration) 1994 Multiplicity dependence of transverse momentum spectra of centrally produced hadrons in $\bar{p}p$ collisions at 0.3, 0.54, 0.9 and 1.8 TeV center-of-mass energy *Phys. Lett.* B **336** 599–604

[9] Albajar C *et al* (UA1 Collaboration) 1990 A study of the general characteristics of $p\bar{p}$ collisions at $\sqrt{s} = 0.2$ TeV to 0.9 TeV *Nucl. Phys.* B **335** 261

[10] Abe F *et al* (CDF Collaboration) 1990 Pseudorapidity distributions of charged particles produced in $\bar{p}p$ interactions at $\sqrt{s} = 630$ GeV and 1800 GeV *Phys. Rev.* D **41** 2330

[11] Ansorge R E *et al* (UA5 Collaboration) 1989 Charged particle multiplicity distributions at 200 and 900 GeV c.m. energy *Z. Phys.* C **43** 357

[12] Ansorge R E *et al* (UA5 Collaboration) 1988 Charged particle correlations in $p\bar{p}$ collisions at c.m. energies of 200, 546 and 900 GeV *Z. Phys.* C **37** 191–213

[13] Abe F *et al* (CDF Collaboration) 1988 Transverse momentum distributions of charged particles produced in $\bar{p}p$ interactions at $\sqrt{s} = 630$ GeV and 1800 GeV *Phys. Rev. Lett.* **61** 1819–22

[14] Alner G J *et al* (UA5 Collaboration) 1987 UA5: a general study of proton-antiproton physics at $\sqrt{s} = 546$ GeV *Phys. Rep.* **154** 247–383

[15] Ansorge R E *et al* (UA5 Collaboration) 1986 Diffraction dissociation at the CERN pulsed $p\bar{p}$ collider at c.m. energies of 900 and 200 GeV *Z. Phys.* C **33** 175

[16] Breakstone A *et al* (ABCDHW Collaboration) 1984 Charged multiplicity distribution in pp interactions at ISR energies *Phys. Rev.* D **30** 528

[17] Arnison G *et al* (UA1 Collaboration) 1982 Transverse momentum spectra for charged particles at the CERN proton anti-proton collider *Phys. Lett.* B **118** 167

[18] Aad G *et al* (ATLAS Collaboration) 2008 The ATLAS experiment at the CERN Large Hadron Collider *JINST* **3** S08003

[19] Evans L and Bryant P (ed) 2008 LHC Machine *JINST* **3** S08001

[20] Aad G *et al* (ATLAS Collaboration) 2010 The ATLAS Inner Detector commissioning and calibration *Eur. Phys. J.* C **70** 787–21 (arXiv:1004.5293)

[21] Sjostrand T, Mrenna S and Skands P 2006 PYTHIA 6.4 physics and manual *J. High Energy Phys.* JHEP05(2006)026 (arXiv:hep-ph/0603175)

[22] ATLAS Collaboration 2010 ATLAS Monte Carlo tunes for MC09 *CERN Report* ATL-PHYS-PUB-2010-002

[23] Sherstnev A and Thorne R S 2007 Parton distributions for LO generators *Eur. Phys. J.* C **55** 553–75 (arXiv:0711.2473)

[24] Sjostrand T 2004 New showers with transverse-momentum-ordering *Proc. Workshop on Physics at TeV Colliders, Les Houches, France* submitted (arXiv:hep-ph/0401061)

[25] ATLAS Collaboration 2010 The ATLAS Simulation Infrastructure *Eur. Phys. J.* C **70** 823–74 (arXiv:1005.4568)

[26] Agostinelli S *et al* (GEANT4 Collaboration) 2002 GEANT4: a simulation toolkit *Nucl. Instrum. Methods* A **506** 250–303

[27] Albrow M G *et al* 2006 Tevatron-for-LHC report of the QCD working group (arXiv:hep-ph/0610012)

[28] Sjostrand T, Mrenna S and Skands P Z 2008 Brief Introduction to PYTHIA 8.1 *Comput. Phys. Commun.* **178** 852–67 (arXiv:0710.3820)

[29] Engel R 1995 Photoproduction within the two component dual parton model. 1. Amplitudes and cross-sections *Z. Phys.* C **66** 203–14

[30] Schuler G A and Sjostrand T 1993 Towards a complete description of high-energy photoproduction *Nucl. Phys.* B **407** 539

[31] Schuler G A and Sjostrand T 1994 Hadronic diffractive cross sections and the rise of the total cross section *Phys. Rev.* D **49** 2257–67

[32] Aktas A *et al* 2007 *J. High Energy Phys.* JHEP10(2007)042 (arXiv:0708.3217)

[33] Navin S 2010 Diffraction in Pythia (arXiv:1005.3894)

[34] ATLAS Collaboration 2010 Charged particle multiplicities in pp interactions at $\sqrt{s} = 0.9$ and 7 TeV in a diffractive limited phase space measured with the ATLAS detector at the LHC and a new PYTHIA 6 tune *CERN Report* ATLAS-CONF-2010-031

[35] Buttar C *et al* 2006 Les Houches physics at TeV colliders 2005, standard model and Higgs working group: summary report arXiv:hep-ph/0604120

[36] Buckley A *et al* 2010 Rivet user manual arXiv:1003.0694 [hep-ph]

[37] Buckley A, Hoeth H, Lacker H, Schulz H and von Seggern J E 2010 Systematic event generator tuning for the LHC *Eur. Phys. J.* C **65** 331–57 (arXiv:0907.2973 [hep-ph])

[38] Hamacher K and Weierstall M 1995 The next round of hadronic generator tuning heavily based on identified particle data arXiv:hep-ex/9511011

[39] ATLAS Collaboration 2010 Track-based underlying event measurements in pp collisions at $\sqrt{s} = 900$ GeV and 7 TeV with the ATLAS Detector at the LHC *CERN Report* ATLAS-CONF-2010-029

[40] Aad G *et al* (ATLAS Collaboration) 2010 Measurement of underlying event characteristics using charged particles in pp collisions at $\sqrt{s} = 900$ GeV and 7 TeV with the ATLAS detector *Phys. Rev.* D at press (arXiv:1012.0791)

[41] Acosta D E *et al* (CDF Collaboration) 2002 Soft and hard interactions in $p\bar{p}$ collisions at $\sqrt{s} = 1800$-GeV and 630-GeV *Phys. Rev.* D **65** 072005

[42] Piacquadio G, Prokofiev K and Wildauer A 2008 Primary vertex reconstruction in the ATLAS experiment at LHC *J. Phys.: Conf. Ser.* **119** 032033

[43] ATLAS Collaboration 2010 Characterization of interaction-point beam parameters using the pp event-vertex distribution reconstructed in the ATLAS Detector at the LHC *CERN Report* ATLAS-CONF-2010-027

[44] Cornelissen T *et al* 2007 Concepts, design and implementation of the ATLAS New Tracking (NEWT) *CERN Report* ATL-SOFT-PUB-2007-007

[45] Cornelissen T *et al* 2008 The new ATLAS track reconstruction (NEWT) *J. Phys.: Conf. Ser.* **119** 032014

[46] D'Agostini G 1995 A multidimensional unfolding method based on Bayes' theorem *Nucl. Instrum. Methods* A **362** 487–98

[47] Tsallis C 1988 Possible generalization of Boltzmann–Gibbs statistics *J. Stat. Phys.* **52** 479–87

[48] Adare A *et al* (PHENIX Collaboration) 2011 Measurement of neutral mesons in $p + p$ collisions at $\sqrt{s} = 200$ GeV and scaling properties of hadron production *Phys. Rev.* D **83** 052004 (arXiv:1005.3674 [hep-ex])

[49] Acosta D E *et al* (CDF Collaboration) 2003 Underlying event in inclusive jet production http://www-cdf.fnal.gov/physics/new/qcd/run2/ue/chgjet/index.html

[50] Acosta D E *et al* (CDF Collaboration) 2004 The underlying event in hard interactions at the Tevatron $\bar{p}p$ collider *Phys. Rev.* D **70** 072002

[51] Abazov V M *et al* (D0 Collaboration) 2005 Measurement of dijet azimuthal decorrelations at central rapidities in $p\bar{p}$ collisions at $\sqrt{s} = 1.96$ TeV *Phys. Rev. Lett.* **94** 221801

[52] Aaltonen T *et al* (CDF Collaboration) 2009 Measurement of particle production and inclusive differential cross sections in $p\bar{p}$ collisions at $\sqrt{s} = 1.96$ TeV *Phys. Rev.* D **79** 112005

[53] Affolder A A *et al* (CDF Collaboration) 2000 The transverse momentum and total cross section of e^+e^- pairs in the Z boson region from $p\bar{p}$ collisions at $\sqrt{s} = 1.8$ TeV *Phys. Rev. Lett.* **84** 845–50